A HIGH FIELD SOLID-STATE NUCLEAR MAGNETIC RESONANCE EXPERIMENTAL STUDY FOR CLAY AND SHALE SWELLING

by

Mohammed Alzahran

A thesis submitted to the Faculty and Board of Trustees of the Colorado School of Mines in Partial fulfillment of the requirements for the degree of Master of Science (Petroleum Engineering).

Golden, Colorado

Date _____

Signed: _____
Mohammed S. Alzahrani

Signed: _____
Dr. Azra N. Tutuncu
Thesis Advisor

Golden, Colorado

Date _____

Signed: _____
Dr. William Fleckenstein
Professor and Head
Department of Petroleum Engineering

ABSTRACT

The development of the shale resources faces many problems related to their complex structure and challenging conditions. Drilling and fracturing operations suffer from the swelling tendency of clays and shale formations. The expansion mechanisms of clays have been discussed in detail in the literature and several theories have been developed to predict the swelling in shales. The crystalline (interlayer), double-layer, and the layers breakage/formation swelling mechanisms are the mechanisms that are the most contributing for the clay swelling. They all depend on the ionic concentration of the system. Low frequency NMR technique has been used in the industry mainly to determine the rock properties. NMR has also been used to determine the chemistry of the matters, especially in high frequency fields in chemistry and other scientific applications. Yet, to the author's knowledge, there has been no high field NMR study exists to describe the swelling behavior of the clays. In this study, we conducted an experimental investigation to determine the feasibility of high frequency NMR measurements in characterizing the expansive behavior of pure clays and shale formations. Mainly, the benefits of utilizing the high field NMR for studying the swelling behavior of clays have been investigated and NMR data was collected and analyzed (e.g. relaxation times and distributions) for various liquid/clay systems. NMR data was also correlated to petrophysical and acoustic properties of pure clays and shales reported in the literature. An ultimate goal of this work is to evaluate the feasibility of the high field NMR use for characterization of the unconventional resource shale systems, in particular the Eagle Ford shale.

In this study, high field NMR has been used to determine several clay and Eagle Ford shale structure and to measure the relaxation times of dry and saturated samples. Moreover, the

relaxation time distribution curves have been used to identify the dominant swelling mechanism(s) taking place in the pure clays studied. Our study concentrates on the pure montmorillonite as it has the highest affinity to liquids. Few kaolinite and Eagle Ford shale samples have also been investigated to compare to the montmorillonite results and to present NMR data utilization in unconventional resource characterization.

TABLE OF CONTENTS

LIST OF FIGURES

LIST OF TABLES

ACKNOWLEDGMENTS

I would like to thank my advisor Dr. Azra N. Tutuncu for her continuous support, guidance, and encouragement throughout my graduate studies. She provided me with all the knowledge and advice to make this study completed. Also, I would like to thank Dr. Yuan Yang for her valuable support in this research. She was very generous in sharing her knowledge, experience, and precious time in NMR laboratory. I would also like to thank Dr. Mansur Ermila for his valuable recommendations and help.

DEDICATION

For their prayers, love, and words of encouragement, with a special feeling of gratitude I thank my parents and dedicate this work to them.

CHAPTER 1

NUCLEAR MAGNETIC RESONANCE (NMR) PETROPHYSICS

Before discussing the NMR measurements and its applications, it is imperative to first understand the nuclear magnetic resonance petrophysics. In this chapter, an introduction to the nuclear magnetic resonance (NMR) fundamentals and key parameters controlling the NMR response will be discussed. The relaxation times and the mechanisms affecting them will be explained.

1.1 Relaxation Theory

Familiarity to the NMR relaxation theory and the definitions of the T_1 and T_2 relaxation times that are considered as the NMR characteristics of materials and formations is essential prior to any NMR measurement and modeling effort. In this section, the NMR relaxation and how the longitudinal and transverse relaxation processes take place will be discussed. Furthermore, the data inversion from acquisition time domain to relaxation time domain will be explained as majority of the information used in the petroleum engineering applications are obtained from the relaxation time domain distributions.

1.1.1 Longitudinal and Transverse Relaxation

In a magnetic field (B_0), the spinning nuclei are aligned in the direction of the field. The actual magnetic field felt by different protons depends on the electron density around the nucleus, which reduces this field (Reich, 2012). In this field, the nuclei precess around the field, as illustrated in Figure 1.1, with a frequency equal to the Larmour frequency. This frequency

represents the resonance frequency of proton and depends on the magnetic field strength (Coates et al., 1999). Equations 1.1 (Reich, 2012) and 1.2 describe the actual magnetic field on the proton and the Larmour frequency, respectively.

$$B = Bo - Be \tag{1.1}$$

$$f = \frac{\gamma B_0}{2\pi} \tag{1.2}$$

where γ is the gyromagnetic ratio, a measure of the nuclear magnetism and Be is the alteration by the electrons density. At equilibrium, most of the precessing nuclei are parallel to the field direction and the net magnetization vector is in the same direction. This vector equals to the equilibrium magnetization (M_0).

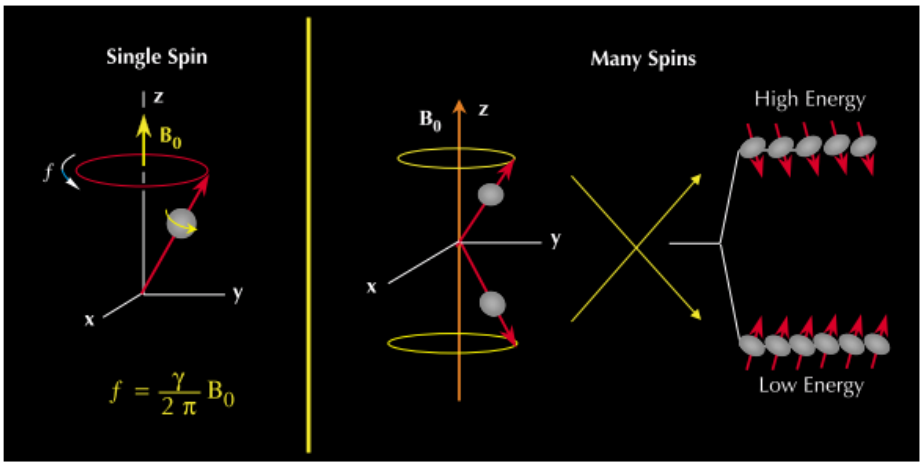

Figure 1.1: The precessional movement of the spinning nuclei in a magnetic field (Coates et al., 1999)

A given radio frequency (rf) pulse, applied perpendicular to the original field will tip the net magnetization (M_0) from its original (at equilibrium) direction (z axis) into the transverse plane (xy plane) taking its component along z-axis to zero (Mz = 0). When the oscillating field is

shut off, the proton spins start to diphase as they lose their coherence due to their interactions (Coates et al., 1999).

The magnetization on the transverse plane (Mxy) then starts to decay with time until it completely vanishes. At the same time, the magnetization (Mz) is observed growing back along the longitudinal axis to reach the original state of equilibrium (M_0). Both of these decay and growth processes are called the relaxation processes and they take place simultaneously (Traficante, 1996).

1.1.2 T_1 and T_2 Relaxation Times

In theory, T_1 provides information on the magnetization growth rate along the z-axis (return to equilibrium position). If the magnetization grows at a rate equal to the initial rate, it will reach a complete relaxation in a time equal to T_1 (Traficante, 1996). This relaxation is an exponential function as expressed in equation (1.3) and illustrated in Figure 1.2. Similarly, T_2 provides information on the magnetization decay rate on the xy-plane. A decay of the amplitudes, FID (frequency induction decay), accompanies the decay of (Mxz). T_2* is a measure of how long this decay takes. If the FID decays at a rate equal to the initial rate, it will reach a complete decaying in a time equal to T_2* (Traficante, 1996). The FID also follows an exponential function as expressed in equation (1.4) and illustrated in Figure 1.3 (Traficante, 1996).

When the net magnetization is flipped into the transverse plane, it will diphase as it rotates around the (z axis) because the spins have different frequencies as they slightly undergo different magnetic field and they move at different speeds. This makes the transverse relaxation

depend on the diffusion which is not a part of the longitudinal relaxation, as it will be discussed later.

The longitudinal relaxation time, T_1, can also be described as a distinguishing time at which the growing Mz reaches the value of $\boldsymbol{Mz = Mo\ (1 - e^{-1})}$. The value of T_1 reflects how easy the magnetic energy is transferred between the spins in the material and the environment and usually is referred to as the spin-lattice relaxation time. Small values of T_1 imply rapid energy transfer expediting to reach the equilibrium while large values imply slow energy transfer delaying the reach to the equilibrium state. The transverse relaxation time, T_2, is usually called spin-spin relaxation time which describes the energy transfer between spins (Dunn et al., 2002).

$$\mathrm{Mz} = \mathrm{Mo}\ (1 - \mathrm{e}^{-\mathrm{t}/\mathrm{T1}}), \tag{1.3}$$

$$\mathrm{A} = \mathrm{Ao}\ \mathrm{e}^{-\mathrm{t}/\mathrm{T2}}, \tag{1.4}$$

where A is the resulted amplitude (or magnetization).

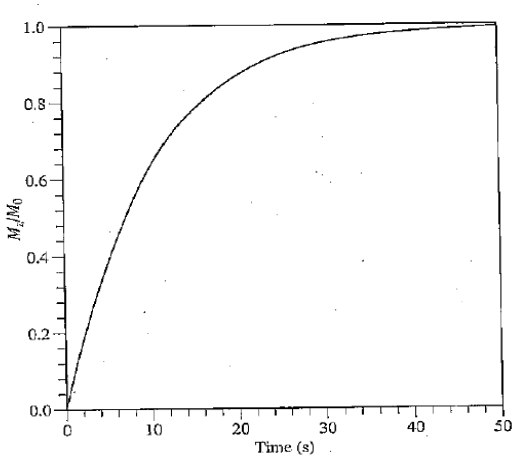

Figure 1.2: Longitudinal relaxation - growth of Mz with time (Traficante, 1996).

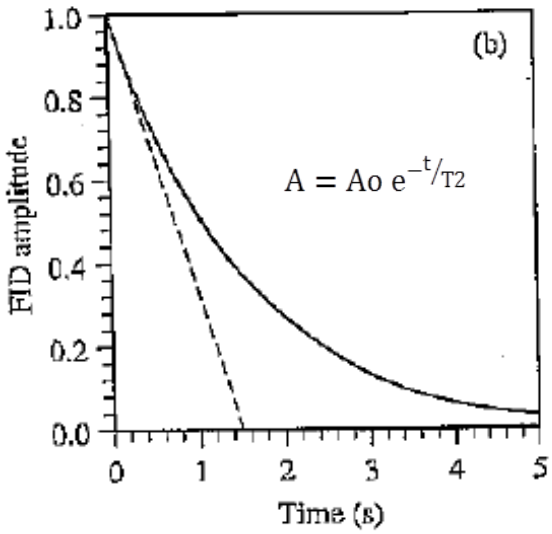

Figure 1.3: Frequency Induction Decay (FID) amplitude with time (Traficante, 1996).

1.1.3 NMR Raw Data - Spin-Echo Train and T_2 Distribution

The protons in the formations are oriented randomly. When the formation is logged for NMR response, the permanent magnet produces a magnetic field that aligns the protons in certain direction. The oscillating field is applied to tip these protons away from their positions and when it is shut off, they tip back to their positions and relax. Specific pulse patterns are applied to generate spin-echos that are detected by the NMR tool and reflected as spin-echo trains. These trains are generated by plotting the amplitudes of the spin-echoes as a function of time, as shown in Figure 1.4. The spin echo-train can be fitted by various exponential decaying constants. The sets of all of these constants form the transverse relaxation time (T_2). The T_2 distribution generated from the spin-echo train in Figure 1.4 is shown in Figure 1.5 (Coates et al., 1999).

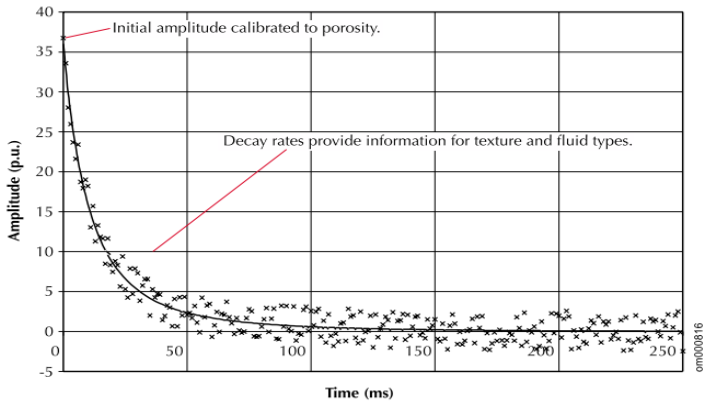

Figure 1.4: Example of the NMR Spin-Echo Train (Coates et al., 1999).

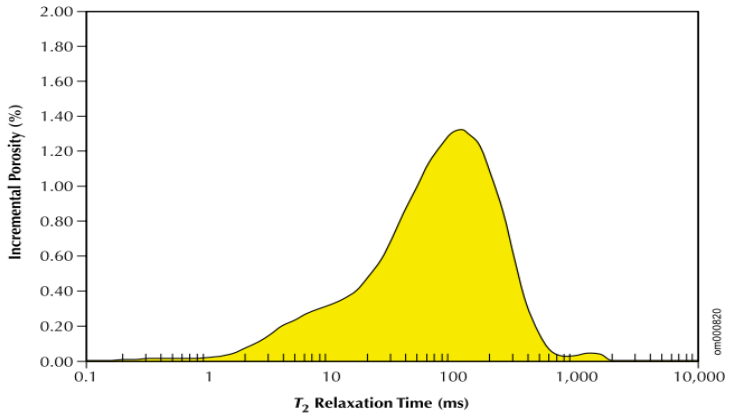

Figure 1.5: T_2 distribution of the spin-echo train in Figure 1.4 (Coates et al., 1999).

1.1.4 T_2 Processing

Due to its faster detection since $T_2 <= T_1$, T_2 relaxation time is more practical in the logging processes than T_1 relaxation time. In addition, T_2 distribution curve is easier invert for the analysis and it is used directly to estimate the porosity and the pore size distribution in the logged interval.

The spin-echo train is converted into T_2 distributions utilizing a mathematical technique, called the mapping process. This process contains a set of equations that involves processing of individual echoes as shown in Figure 1.6. To simplify the process, a multi-exponential model is used assuming that the T_2 distribution is represented by a number of discrete relaxation times that are related to porosity. These times are pre-selected and the porosities are estimated to fit their values. Figure 1.7 illustrates how this process inverts the measured echo train into the porosity as function of time (Coates et al., 1999).

$$
\begin{aligned}
echo(1) &= \phi_1 e^{-\left[t(1)/T_{2,1}\right]} + \phi_2 e^{-\left[t(1)/T_{2,2}\right]} + \phi_3 e^{-\left[t(1)/T_{2,3}\right]} + \cdots + \phi_m e^{-\left[t(1)/T_{2,m}\right]} + noise \\
echo(2) &= \phi_1 e^{-\left[t(2)/T_{2,1}\right]} + \phi_2 e^{-\left[t(2)/T_{2,2}\right]} + \phi_3 e^{-\left[t(2)/T_{2,3}\right]} + \cdots + \phi_m e^{-\left[t(2)/T_{2,m}\right]} + noise \\
&\vdots \\
echo(n) &= \phi_1 e^{-\left[t(n)/T_{2,1}\right]} + \phi_2 e^{-\left[t(n)/T_{2,2}\right]} + \phi_3 e^{-\left[t(n)/T_{2,3}\right]} + \cdots + \phi_m e^{-\left[t(n)/T_{2,m}\right]} + noise
\end{aligned}
$$

Figure 1.6: Mathematical illustration of the T_2 mapping (Coates et al., 1999).

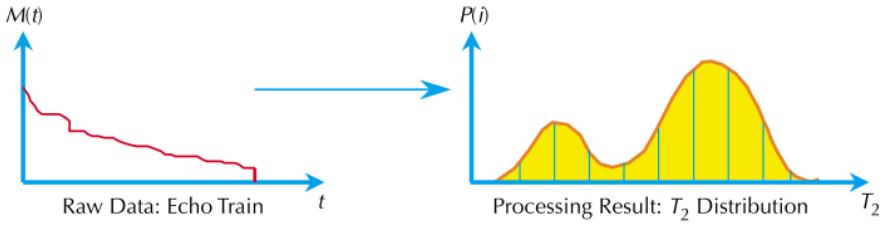

Figure 1.7: Echo fitting process (Coates et al., 1999).

The multi-exponential model to solve the NMR relaxation decay is usually an ill-posed problem giving a non-unique solution and resulting in a building up error. Various regulatory methods have been used in inverting the data to provide a solution for the non-uniqueness issue. In this research study, a Matlab code based on regularized inverse Laplace transform CONTIN (Provencher, 1982) has been utilized.

1.2 NMR Relaxation Mechanisms in Porous Media

There are three relaxations mechanisms for the fluids in porous media: bulk fluid process, diffusion process and surface relaxation. The last affects only T_2 whilst the other two mechanisms influence both T_1 and T_2.

1.2.1 The Bulk Relaxation

Bulk T_1 and T_2 are the measured relaxation times when fluids are not contained in the pore space (i.e., fluid is not contacting a surface). Surface T_1 and T_2 are the relaxation times resulting from the surface relaxation. T_2 due to diffusion is the relaxation time induced by the diffusion of magnetic field gradient.

The bulk relaxation takes place as a result of the molecular interactions within the fluid. In theory, the bulk relaxation is due to the differences in the magnetic field that the spins in the liquid have. Generally, this relaxation is a function of temperature and properties of fluids and not a function of any formation property.

1.2.2 The Surface Relaxation

The surface relaxation takes place as a result of the interactions between the neculi in the fluid and the pore surfaces. Basically, it is resulted when the protons in the fluids collide with the solid surfaces during their diffusive motion. Both transverse and longitudinal relaxations are contributed by this relaxation. The surface relaxation times are functions of T_1 and T_2 surface relaxivities, which are the T_1 and T_2 relaxing strengths for grain surfaces, and the ratio of pore surface to fluid volume. This relaxation mechanism depends on the pores in which the fluid is contained. In small pores, more restriction is put on the particles diffusion. Moreover, longer

relaxation time is needed to relax large fluid volumes if only small surface area is available. Equations (1.5) and (1.6) represent this relaxation.

$$\frac{1}{T_1 S} = \frac{\rho_1 S}{V} \tag{1.5}$$

$$\frac{1}{T_2 S} = \frac{\rho_2 S}{V} \tag{1.6}$$

where S and V are the pore surface area and the pore volume, respectively.

1.2.3 The Relaxation Due to Diffusion

The diffusion relaxation takes place as a result of the diffusion of spins in a remarkable magnetic gradient. It is related to the dephasing accompanied by the transverse relaxation. Hence, it contributes only toward the transverse relaxation and not to the longitudinal relaxation (Dunn et al., 2002). The molecules diffuse at different magnetic fields due to the different frequencies they have causing an additional decay. The diffusion relaxation time is a function of the molecular diffusion coefficient, gyromagnetic ratio of the protons, and field strength gradients. The relaxation decay due to the diffusion is given in equation (1.7) (Dunn et al., 2002).

$$\frac{1}{T_2 D} = \frac{D}{12}(\gamma G T_E)^2 \tag{1.7}$$

where D is the diffusion coefficient of the molecules, γ is the gyromagnetic ratio, T_E is the time between detected spin echoes in the Carr, Purcell, Meiboom, and Gill (CPMG) pulse sequence (will be discussed later) to measure T_2, and G is the magnetic gradient strength.

1.2.4 Total Relaxation

The bulk, surface, and diffusion relaxation mechanisms appear in parallel and the relaxation times T_1 and T_2 are described in equations 1.8 and 1.9.

$$\frac{1}{T_1} = \frac{1}{T_{1B}} + \frac{1}{T_{1S}} = \frac{1}{T_{1B}} + \frac{\rho_1 S}{V} \tag{1.8}$$

$$\frac{1}{T_2} = \frac{1}{T_{2B}} + \frac{1}{T_{2S}} + \frac{1}{T_{2D}} = \frac{1}{T_{2B}} + \frac{\rho_2 S}{V} + \frac{D}{12}(\gamma G T_E)^2 \tag{1.9}$$

In most of the petroleum engineering applications, the diffusion relaxation is neglected as low frequency magnetic field (usually 2 MHz) is used with minimal magnetic gradients. Moreover, as the bulk relaxation time that is measured in seconds is typically much greater than the surface relaxation time in milliseconds. Therefore, the surface relaxation is used as the dominant mechanism in the industry and the following simplified equations are used to determine T_1 and T_2;

$$\frac{1}{T_1} = \frac{\rho_1 S}{V} \tag{1.10}$$

$$\frac{1}{T_2} = \frac{\rho_2 S}{V} \tag{1.11}$$

CHAPTER 2

LITERATURE REVIEW FOR PETROLEUM ENGINEERING APPLICATIONS OF NUCLEAR MAGNETIC RESONANCE

The NMR techniques have been used in the oil industry since 1960s. However, the applications have been limited mainly to determine the properties of rocks and fluid types. Some research has also been conducted to determine the clay bound water cutoff values and studying the wettability and swelling effects. In this chapter, the use of NMR in the petroleum industry applications will be reviewed.

2.1 NMR Rock Properties Determination

NMR response is independent of the formation rock properties and reflects only what is contained in the pores. Thus, the properties calculated from the NMR response are considered to provide more accurate information of the reservoir fluids than other techniques used in the industry. A summary of the NMR properties is discussed in the following section.

2.1.1 NMR Porosity

The initial amplitude (or initial magnetization value) in the spin-echo train is used to calculate the porosity of the formation from the NMR log or sample measured in the laboratory as it is proportional to the hydrogen amount in the fluid. A known amplitude (or magnetization) of a known volume of the fluid is needed to determine the porosity. The measured amplitude (or magnetization) is related to the NMR response measured for samples with known porosities, e. g.

neutron porosity, or detected in a water tank (100 % porosity) as discussed by Coates et al. (1999).

When the T_2 is inverted, the initial amplitude in the FID (porosity) is represented by the area under the distribution curve. In general, the clay-bound water is detected at times less than 1.0 ms. Typically, the effective porosity is defined as the area under the curve from this cut-off time and the clay-bound water is for the remaining area below it. The NMR porosity has good accuracy and is currently considered the most accurate porosity measurement among the methods used in the industry under specific conditions (Coates et al., 1999). An example for the agreement between the laboratory NMR porosity measurements and conventional core analysis is shown in Figure 2.1.

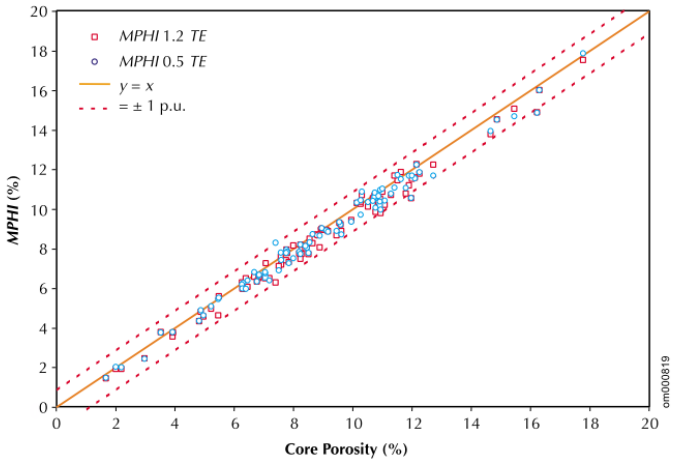

Figure 2.1: An example for the NMR porosity versus the conventional core porosity (Coates et al., 1999).

For unconventional formations applications, the NMR porosity technique revealed reliable results when compared to the helium expansion experiments under the same testing conditions. Glorioso et al. (2012) reported experimental porosity of 3.4 % using helium porosity measurement and 3.9 % utilizing NMR measurement for a shale sample with < 40 % clay

content. Publishers stated that “Widespread use will determine whether or not these porosity measurements are useful for shale gas”.

The mobile fluids can be also determined using the NMR tool. As the T_2 distribution is related to the porosity, the effective porosity can be divided into producible porosity (FFI, free-fluid index) and bound-fluid porosity (BVI, bound volume irreducible). Based on the supposition that the larger porosity will have producible fluids and the smaller porosity will have bound fluids, T_2 cutoff is determined in the laboratory to distinguish between the two porosities as shown in Figure 2.2. Common T_2 cut-off times of 33 ms and 93 ms for the Gulf of Mexico sandstones and carbonates are used, respectively (Coates et al., 1999).

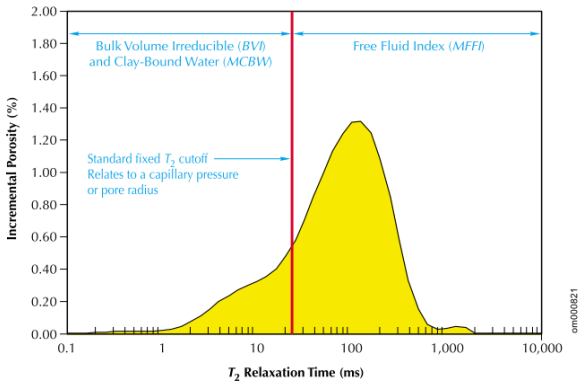

Figure 2.2: Illustration of the T_2 cut-off distinguishing between the movable and immovable fluids in pore space (Coates et al., 1999).

As a common practice in the petroleum industry, the clay bound water is responsible for the T_2 relaxation time components below 3 ms, the irreducible capillary bound water for relaxation time components between 3 and 33 ms, and the free fluid for relaxation times component above 33 ms (Dunn et al., 2002).

2.1.2 NMR Permeability

The NMR permeability is estimated from the measured NMR porosity. The most commonly used NMR permeability models in the industry are the free fluid (Coates) model for water and hydrocarbon saturated systems and the mean T_2 model for water saturated systems. When applied for calculation of the permeability in hydrocarbon saturated zones, the mean T_2 model gives erroneous results (Coates et al., 1999). Laboratory data can be used to calibrate these models as presented in Figure 2.3 for the Coates model.

Both models assume that permeability vary with the porosity to the 4th power. Coates model and average T_2 model are expressed in equations (2.1) and (2.2), respectively.

$$k = \left[\left(\frac{\emptyset}{C}\right)^2 \left(\frac{FFI}{BVI}\right)\right]^2 \qquad \text{(Coates Model)} \qquad (2.1)$$

$$k = a\, T_{2gm}{}^2 \emptyset^4 \qquad \text{(Mean } T_2 \text{ Model)} \qquad (2.2)$$

where C and a are coefficients dependent on the type of formation.

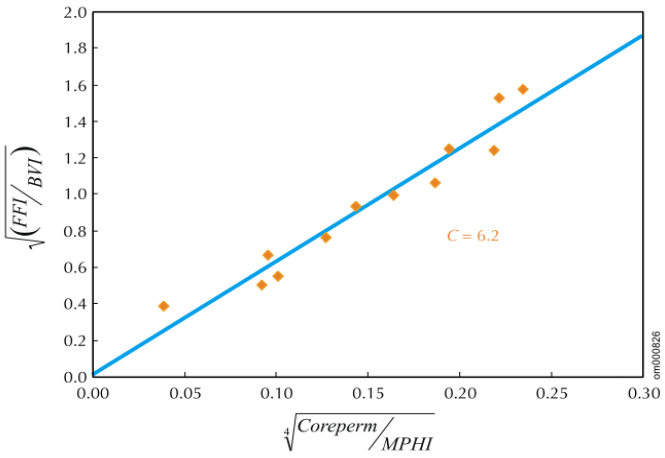

Figure 2.3: Calibrating Coates NMR permeability model (Coates et al., 1999).

2.1.3 NMR Wettability:

Besides the NMR porosity and permeability, information regarding the wettability of the rock can be inferred from the T_2 distribution curves. The rocks with mixed wettability will show a shift in the curve to the left compared to the curve of the oil bulk sample. The mixed wet rocks (oil wet-water wet) need shorter relaxation times T_2 implying that oil is in contact with the pore space. (Freedman et al., 2004)

The results of an experiment conducted by Freedman et al. (2003) for wettability determination are shown in Figure 2.4. Two of their samples show mixed-wet behavior as they shift from the bulk oil T_2 distribution, where the other two samples indicate water-wet behavior. However, the samples that show mixed wettability at low oil saturations did not present the same behavior at high oil saturations. Hence, the low oil saturations usually enhance the wettability by increasing the probability of surface interactions (Freedman et al., 2004).

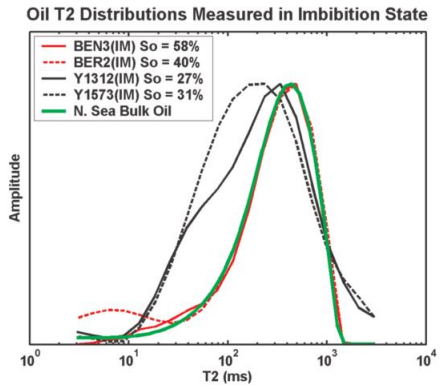

Figure 2.4: T_2 distributions for mixed-wet and water-wet samples (Freedman et al., 2004).

2.1.4 Properties and Types of Fluids

The hydrocarbons typically move in the large pore space whilst the clay bound water and the capillary bound water are located in the smaller pores. NMR qualitatively uses the

differences between fluids and pore space to determine the properties of these fluids. The qualitative values of T_1, T_2 and diffusion for various fluids in different pore space values are shown in Figure 2.5 (Coates et al., 1999).

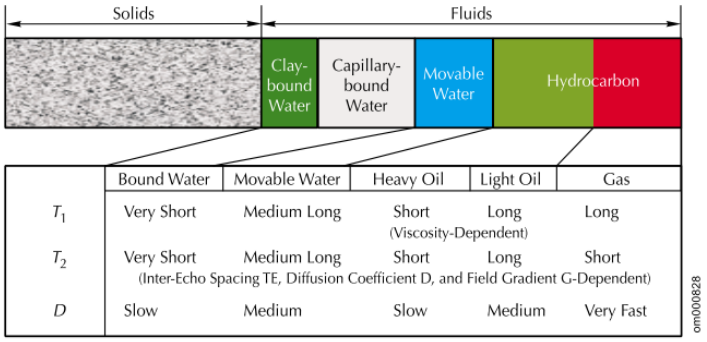

Figure 2.5: Qualitative T_1, T_2 and D values to distinguish fluids in the system (Coates et al., 1999).

2.2 Integration of NMR with Other Logs

Over the years, researchers and engineers discovered ways to combine NMR with other commonly implemented log data to better understand the formation properties. In the following sections, examples of such work are presented and discussed.

2.2.1 Water Saturation Enhancement

BVI (bound volume irreducible - irreducible fluids) and FFI (free fluid index – producible fluids) values calculated from NMR can be integrated with the water saturation data collected by the resistivity-based logs to enhance the analysis. The resistivity logs provide information to determine the water saturation in the formations, yet they can't distinguish between the amount of water in pore space that is movable or bounded. By combining these data

with the NMR calculated BVI and FFI, valuable insight toward formation evaluation is achieved (Coates et al., 1999).

2.2.2 Porosity Enhancement in Tight Gas Reservoirs

Abu-Shanab et al. (2005) combined the NMR and density porosities in one equation to correct for the lithology, gas, and heterogeneity in tight gas formations. They concluded that using the new technique gives better results than using either NMR or density porosities alone. The corrected porosity, called "the density-magnetic resonance (DMR) porosity", is expressed in equation (2.3).

$$\text{DMRP} = \emptyset = \text{A} * \emptyset_{\text{D}} + \text{B} * \emptyset_{\text{NMR}} \tag{2.3}$$

and

$$\frac{\emptyset_{\text{core}}}{\emptyset_{\text{NMR}}} = \text{A} * \frac{\emptyset_{\text{D}}}{\emptyset_{\text{NMR}}} + \text{B} \tag{2.4}$$

where A and B values can be estimated from the linear relationship in equation 2.4, using a set of core porosities values as the DMR porosities.

Figure 2.6 and Figure 2.7 show the density porosity and the DMR porosity results, respectively, for data obtained from a tight gas sandstone field (Obaiyed) in Egypt. The DMR technique revealed better matching porosity values to the core porosity in the studied reservoir.

Similarly, Xiao et al. (2012) reported a combined NMR-acoustic porosity model for gas bearing reservoir applications where the acoustic porosity is calculated from the interval transit time from sonic log. Their equations are expressed as in equations (2.5) and (2.6).

$$\emptyset = \text{A} * \emptyset_{\text{t}} + \text{B} * \emptyset_{\text{NMR}} \tag{2.5}$$

$$\frac{\emptyset_{core}}{\emptyset_{NMR}} = A * \frac{\emptyset_t}{\emptyset_{NMR}} + B \quad (2.6)$$

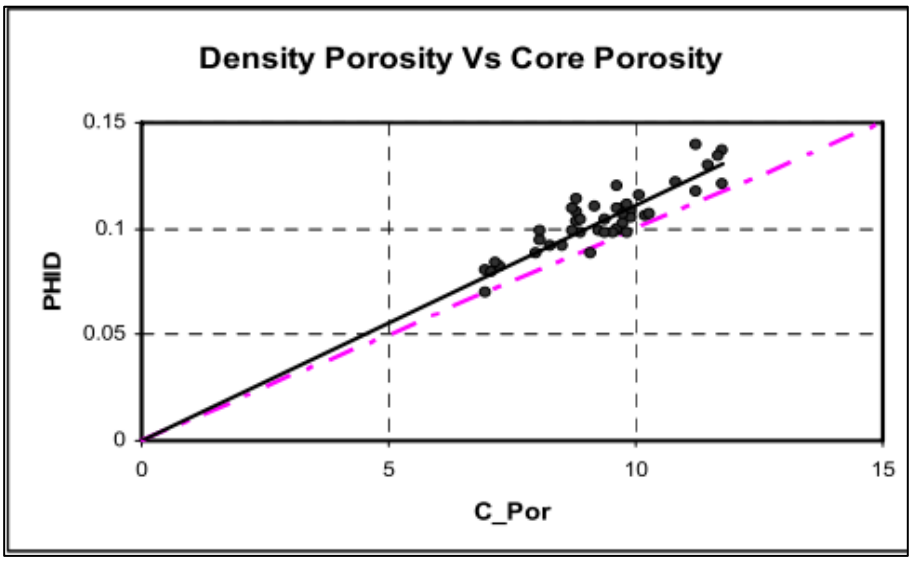

Figure 2.6: Density porosity versus the core porosity for Obaiyed field (Abu-Shanab et al., 2005).

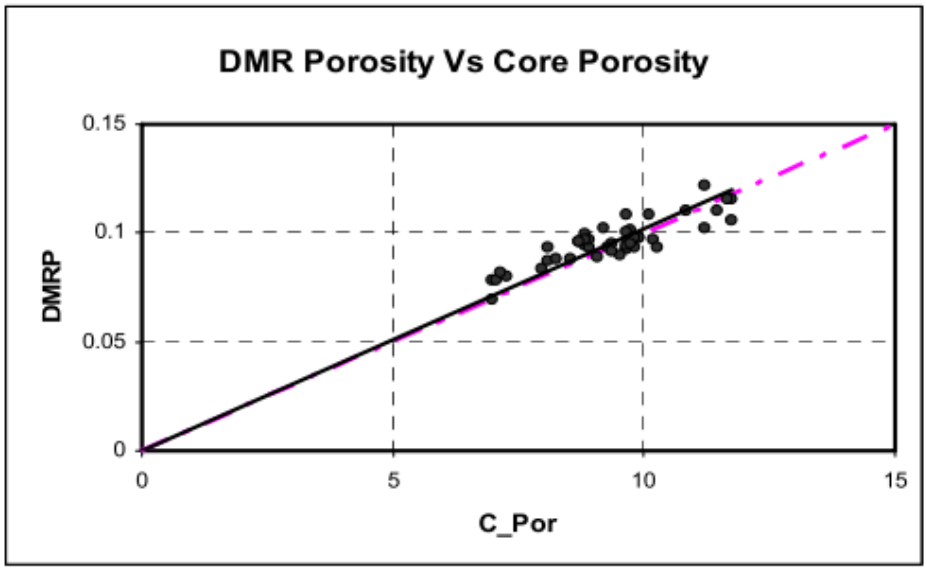

Figure 2.7: DMR porosity versus the core porosity for Obaiyed field (Abu-Shanab et al., 2005).

2.2.3 Permeability Enhancement in Tight Gas Reservoirs

Hamada (2012) presented an NMR derived permeability model for tight gas formations that used the terminology "Bulk Gas Magnetic Resonance Permeability (BGMR)" as shown in equation (2.7). This permeability is a function of the bulk gas volume (BG), which is the difference between the DMR porosity (defined in the previous section) and the NMR porosity. The technique eliminates the use of the BVI value, for example in Coates NMR permeability model, which might hold uncertainties. To derive the equation, the model considers the ideas that the capillary forces is only affected by the permeability, as the gravity is constant, and the mobility depends on the permeability, as the viscosity is constant for gas.

$$K_{BGMR} = 0.18 * 10^{(6.4 * S_{gxo})} \tag{2.7}$$

where S_{gxo} is the flushed zone gas saturation (equals to the gas volume divided by the DMR porosity). A logged interval with the core and BGMR permeabilities is illustrated in Figure 2.8. Although Hamada (2012) has not compared his method with other commonly used NMR models (e.g. Coates), the model provided a reasonable match with the core data used in his study.

2.3 Swelling Behavior of Clays with an Emphasize on Montmorillonite

In this section, background information will be presented for the swelling behavior of pure montmorillonite clay minerals, their elastic properties, and NMR relaxation response. Some information will be extended to cover the Kaolinite clay as well.

The swelling behavior in clay minerals is generally a result of addition of sheets of water in the interlayer space between the clay platelets. Several attractive and repulsive forces generally control the expansion in clays, as illustrated in Figure 2.9. In general, the repulsive forces include the crystalline hydration, electrostatic repulsion, and the osmotic swelling (when

the relative water activity for the clay is < 1) while the attractive forces include van der Waals attraction and born repulsion (Tutuncu, 1992). In the case of salt concentrated water is present in between the platelets, the water distribution is controlled by the interlayer cations and the external cations which compete for the water and if the cation hydration is the only existing force, more salt needs to be added to reduce the swelling (Slade et. al, 1991).

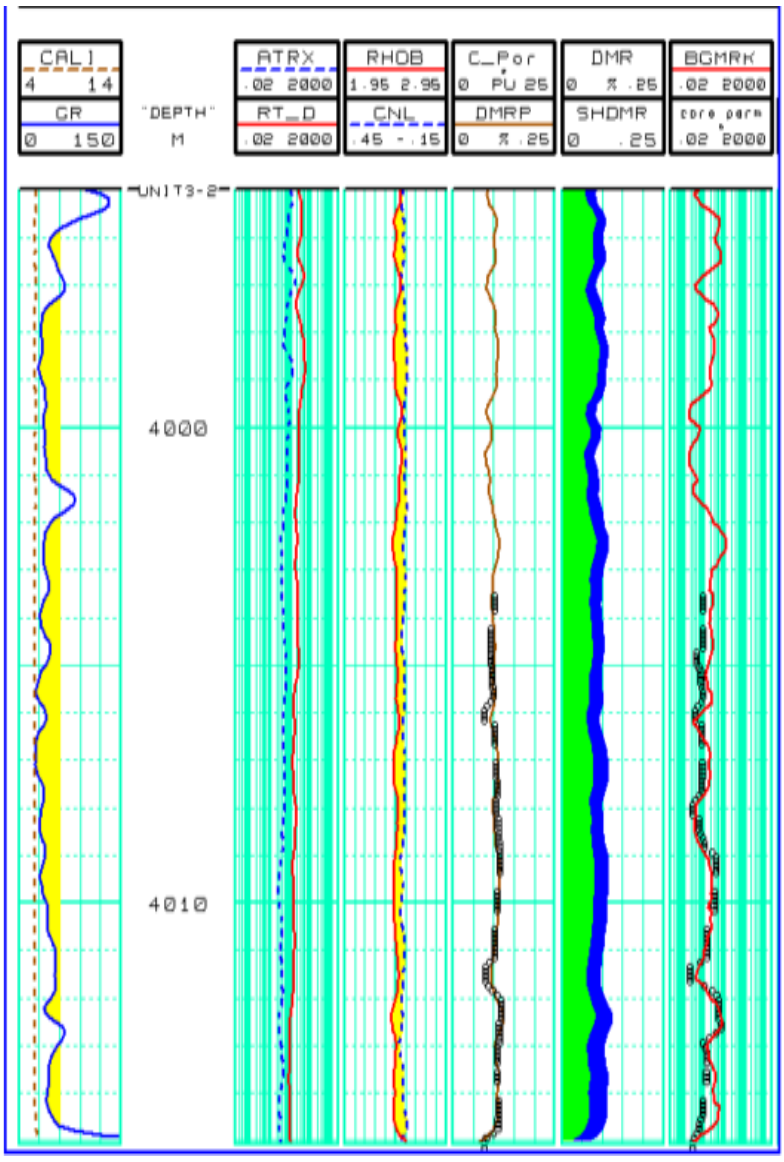

Figure 2.8: BGMR versus core permeability (right track) in a tight gas reservoir (Hamada, 2012).

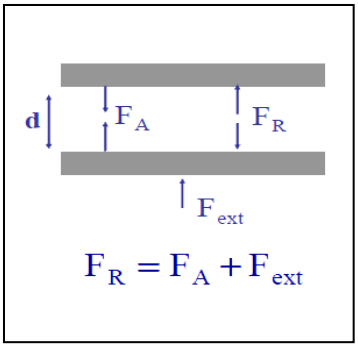

Figure 2.9: Illustration of forces acting on two clay platelets (Mese, 1995 and Tutuncu, 2012)

The interaction energy between the layers of the clay is affected by the existing repulsive and attractive forces. The effect of the repulsive electrostatic double layer force and the attractive van der Waals is described by the DLVO theory (found by and named after B. Derjaguin, L, Landau, E. Verwey, and J. Overbeek). Based on the DLVO theory, the net energy between two inner surfaces of a clay is shown if equation 2.8 (Ghosh, 2012).

$$\emptyset_{net} = (RTnk^{-1})tanh^2\left(\frac{zeV}{4kT}\right)\exp(-kd) - \frac{A_h}{12\pi d^2} \qquad (2.8)$$

where the first term represents the repulsive force and the second represents the van der Waals attractive force. In the equation, R is the gas constant (8.314), T is the temperature, n is the electrolytes concentration, e is a constant ($1.602x10^{-19}$), z is the valance of the ions in solution, V is the surface potential (mV), k is the Debye-Huckel parameter given by equation 2.9 (Ghosh, 2012), d is the distance between the surfaces, and A_h is the Hamaker constant.

$$k^{-1} = [5.404x10^{15}\ \sum z_i^2 n_i]^{-1/2} \qquad (2.9)$$

The net energy equation for the montmorillonite clay is expressed by equation 2.10. The concentration dependence of the net energy is presented in Figure 2.10. The surface potential and Hamaker constant have been assumed 600 mV, $2.2x10^{-20}$ J, respectively.

$$\emptyset_{net} = \left(13.321\ \frac{c}{\sqrt{c}} e^{-3.287\ d\ \sqrt{c}}\right) - \left(\frac{5.84}{d^2}\right) \qquad (2.10)$$

where the units of c, m, and net energy are mole/liter, nm, and mJ, respectively.

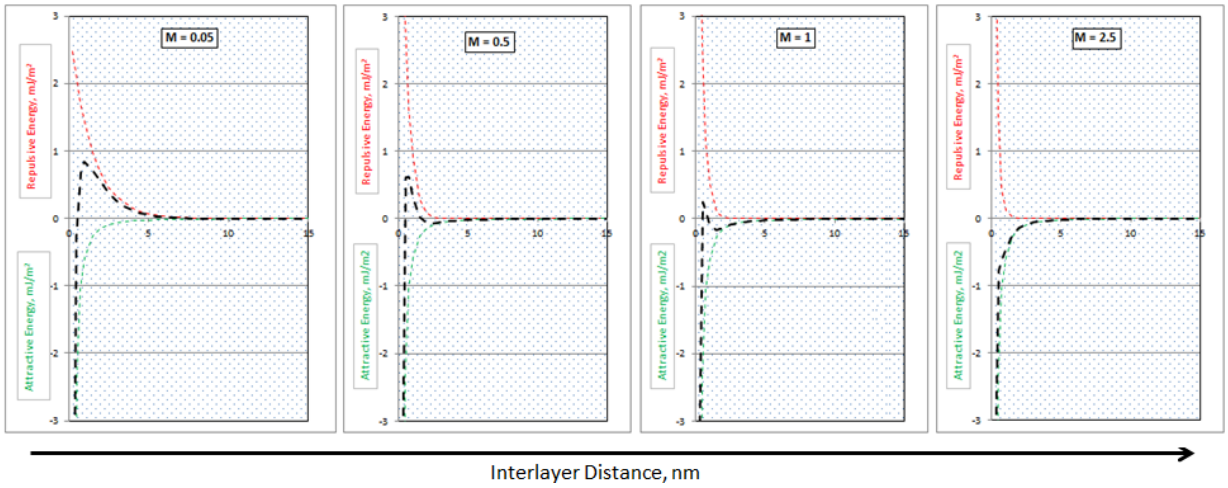

Figure 2.10: The DLVO net energy for the montmorillonite clay as a function of concentration and interlayer distance.

Mese (2008) studied the swelling tendency of various pure clays and shale formations. He conducted an experimental study using bentonite, Swy-1 smectite, kaolinite and several shale samples from various fields including Ekofisk shale measuring swelling pressures and swelling along with the acoustic velocities from these samples. The measured swelling pressures and velocities in various salt concentrations are shown in Figure 2.11 and Figure 2.12, respectively. The results assert that all clays have swelling tendency but the degree of swelling differs from clay to clay (Mese, 2008). As shown in Figure 2.11, the smectite has high tendency to swell. Its swelling pressure when exposed to 2% salt concentrations is almost the same as the swelling pressure of bentonite exposed to de-ionized water. This reaction could be a result of the larger surface area (m^2/g) of the smectite that may reach to 820 m^2/g.

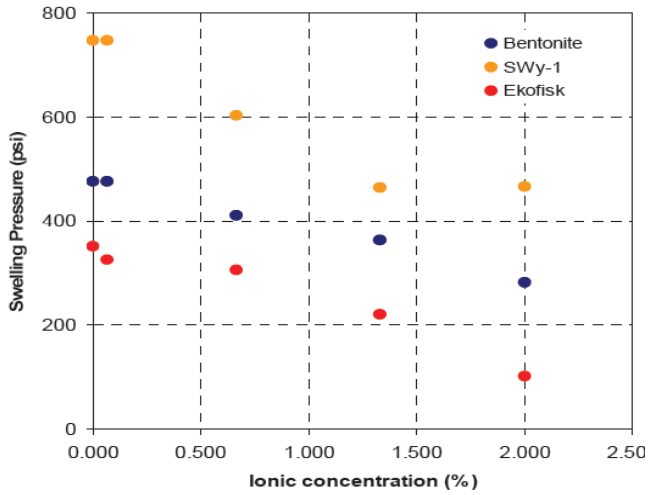

Figure 2.11: Swelling pressure measurements for various clays and shales (Mese, 2008).

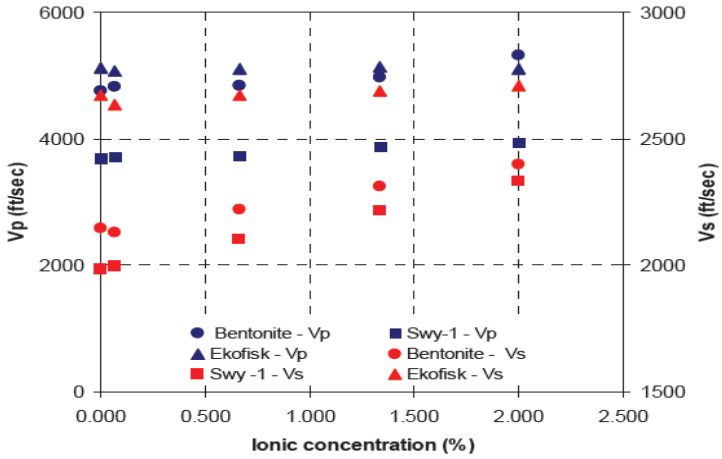

Figure 2.12: Ultrasonic velocities for pure clays and selected shales after Mese (2008).

The elastic properties of the STx-1 smectite and KGa-1b kaolinite that are used in our study were calculated by inverting the measured elastic properties of composite samples using the weighted Hashin-Shtrikman average by Wang et al. (1988) where they mixed the smectite with a material with known elastic properties. There is some error associated with the inverted data. However, the method seems to be good for handling the clays that could not not be tested

using the conventional ways. The calculated properties for the smectite and kaolinite are shown in Table 2-1 and Table 2-2, respectively.

Table 2-1: STx -1 smectite elastic properties inverted from weighted Hashin-Shtrikman average (Wang et al., 1998).

Property	Value	Property	Value
Grain Density (%)	2.338	Vs (m/s)	3250
Average K (GPa)	49.5	Poisson's Ratio	0.286
Average G (GPa)	24.7	Delta tp (micro s/m)	168.5
Vp (m/s)	5936	Delta ts (micro s/m)	307.7

Table 2-2: KGa-1b kaolinite elastic properties inverted from weighted Hashin-Shtrikman average (Wang et al., 1998).

Property	Value	Property	Value
Grain Density (%)	2.444	Vs (m/s)	2853
Average K (GPa)	47.7	Poisson's Ratio	0.317
Average G (GPa)	19.9	Delta tp (micro s/m)	181.4
Vp (m/s)	5511	Delta ts (micro s/m)	350.4

Smectite not only adsorbs water, but it also adsorbs hydrocarbons under certain conditions. Zhang et. al (2012) conducted NMR experiments for smectite/hexane and smectite/butane samples. They showed that the hexane and butane can condense in the

intercrystalline pore space of the smectite at or below the saturation pressure. Their results suggest that smectite can be oil wet in the absence of water and mixed wet in its presence. Moreover, their results showed that the hexane adsorption is reversible, such that the liquid can be released from the pore space when the partial pressure drops. The T_2 peaks for a sample saturated with hexane from their study are shown in Figure 2.13. The immediate measurement represents the adsorption of hexane and the other shifted peaks represent the desorption process. The measured weight of the sample versus the T_2LM (T_2 logarithmic mean) and the experiment time is shown in Figure 2.14.

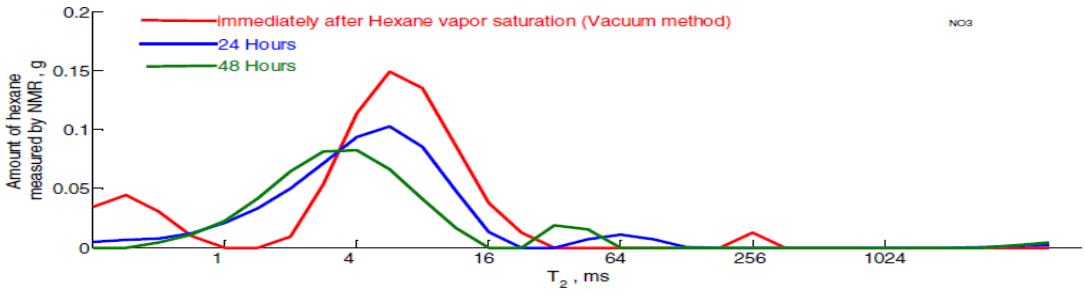

Figure 2.13: T_2 distribution for a hexane-saturated smectite sample at various times (Zhang et. al, 2012).

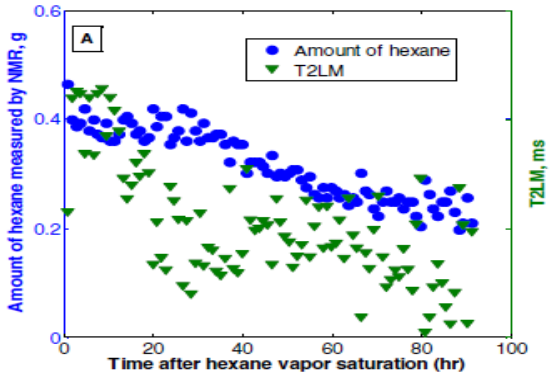

Figure 2.14: Amount of hexane weight vs. T_2LM and experiment time for the sample in Figure 2.13 (Zhang et. al, 2012).

Many factors and environmental conditions affect the swelling behavior of clays and particularly smectite that is the focous of our study. Besides the induced fluids salinity, temperature and effective stresses have been found to play significant role in the swelling tendency of smectite.

Young et al. (1962) studied the swelling pressures of sodium montmorillonite at depressed temperatures. They showed that the swelling pressure decreases with decreasing temperature. This conclusion agrees with the physical model of the diffuse ion-layers which assumes that when ions have high thermal energy, they cannot easily orient in the field of charged surfaces, consequently resulting in an extension over a distance from these surfaces.

The Pore-Platelet Unit (PPU) model has been used to find a relationship between the swelling behavior of shales and the surrounding stresses. The model divides the water in clay (as a part of shale) into two connected bodies: platelet water between the clay layers and the shale pore water in the pore space (Figure 2.15). An equation has been defined for drilling application as shown in equation 2.11.

$$\left(a_{w,platelet}\right)_{avg} = a_{w,pore}\ \exp\left(\frac{Vmw}{RT} * \left(\frac{\sigma v+\sigma H+\sigma h}{3} - P_0\right)\right) \qquad (2.11)$$

where a_w is the water activity, V_{mw} is the water molar volume, R is the gas constant, T is the temperature and P_0 is the pore pressure. The average platelet water activity can be interpreted as the shale water activity. According to this equation, the stresses on the shale act on the clay platelets which are the part of the shale matrix and the effective stress term is derived from the differential pressure between the platelet and pores (osmotic pressure differential). The more stress acts on the shale (less confining pressure), the more water moves from platelet to the pore space (Wang, 2010).

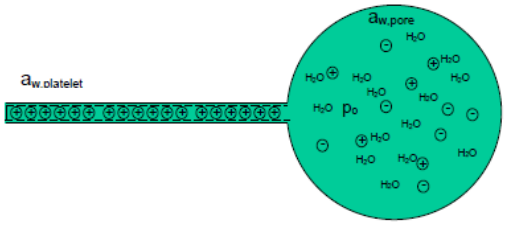

Figure 2.15: Platelet-Pore Unit (PPU) schematics (Wang, 2010).

Other models for the water adsorption and desorption of shale show the effect of the confining pressure. Yew and Wang (1992) indicated that the water adsorption/desorption is affected by confining pressure, Pc, and used equation 2.12.

$$e = \frac{1}{3K} Pc \tag{2.12}$$

This is based on earlier experiments by (Osisanya, 1991) where e is dilation and K is bulk modulus of shale.

$$\in m = \frac{1}{3K}\left(\frac{RT}{arKc} - Pc\right) \quad \text{for ar <1 (adsorption)} \tag{2.13}$$

$$\in m = \frac{1}{3K}\left(\frac{RT}{arKc} + Pc\right) \quad \text{for ar >1 (desorption)} \tag{2.14}$$

where $\in m$ is the induced strain, ar is the relative water activity that can be calculated from the ratio of the shale water activity to pore fluid activity as ar = aw_{shale} / aw_{pore}, Kc is one of three slopes from the dilation versus ar plot, Figure 2.16.

Prammer et al (1996) studied the NMR response of various clays at 2MHz NMR set-up. Ranges of T_2 values were determined for different clays. Kaolinite clay had relaxation T_2 values varying from 8 to 16 ms, illite clay had T_2 values of about 1 ms whilst montmorillonite clay had values from 0.3 to 1 ms as shown in Figure 2.17. They suggested that the T_2 peaks positions may

be used to determine the clay types in the tested samples. In their study, the resulted T_2 distributions had multiple peaks with early T_2 peak representing the clay bound water.

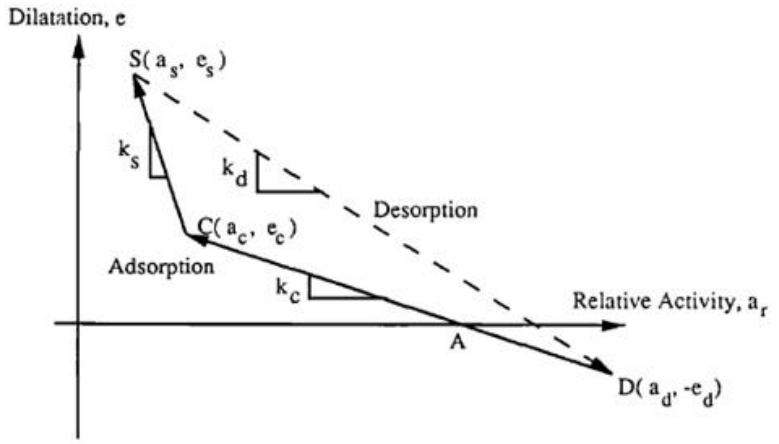

Figure 2.16: Dilation versus the relative water activity (Yew and Wang, 1992).

clay ID	water weight per dry clay weight (%)	NMR visibility at Te=0.5ms (%)	T_2 of clay-bound water at Te=0.5ms (ms)	apparent ρ_2 surface relaxivity (μm/s)	remarks
SWy-2	7.0	20	-	-	T_2 < 0.2ms
	18.9	90	0.3	1	
	31.1	100	0.5	1	
	54.4	100	1	0.9	T_1 = 1.5ms
IMt-1	8.8	90	1	0.9	
	15.8	100	2	0.8	
KGa-1b	11.7	100	8	0.8	
	17.4	100	12	0.8	
	20.0	100	16	0.7	T_1 = 30ms
CCa-2	7.5	100	5	0.4	ρ_2 may be too low due to overestimated surface area

Figure 2.17: Measured clay bound water T_2 (Prammer et al., 1996).

On the other hand, a study on clays conducted by Matteson et al. (2000) had an opposite conclusion. Several brine/clays samples were tested under compaction and all the clays tested showed only one peak in their T_2 distributions that shifts to the left toward the faster relaxation times as compaction increases as illustrated in Figure 2.18. They thought having one peak might be a result of the effective diffusion of the fluids in the samples.

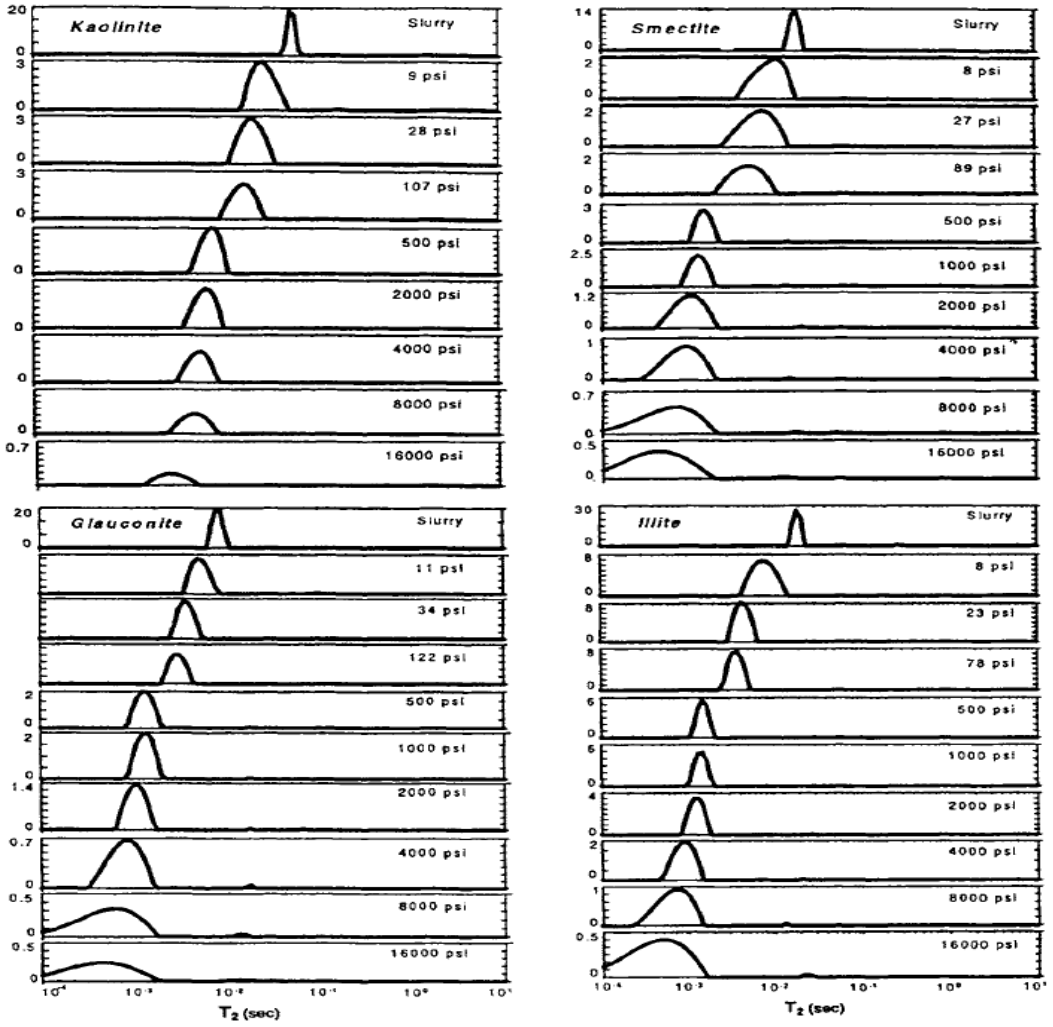

Figure 2.18: T2 behavior for various clays under compaction (Matteson et al., 2000).

Detecting faster relaxations when compacting the sample as reported by Matteson et al. (2000) might be explained by the increase in the surface relaxation as the volume of pores decreases with the assumption of constant surface area. Moreover, the diffusion theory might also be applicable. However, there is a possibility that these single peaks attribute to the fluid particles in the pore volumes between clay molecules and the inter-layered fluids were not detected.

The typical T_2 distribution of montmorillonite clays was studied by Chitale et al. (2000). They found that for the Ca-Montmorillonite and Na-Montmorillonite, the distribution of T_2 relaxation time is bi-modal with two peaks; the fast relaxation time for the clay bound water and the slow relaxation time for the pore volume water. A typical T_2 distribution of hydrated montmorillonite is shown in Figure 2.19.

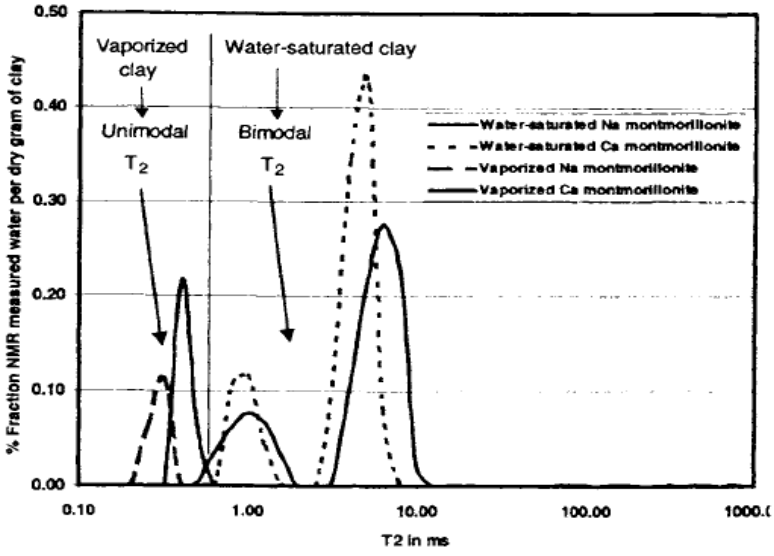

Figure 2.19: Typical unimodal and bimodal T_2 distributions of clays (Chitale et al., 2000).

2.4 Motivation to This Study

The swelling behavior of pure clays results in serious drilling and production issues affecting the developments of the unconventional hydrocarbon reservoirs (e.g. shale formations). Most of these problems are related to the instability caused by the liquid-clay interactions during the drilling and fracturing operations. The understanding of this behavior and tackling it from different angles will help to find the best preventive solutions.

By reviewing the literature of the clays and the NMR technique applications in the petroleum industry, it is evident that the NMR technique has not been widely used to describe the clay swelling behavior. Moreover, most of the reviewed NMR applications in the petroleum industry depend on the low field (1MHz or 2MHz) NMR measurements that don't have the capability to describe the main structural groups in the clay. The high field NMR can define the main groups in the structure, e.g. ^{1}H, ^{13}C, and ^{29}Si groups. It provides information on the chemical bond breakage or formation taking place under different conditions. Thus, the utilization of the high field NMR appears to have potential benefits in this matter. Moreover, studying the swelling mechanisms and using the relaxation time measurements and distribution curves to confirm them are of high importance to build better understanding of reservoir characterization. In addition, the high field NMR has the capability to investigate the interlayer (in nano-meter) and inter-particle pore spaces (in nano-meter) in the pure clays. The measurement methods used in the industry to estimate the porosity and pore throat sizes are summarized in Figure 2.20 (Nelson, 2009). Typically, the only method used in determining the porosity in unconventional formations with pore dimensions less that 1.0 nm is the computational chemistry method. The high field NMR application, with its high resolution and resistivity, provides information to study the porous systems in this range.

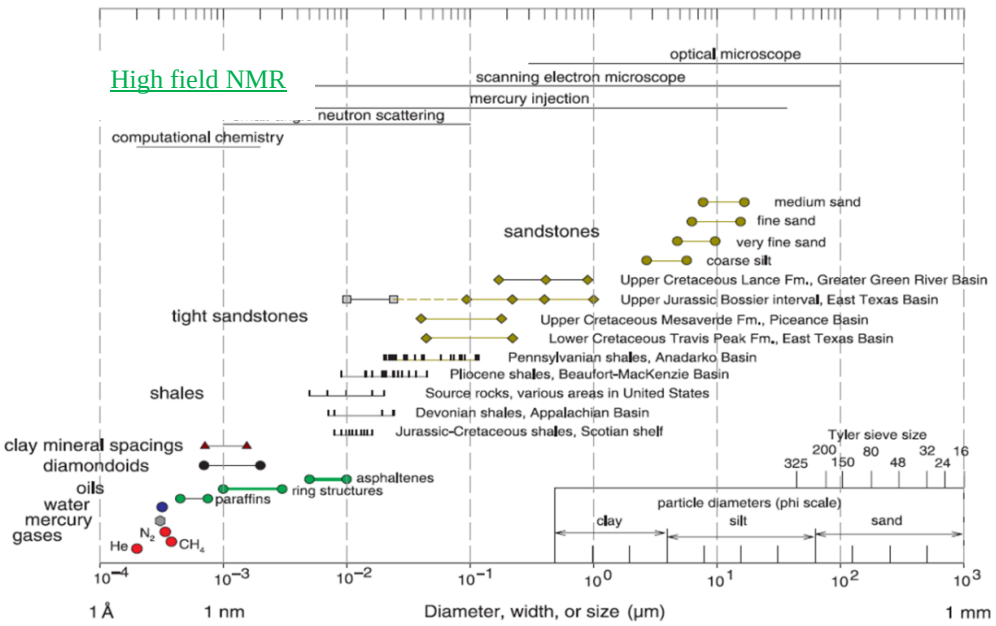

Figure 2.20: Sizes of molecules and pore throat in silicastic rocks. The measurements methods of different size ranges are shown at the top (Nelson, 2009).

In this study, the high field NMR equipment has been used to give a general description of the clay structure under saturation with different salt concentration liquids. Moreover, the relaxation time distribution curves have been used to confirm the swelling mechanism taking place in the clays based on the knowledge of their swelling behavior and the NMR relaxation mechanisms.

Our effort has been concentrated here on montmorillonite clay which has the highest affinity to liquids. However, to extend our findings to other clays and eventually to shales, we have conducted a few other experiments on kaolinite and Eagle Ford shale samples. Though these few tests are not enough to draw a full conclusion on these other clays and the shale studied, they provide valuable insight on the variability ranges of the NMR response on the selected clays and shales of this study.

CHAPTER 3

EXPERMENTAL STUDY

Evaluating the feasibility of utilizing the high field NMR in petroleum engineering studies is an objective of our study. Therefore, both liquid and solid state NMR set-ups have been considered in this matter. Although most of the research has been performed using the solid-state NMR, some knowledge of the liquid state NMR has been built and its capability has also been evaluated.

In this chapter, the NMR instruments used will be introduced. Furthermore, details on the experiments conducted and samples used in the experiments will be shown. Several techniques are present in the industry to acquire NMR data. However, certain techniques, namely the MAS and CP techniques for the structure information and the CPMG and inversion recovery pulse sequences for the relaxation parameters, have been chosen due to their compatibility with the objectives of our study. These techniques will be discussed in later sections of this chapter.

3.1 NMR Equipment and the Experiments

The NMR equipment in the Chemistry Department at Colorado School of Mines has been used in this study to conduct two types of experiments: relaxation time determination and clay structure determination.

3.1.1 Liquid and Solid State NMR Equipment

The high field NMR equipment used in this study includes 500 MHz liquid state NMR and 400 MHz solid state NMR as illustrated in Figure 3.1. Generally, the high-frequency NMR provides higher resolution and the produced spectrum is easier to detect and analyze compared to the low frequency devices. The spectrum of the same substitute under different frequencies is shown in Figure 3.2. It is evident from Figure 3.2 that with the use of the higher frequency, the peaks of the spectrum are clearer and their patterns are more distinguishable, resulting in higher accuracy in our analysis. A clear advantage is observed in studying the chemical composition of the samples tested.

Figure 3.1: Liquid state NMR (left) and solid state NMR (right) used in this study.

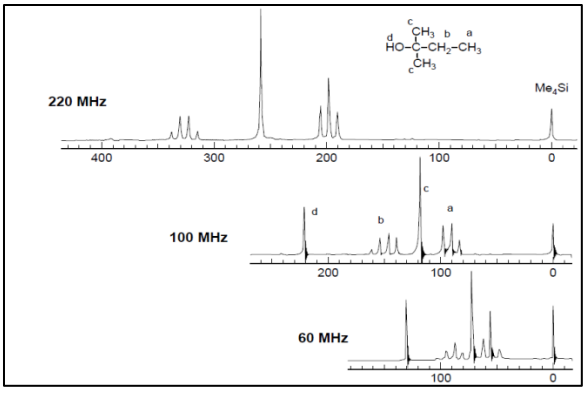

Figure 3.2: Example showing the advantage of the high frequency NMR for accurate analysis (Reich, 2012).

The main NMR instrument used in our study is the Bruker Avance III (400 MHz, solid state) device. Two probes are used to run the experiments: A 4 mm triple resonance MAS probe and a 5 mm double resonance z-gradient diffusion probe. The magnetic field of this instrument is very high compared to the conventional 1 or 2 MHz fields typically used in the petroleum engineering applications.

The advantages of the higher field solid state NMR include providing higher resolution for the detected spectra, more sensitivity to various atoms other than the protons (e.g. ^{13}C and ^{29}Si), better magnet homogeneity throughout the sample, and more frequency preservation as the temperature is preserved (Yang, 2012). The clay samples used in this study are silicon-rich making it more practical to study their silicon spectra. Because they are acquired from Clay Mineralogical Society as pure reference clays to be used for research purposes, they do not contain any carbon. Moreover, the temperature can be varied from -220^{o} F to 310^{o} F enabling to study the effect of temperature on the NMR response. One possible disadvantage of the high field NMR is its sensitivity to paramagnetic materials, which potentially might affect the detected response.

3.1.2 An Example for Determining the Chemical Composition

Determination of the chemical composition of the samples tested, including defining the proton and carbon groups, is one of the main objectives for conducting NMR experiments. Two liquid samples have been tested and their spectroscopies were analyzed to determine how the functional groups are distributed and linked within these samples. One of these measured liquids is Ethylbenzene (C_6H_{10}) and its chemical structure and NMR H-spectrum are shown in Figure 3.3. Utilizing the NMR analysis techniques enables determining the number of proton groups in the compound. For example, the third pattern in the figure includes three peaks

indicating the proton attached to two other protons on an adjacent carbon, referring to the proton in CH_3 that is linked to the two other protons in the adjacent CH_2. In some cases when the carbon spectrum is analyzed, more advanced techniques, e.g. Distortionless Enhancement by Polarization Transfer (DEPT), are used to determine which carbons have no communication with protons and which ones are parts of CH_1, CH_2, or CH_3 groups.

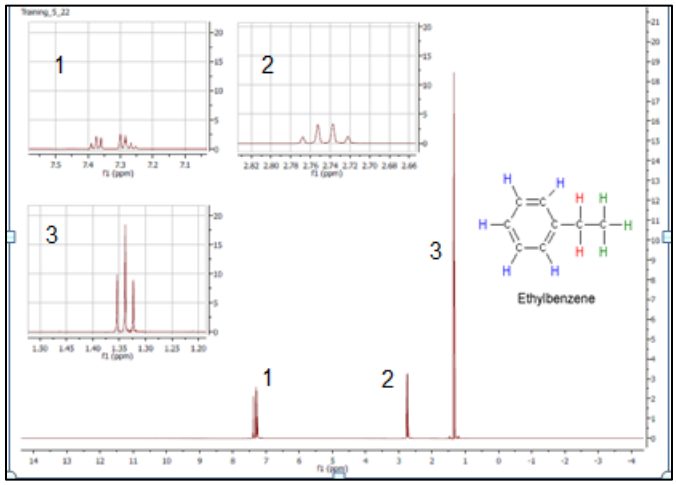

Figure 3.3: Example of structure determination (H-Spectrum for Ethylbenzene)

Sometimes, the conventional 1-D NMR analysis is not adequate to give a conclusion about the chemical composition. In such cases, a 2-D analysis is required. Two common types of the 2-D analysis are mostly used in the NMR laboratories: COSY (correlation spectroscopy) which determines the bonds between atoms of the same type like proton-proton, and HetCor (heteronuclear correlation) which determines the bonds between different atoms like proton-carbon. An example of the COSY analysis is illustrated in Figure 3.4. This analysis, for example, basically provides a plot of the same spectrum on two axes. A contour level is chosen and then the peaks are displayed at this level. Cross peaks between the two spectra determine the bonds between different atoms. A double check indicator of this linkage is the symmetricity of the cross

peaks around the diagonal peaks line that also helps to avoid the small noisy peaks might be found scattered in the plot.

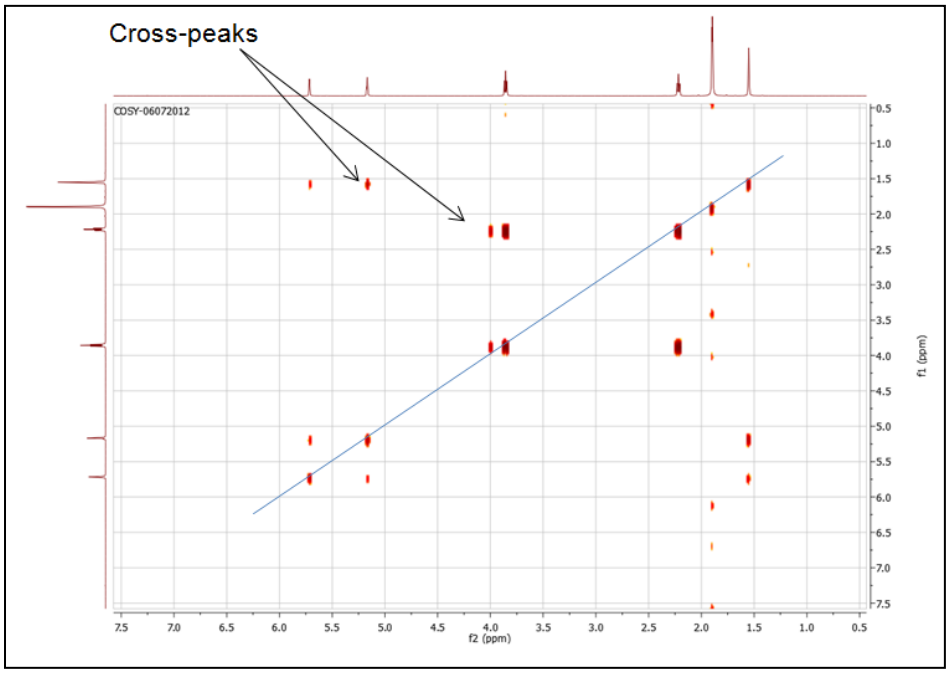

Figure 3.4: An example for COSY analysis.

The use of the liquid state NMR has been limited in our research. The solid-state NMR has been used extensively to determine the structure of the clays and shale samples of our research study. However, the significance and feasibility of using the high field liquid NMR have been illustrated by studying the structures of liquid samples in our limited number of high field liquid NMR measurements.

3.1.3 Types of NMR Experiments Used in This Study

Two types of NMR tests are considered in this study. They are discussed in the following paragraphs.

NMR Experiment Type 1: Experiments with Cross Polarization and Magic Angle Spinning (CP-MAS) pulse sequences to detect the chemical shifts of the compounds in the sample. The chemical shift is the resonant frequency of the nuclei related to a standard material. The positions and numbers of the chemical shift within the molecules provide good information about the different existing bounded groups. Our objective of performing these tests is to define the structure of the samples based on the type of nucleus being tested (e.g. ^{29}Si and ^{1}H).

NMR Experiment Type 2: These are the experiments with designed Inversion Recovery and CPMG pulse sequences to study the relaxation times. The preparation for these tests involves determining the main inputs for the optimum pulse sequences. The analysis of the relaxation data requires exponential curve fitting and mathematical transformation (usually inverse Laplace transformation) for the distributions.

3.2 Sample Types Used and Their Preparation

In this study, several pure clays and field shale samples have been prepared in such a way that the NMR response behavior can be distinguished and correlated to other petrophysical properties. This section talks about the samples we have used and their preparation stages.

3.2.1 Available Samples:

Three types of pure clays, namely kaolinite, illite and Ca-montmorillonite (smectite) and Eagle Ford shale samples have been used for experimental part of this research. The pure clay samples kaolinite (KGa-1b), Texas montmorillonite (STx-1b) and Illite are used in powder form and have been purchased from the Clay Mineral Society. Illite sample contains a ferromagnetic ion preventing the sample from spinning inside the equipment. Consequently, we were unable to test the pure illite samples in the NMR equipment we are currently using in our experimental

study. As the montmorillonite is a clay mineral that is a member of smectite group, montmorillonite and smectite will be interchangeably used in our study to describe the samples.

A preserved shale core plug (1.0 in diameter X 0.57 in length) obtained from an Eagle Ford well in South Texas has also been tested as part of the experimental part of this study. Based on X Ray Diffraction analysis (XRD), the shale sample has the following composition: 45% calcite, 28% quartz, 15% mica/illite, 7% kaolinite, < 3% plagioclase and feldspar, < 3% pyrite, and < 3% marcasite, all percents are per weight.

As montmorillonite is very prone to reaction with fluids, it is important to investigate the structure of the montmorillonite used in this study. The structure as provided by the source (Clay Mineral Society) is as follows: (Ca.27 Na.04 K.01)[Al2.41 Fe(III).09 Mntr Mg.71 Ti.03][Si8.0]O20(OH)4. From this reported structure, the formula of the sample can be written as (Ca, Na, K) 0.32 (Al, Mg, Fe, Ti) 3.24 (Si 8 O20) (OH) 4. Usually, the montmorillonite has layers of 3 sheets (in each layer). Each layer contains tetrahedral silica-octahedral alumina-tetrahedral silica sequence, as illustrated in Figure 3.5. These layers have negative surface charges due to the presence of silicate and the isomorphous substitution in which Mg substitutes Al leaving one oxygen atom free. These negative charges between layers attract water and cations.

The fluids chosen to saturate our clay and shale samples for this study are de-ionized water, 8% wt KCl solution, and 17.9% wt KCl solution. The tap water is used for few samples considering its ion concentration is above zero (DI water) and below the KCl solutions used. However, the accurate ion concentration of tap water is unknown. Therefore, it was considered equivalent to the DI water in the calculations of samples density and is used with conservation

in our data analysis giving it a molarity value of 0.001 M. The objective of choosing these concentration values to study the NMR response is that these values are within the ranges common in drilling and stimulation operations in petroleum engineering applications. The potassium chloride (KCl) solution has been known of its swelling preventive ability making it in our study more practical and feasible.

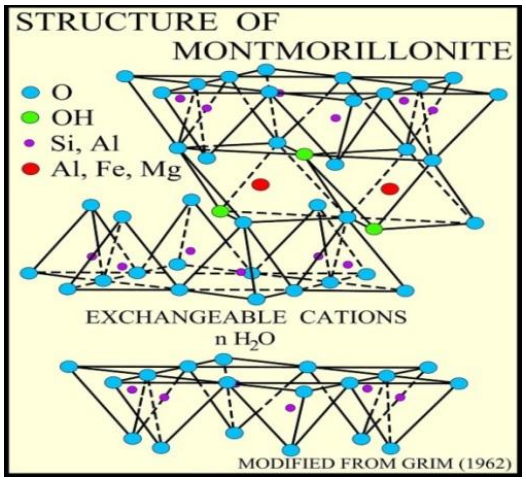

Figure 3.5: Illustration of the typical structure of montmorillonite (after pubs.usgs.gov).

3.2.2 Sample Preparation

To introduce the size and preparation tools of the NMR samples, the liquid NMR sample tube and the solid NMR rotor are shown in Figure 3.6 and Figure 3.7, respectively. For the liquid set up, the sample must be dissolved completely in the solvent. This expedites getting a clear spectrum. The results of the liquid NMR are usually collected within a few minutes. On the other hand, acquiring and analyzing the solid NMR is time consuming. The spectrum might take more than twelve hours to be achieved. The small rotor, less than 1 inch in length and 4 mm in diameter, must be carefully handled. The sample must be tightly and gradually packed into the

rotor to equally distribute the weight. As the rotor will be hanged in the space inside the probe, any misdistribution in the rotor's weight will shift the rotors and make it hit the coil and damage the whole set up.

Figure 3.6: Liquid NMR sample tube used in this study.

Figure 3.7: Solid NMR rotor used in this study.

Twenty four samples have been prepared for the T_1 and T_2 measurements. 14 of them are montmorillonite samples, 5 are kaolinite samples, and 5 are shale samples. De-ionized water, tap water, 8% wt KCl, and 17.9% wt KCl have been used to prepare the clay (shale) / water samples

for the measurements. Nine montmorillonite samples have been specially prepared to study the swelling behavior of the montmorillonite. As the NMR instrument was neither designed nor used originally to conduct swelling experiments, the sample preparation procedures followed, preservation of the samples to be tested, and the sample packing protocol into the rotors or tubes have been designed and executed to the highest degree of caution and accuracy.

Montmorillonite, kaolinite, and shale have been dried under vacuum at 100 ^{0}C for 24 hours. For preparing the clay/water samples, the water has been slowly added to the dry clay and stirred gently to obtain homogeneous mixtures. The prepared samples have been capped and covered with foil sheet to prevent any possible contact with the outside humidity. Once the test tubes prepared for the measurements, they have also been sealed with parafilm to prevent any humidity alterations.

The work station in the laboratory where the experimental work took place and the set-up used in preparation of the samples used in the measurements is shown in Figure 3.8. It is worth mentioning that the NMR instrument used for this study is designed to examine only very small amounts of samples in the 4 mm and 5 mm probes. Therefore, the shale sample has been ground and mixed with the different fluids to obtain the data discussed here similar to the pure clay measurements.

The details of the samples prepared for this study (mainly the relaxation times) are listed in Table 3-1. The weights of samples have ± 0.002 g error range. The shale samples have not absorbed all of the added water and a little excess amount of water has been poured from the sample later. Therefore, there is small error included in the liquid/clay ratio for the reported shale sample results. The density of fluids were taken as 1.00 g/cc for de-ionized water and tap water,

calculated 1.044 g/cc and 1.114 g/cc for 8% wt KCl and 17.9% wt KCl solutions, respectively. The density of the dry montmorillonite and kaolinite samples are taken as 2.338 and 2.444 g/cc, respectively, as calculated by inverting the measured elastic properties of composite samples using the weighted Hashin-Shtrikman average as also used by Wang et. al (1998). These samples are assumed to still have a portion of water as it not possible to dry the samples to zero porosity (e.g. 2.72 g/cc). The shale density was taken as 2.35 g/cc based on the GRI experiments conducted on a sample from the same depth interval. The ionic concentration for all the liquids used in this study have been carefully prepared in our laboratories as 0.0 for the de-ionized dewater, 0.001 for tap water (estimated), 1.12 M for the 8%wt KCl, and 2.68 for the 17.9%wt KCl.

Figure 3.8: A picture of the work station at NMR laboratory in the Chemistry department used in this study for measurements.

Table 3-1: Summary of the samples prepared for the experiments of this study.

Sample #	Clay Type	Liq. Type	Liq./Clay Wt. ratio	Sample Wt. (g)
1	Dry Smectite			0.204
2	Smectite	Di Water	1.273	0.357
3	Smectite	Di Water	0.969	0.400
4	Smectite	Di Water	0.874	0.369
5	Smectite	Di Water	1.176	0.413
6	Smectite	Tap Water	1.170	0.399
7	Smectite	17.9 KCl	1.269	0.391
8	Smectite	17.9 KCl	0.962	0.561
9	Smectite	17.9 KCl	0.872	0.482
10	Smectite	17.9 KCl	1.096	0.280
11	Smectite	8 KCl	1.270	0.584
12	Smectite	8 KCl	0.963	0.509
13	Smectite	8 KCl	0.873	0.505
14	Smectite	8 KCl	1.109	0.296
15	Dry Kaolinite			0.135
16	Kaolinite	17.9 KCl	0.596	0.883
17	Kaolinite	8 KCl	0.630	0.651
18	Kaolinite	Tap Water	0.478	0.822
19	Kaolinite	Di Water	0.492	0.715
20	Dry Shale			0.365
21	Shale	17.9 KCl	0.147	0.559
22	Shale	8 KCl	0.336	0.467
23	Shale	Tap Water	0.320	0.414
24	Shale	Di Water	0.268	0.507

3.3 Data Acquisition

Each experiment requires data acquisition techniques to obtain representative and reliable results. In this section, the different techniques implemented to obtain the NMR measurements are discussed.

3.3.1 Type 1 Experiment - Acquisition Techniques

For type 1 experiment (defining the structure of clays), the high resolution solid state NMR requires additional techniques to obtain a useful spectrum. When compared to the solution NMR, solid state anisotropic interactions are not suppressed and no distinct sharp peaks will be

visible on the spectrum. Thus, a few techniques are implemented. The solid samples must be oriented at an angle of 54.74^{o} with respect to the magnetic field to overcome the effects of the dipolar and chemical interactions; this is called the magic-angle spinning (MAS). Another technique is cross polarization (CP) where the polarization transfers from abundant nuclei to rare nuclei. The ^{1}H or ^{19}F are normally the abundant nuclei that are easier to excite and ^{13}C is an example of the rare nuclei. A key in obtaining efficient cross polarization is to set the match parameter of the atom investigated to that of ^{1}H or ^{19}F. This can be achieved by adjusting the frequency or the channel of the signal (^{1}H or ^{19}F) to match the nucleus we want to excite. For the energy to be transferred, both magnetic fields must be equal. If the frequencies are not matched, no coupling and no spectrum will be revealed (Schurko, 2009).

Moreover, with cross polarization the contact time could influence the results as some samples might require longer contact time (μs - ms). Dipolar interaction is common, where one nucleus interacts with another and both nuclei get excited by a magnetic field, and depends on the gyromagnetic ratio of the nuclei. The nuclei must be in contact for enough time to have full polarization transfer. This time is called the contact time and is illustrated in Figure 3.9. At insufficient contact time, only the nuclei with direct chemical bonds will be detected. Other interactions (e.g. with physically adsorbed water) will need more time to appear. In general, these interactions can be removed if we spin the sample at speed > 100 kHz (Yang, 2012).

Running Solid NMR requires adjusting the frequency, pulse, power, length of the signal, number of scans and contact time. Appropriate selection of these parameters lead to magnetization coherence where the noise is diminished and the signal is amplified helping to obtain more accurate results. Frequency (channel) can be adjusted manually. Pulse is dependent on the direction of the applied magnetic field and the plane we want to flip magnetic-axis of

nucleus to (90^o, 180^o, 270^o, 360^o). Signal power varies depending on the lab equipment (our equipment maximum output power is 50-Watts). The number of scans helps to eliminate noise and amplify the signal. Yet, too many scans require longer experiment time and an optimum number must be selected (Yang, 2012).

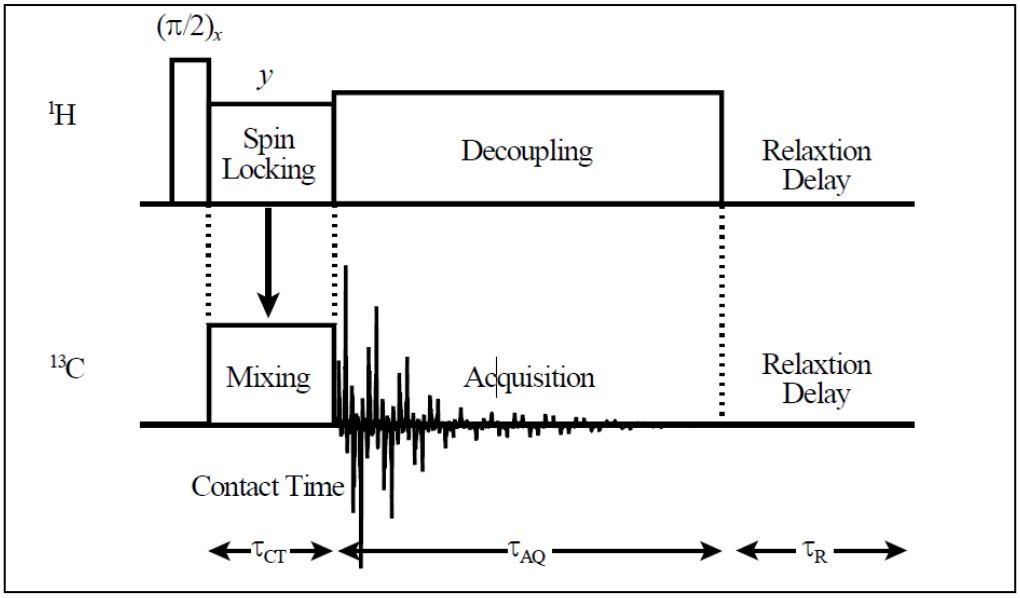

Figure 3.9: Cross polarization RF pulse scheme (Schurko, 2009).

3.3.2 Type 2 Experiments – Acquisition Parameters

For type 2 experiments, two common pulse sequences have been used to obtain the spin-lattice relaxation time , T_1, and the spin-spin relaxation time, T_2, measurements. They are the inversion recovery pulse sequence and CPMG (Carr, Purcell, Meiboom, and Gill), respectively. The inversion recovery sequence (180^o – tau – 90^o) is illustrated in Figure 3.10 and described in equation (3.1). The (tau) time is the time between the pulses. Different values of magnetizations (or signal amplitudes) have been measured at different (tau) times. The CPMG sequence (90^o – tau – [90^o, 2 tau]^n) is illustrated in Figure 3.11 and described in equation (3.2). Various

magnetization values (or signal amplitudes) have been measured at several times that create an echo train as illustrated in Figure 3.12.

$$A = Ao\ (1 - 2e^{-\tau/T1}) \tag{3.1}$$

$$A = Ao\ (e^{-t/T2}) \tag{3.2}$$

where τ is the time period between pulses and A is the signal amplitude.

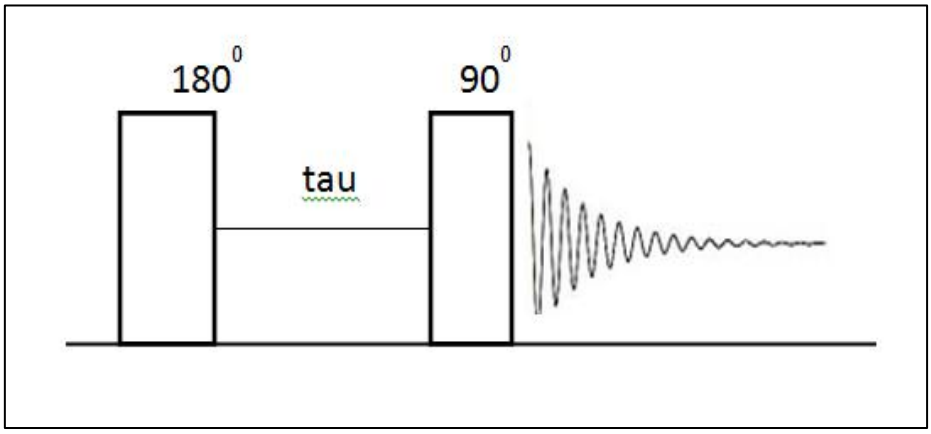

Figure 3.10: Inversion Recovery pulse sequence.

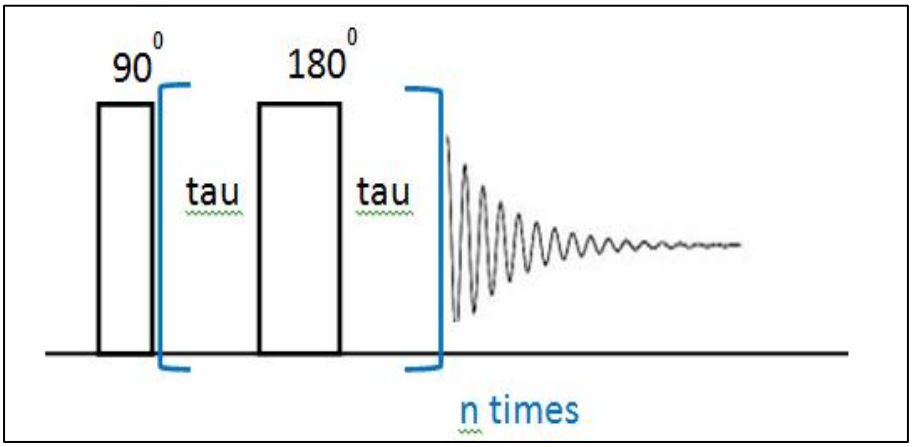

Figure 3.11: CPMG pulse sequence.

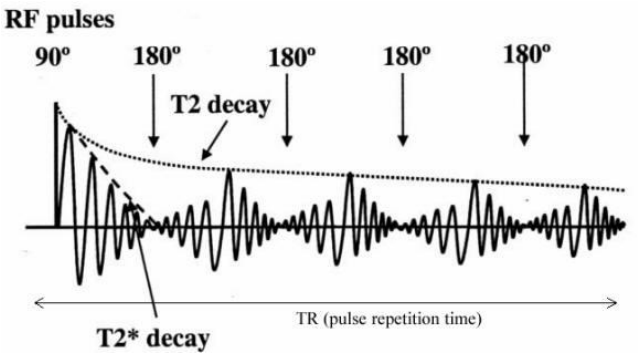

Figure 3.12: Echoes amplitudes decay for CPMG sequence (CNS, 2011).

The (tau) values used for T_1 acquisition and the (n) values used for T_2 acquisition in this study are summarized in Table 3-2. The 90^0 and 180^0 pulse lengths have been determined from after processing the ^1H spectrum of each sample. The pulse lengths and the measured relaxation times for the samples tested in this study are listed in Table 3-3.

Table 3-2: Tau and n parameters values used in inversion recovery and CPMG pulse sequences.

(tau) values for T_1 acquisition, ms			(n) values for T_2 acquisition		
Smectite	Kaolinite	Eagle Ford Shale	Smectite	Kaolinite	Eagle Ford Shale
1	3	3	1	1	1
3	8	8	2	2	2
8	10	10	3	3	3
10	18	18	4	4	4
18	25	25	5	5	5
25	35	35	8	8	8
35	45	45	9	9	9
45	50	50	10	10	10
50	100	100	13	13	13
100	250	250	15	15	15
250	500	500	20	20	20
	750	750	50	35	35
	1000	1000		50	50
	1250	1250		75	75
	1500	1500		100	100
	1750	1750			125

Table 3-3: Pulses lengths and measured relaxation times.

Sample #	Clay Type	Liquid Type	90 pulse, 10e-3 ms	180 pulse, 10 e-3 ms	T_1, ms	T_2, ms
1	Dry Smectite		5.000	10.000	NA	0.461
2	Smectite	Di Water	5.625	11.250	20.284	0.614
3	Smectite	Di Water	5.875	11.750	19.562	0.569
4	Smectite	Di Water	5.875	11.750	17.36	0.544
5	Smectite	Di Water	5.875	11.750	21.461	0.628
6	Smectite	Tap Water	6.000	12.000	19.033	0.527
7	Smectite	17.9 KCl	6.750	13.500	19.955	0.521
8	Smectite	17.9 KCl	6.937	13.874	18.462	0.450
9	Smectite	17.9 KCl	6.688	13.375	20.231	0.511
10	Smectite	17.9 KCl	6.570	13.140	17.497	0.430
11	Smectite	8 KCl	6.875	13.750	21.055	0.549
12	Smectite	8 KCl	6.750	13.500	18.355	0.495
13	Smectite	8 KCl	6.750	13.500	19.019	0.489
14	Smectite	8 KCl	5.875	11.750	21.75	0.692
15	Dry Kaolinite		5.000	10.000	177.899	0.519
16	Kaolinite	17.9 KCl	7.050	14.100	162.825	1.640
17	Kaolinite	8 KCl	6.875	13.750	161.066	1.792
18	Kaolinite	Tap Water	5.060	10.120	165.623	1.726
19	Kaolinite	Di Water	5.000	10.000	171.76	1.863
20	Dry Shale		4.625	9.250	NA	0.720
21	Shale	17.9 KCl	6.750	13.500	375.683	19.467
22	Shale	8 KCl	6.750	13.500	422.581	35.146
23	Shale	Tap Water	4.938	9.875	403.22	16.002
24	Shale	Di Water	4.625	9.250	191.253	2.206

3.3.3 Data Reproducibility and Variable Temperature Effect

The data reproducibility and the effect of variable temperatures on the experimental results, several T_1 relaxation measurements have been obtained for these particular objectives. Sample 14 (smectite and 8% wt KCl) has been tested at different temperatures from 30 ^{0}C – 55 ^{0}C (86 ^{o}F – 131 ^{o}F). The results showed that the T_1 value increases linearly about 0.5 ms every 5 ^{0}C, as shown in Figure 3.13. Moreover, two tests have been repeated to check the reproducibility of these experiments.

The same sample has been tested at a temperature of 27.2 ^{0}C twice giving T_1 values of 21.75 ms and 21.65 ms and at a temperature of 35 ^{0}C giving 22.66 ms reflecting a ± 0.1 ms of an uncertainty. As all of the experiments have been run at the room temperature of 27 ± 0.5 ^{0}C reflecting a variation range of ± 0.05 ms in the measured T_1 values, the anticipated relaxation time variation of our measurements are ± 0.15 ms in T_1 measurements. As the T_2 values are very small compared to T_1 measurements, in ranges of 0.4 to 5 ms, a same proportion of uncertainty with the temperature variation during the experiments should be also considered for the T_2 values.

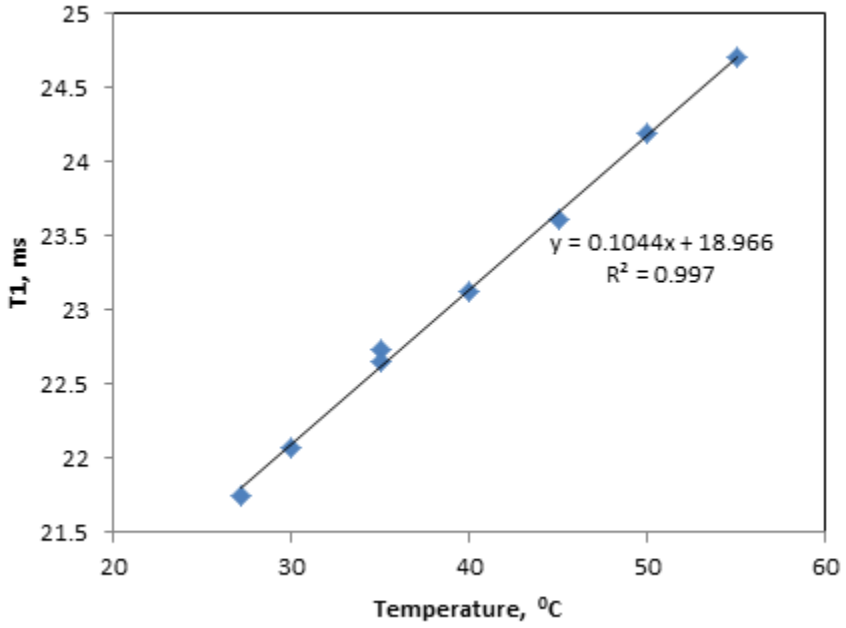

Figure 3.13: Temperature variation effect on T_1 measurements.

CHAPTER 4

RESULTS AND DISCUSSION

The experimental data of this study provides valuable information about the structure of the clays and shale samples at their dry and saturated state. Such information helps to understand the effect of salt concentration in solutions on these pure clays. Moreover, the distributions of the transverse relaxation times provide vital clues on the porosity distribution in the samples measured. This information can be then correlated to the swelling mechanisms and the structural alteration for understanding the swelling behavior in clays and shales.

In this chapter, the structure of the clay samples tested will be discussed based on the obtained NMR spectra and the relaxation time distributions will be shared with associated interpretation of the data.

4.1 NMR Spectra for Structures

In this section the obtained proton (^{1}H), carbon (^{13}C), and silicon (^{29}Si) from the tested samples will be summarized and discussed.

4.1.1 Quick Look into the Structure of Dry Samples

The pure clay samples are silicon-rich, which have better feasibility to study the silicon spectra. Several tests have already been completed for kaolinite, montmorillonite and Eagle Ford shale samples to analyze the chemical shifts from the spectra and to determine the contributing hydrogen and silicon groups. Oven-dried and as-is kaolinite samples were tested and no major

difference between the spectra was detected. However, for the montmorillonite samples, some differences in the intensities have been detected as this clay type is known to be highly reactive.

The ^{1}H spectra for the montmorillonite are shown in Figure 4.1. The detected single peak is of the OH group in the clay structure and the clay bound water. Because of the strong H-H dipole interaction, the two peaks overlay each other. The smaller peaks around the main peak, marked with (*), are spinning side bands related to the spinning speed of the sample during the measurement.

Multi-contact time ^{29}Si experiments were run to observe the effect of the contact time on the cross polarization process. Figure 4.2 shows the silicon spectra from the dry montmorillonite at three contact times that are the times required to transfer the polarization, as previously described, P15 = 1,000 micro seconds, P15 = 5,000 micro seconds and P15 = 8,000 micro seconds. In our study, we used P15 as referred by the equipment software as the contact time. The detected spectra are in the range of -104 to -120 ppm which is the range of the silicate SiO_4 group (Process NMR Associates, 2012). As shown in the three spectra, longer time was needed to see the peaks at – 112 ppm and -120 ppm. This multi-contact time experiments help in determining the right contact time needed for the pulse sequence design. It will also help to understand the total structure of the molecule. For example, in this case, we can infer that more proton atoms are surrounding the silicon atom at -112 ppm where much less protons are bonded to the silicon atom at -120 ppm.

The Eagle Ford shale sample's ^{1}H, ^{13}C, and multi ^{29}Si spectra have been obtained in as-is condition and shown in Figure 4.3. It is observed that a clear proton peak is attached by a little peak which can be considered a distinguishing peak for this Eagle Ford shale sample. The

observed ^{13}C spectrum has several possible peaks that are surrounded by a high noise level. However, a very clear single silicon peak was observed which reflects silicate SiO_4 or $(SiO)_3$ SiOH. The narrow line width of this peak indicates a good crystallinity (structural order) of this formation.

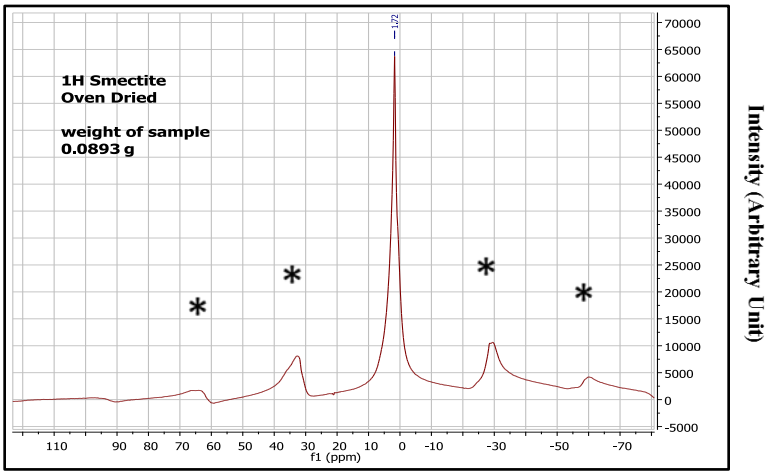

(a)

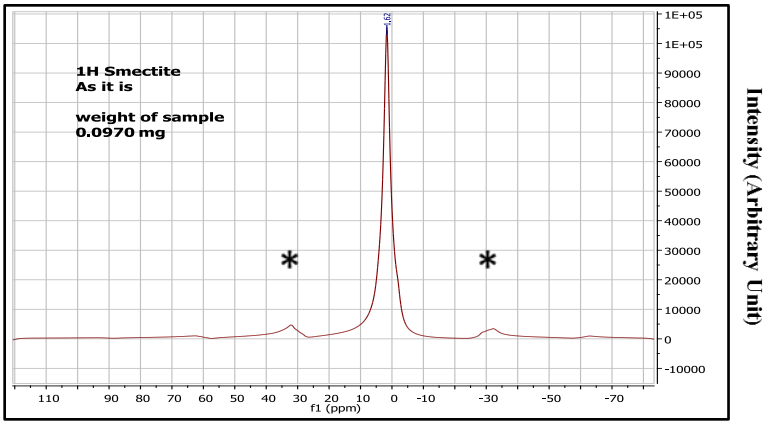

(b)

Figure 4.1: ^{1}H spectrum for montmorillonite, (a) is the dry sample and (b) is as-is condition.

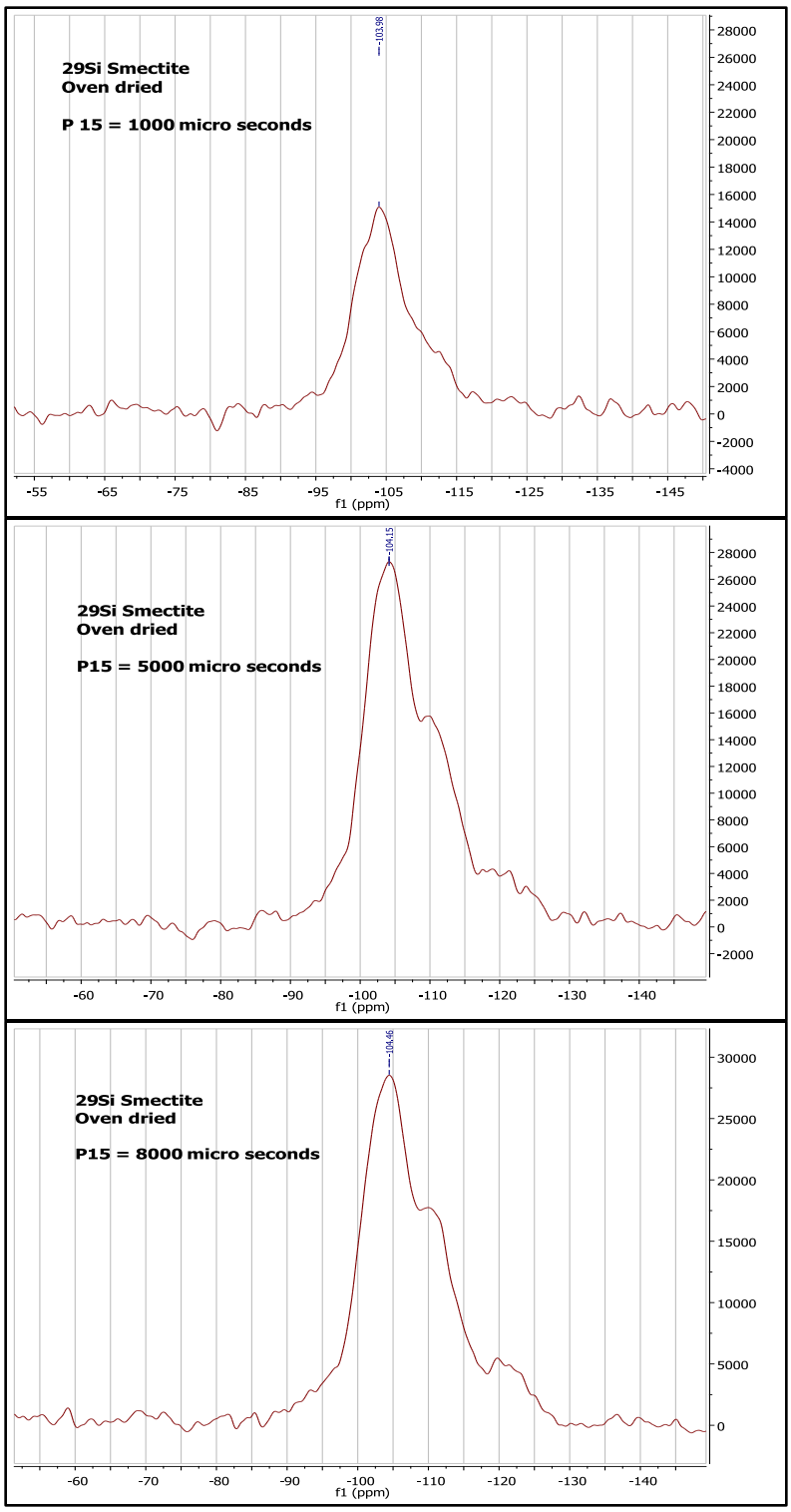

Figure 4.2: ^{29}Si Spectra for dry montmorillonite at three contact times of 1000, 5000, and 8000 micro seconds.

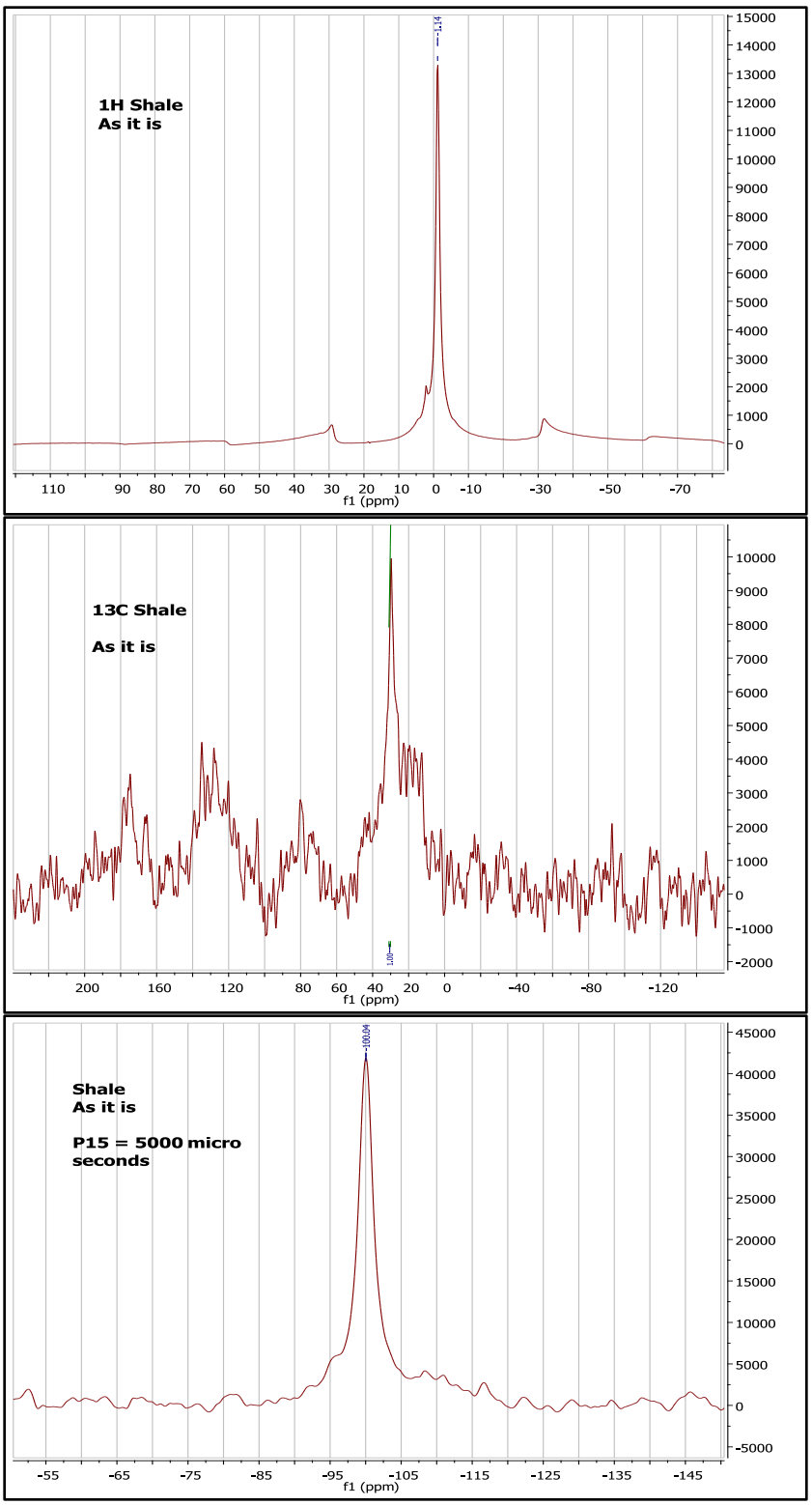

Figure 4.3: ^{1}H (top), ^{13}C, and ^{29}Si (bottom) for Eagle Ford sample.

4.1.2 The Effect of De-ionized Water and KCl on Montmorillonite and Shale

The silicon spectra for the montmorillonite sample at various saturation conditions have been obtained. The oven-dried, as received, DI saturated, and 8% wt KCl saturated spectra are shown in Figure 4.4 (A), (B), (C) and (D), respectively. The dry sample shows a mean peak at around -104 ppm which reflects Q4 (1Al) and an attached peak at around -110 ppm for Q4 (0Al). The latter peak has lower intensity (almost the half) and got separated from the main speak. In the case of the DI saturated sample, the second peak has completely disappeared. When saturating the sample with the 8% KCl, we noticed the presence of a peak at -101 ppm which reflects (SiO)3 SiOH. Such behavior of producing (SiO)3 SiOH has also been observed by Tkac et al. (1994) when they studied the Al and Si spectra of acid-treated montmorillonites (HCl-SWy-1). Although the KCl brine is not as strong as the HCl acid, the peak of (SiO)3 SiOH is clearly visible. We utilized the same peak values and silicon groups in our study. The 17.9% KCl saturated samples did not show any spectra suggesting that a major alteration in the structure of the clay took place. The bonds between atoms might been altered and the small iron content in the sample might then got free producing some paramagnetic effect and preventing the signal detection. The NMR properties, e.g. the surface relaxivity value, of the clay surfaces are dependent on the structure. An increase in the relaxivity value is expected as the iron content increases (Bryar, 1999). Any change in the structure should be taken in consideration when analyzing the NMR data as will be discussed in the next chapter.

The Eagle Ford shale sample has been saturated with DI water and 8% wt KCl and experiments conducted with these two fluids. The saturated responses of both fluids were similar to the dry sample, one sharp peak in the range of -100 to -104 ppm as shown in Figure 4.5.

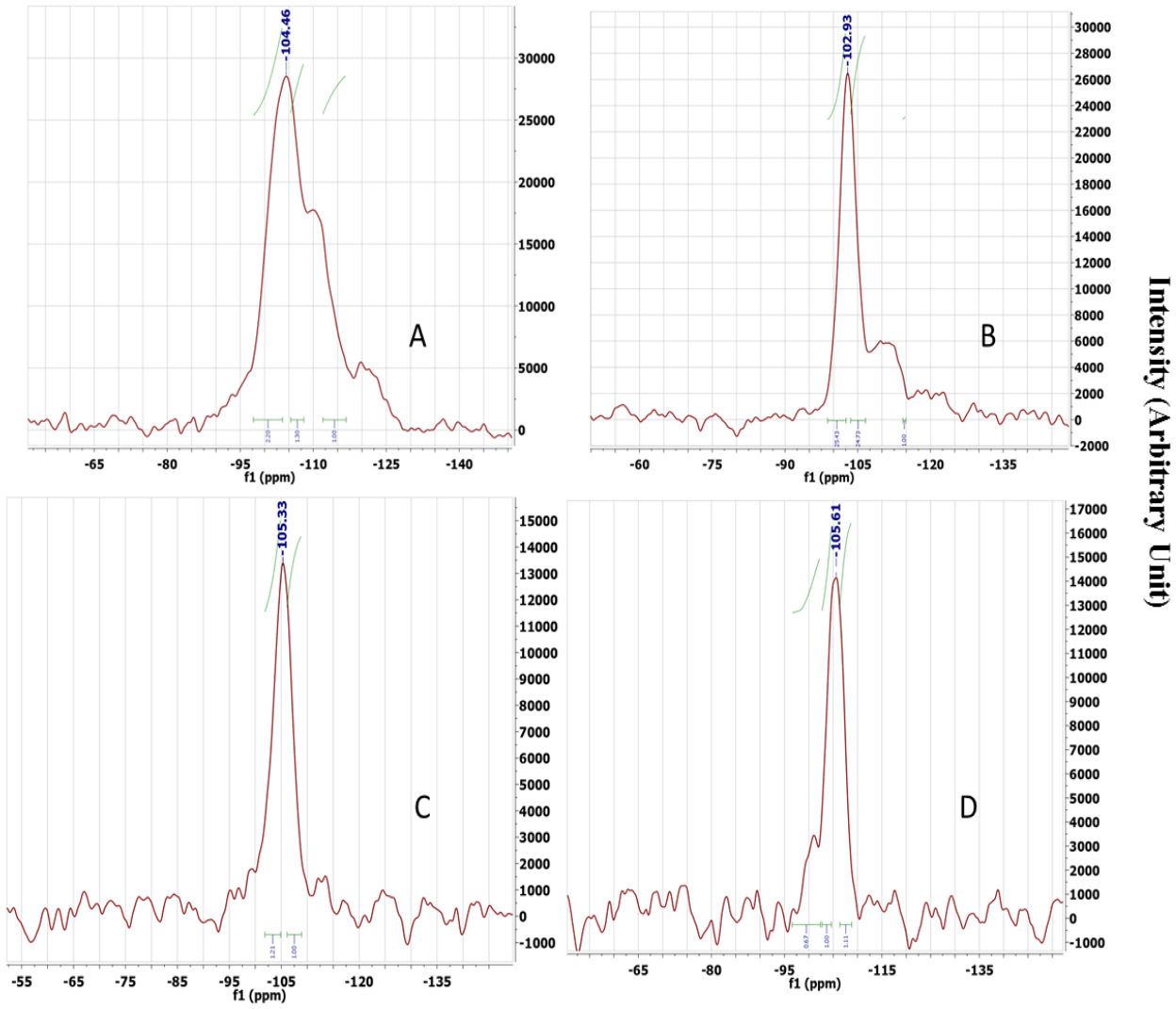

Figure 4.4: Silicon spectra for smectite samples measured at various saturation conditions (A) oven dried, (B) as-is, (C) DI water saturated, and (D) 8% KCl saturated.

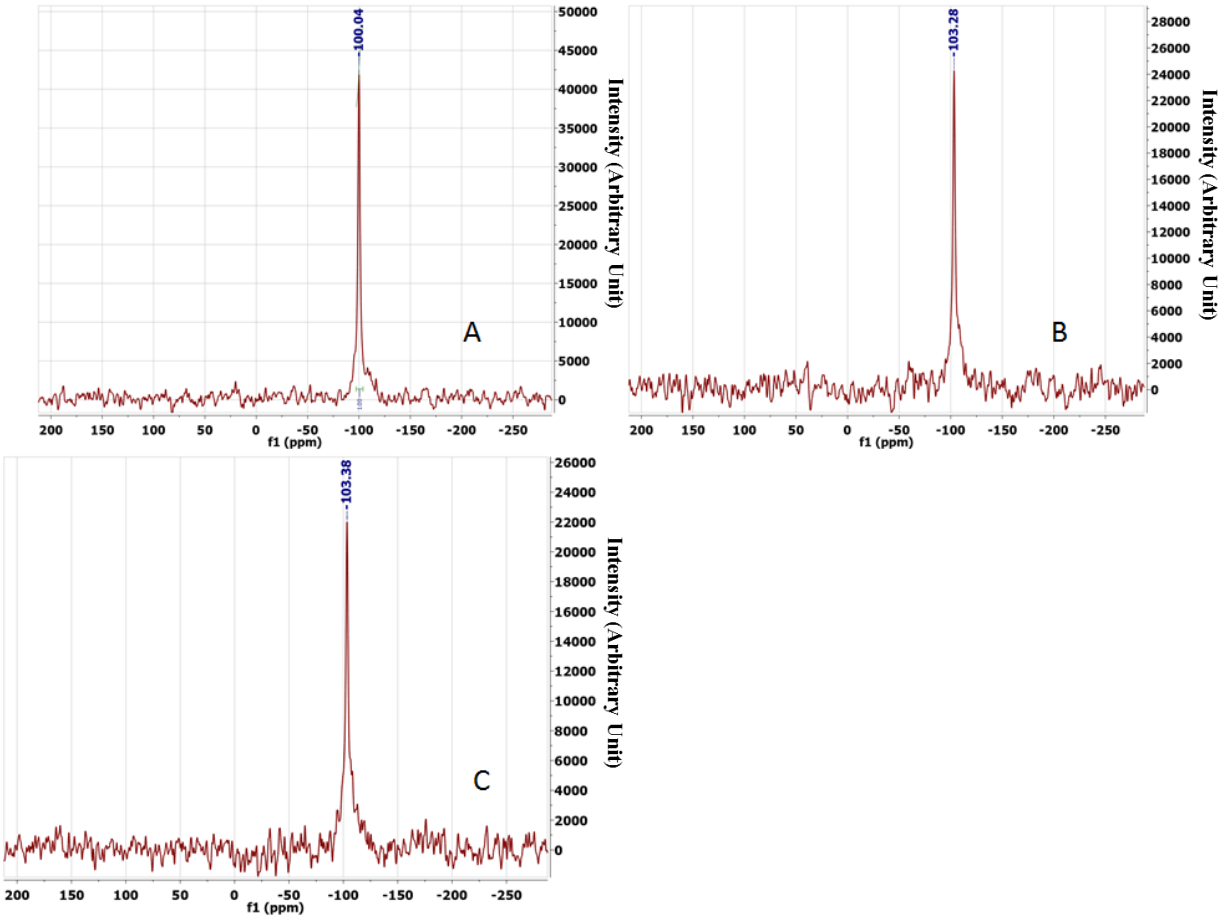

Figure 4.5: Silicon spectra for Eagle Ford shale samples measured at various saturation state. (A) as-is, (B) DI water saturated, and (C) 8% KCl saturated.

4.2 Relaxation Time Results

In this section the measured longitudinal and transverse relaxation times will be summarized and discussed.

4.2.1 Relaxation Times for Dry Samples

All the dry samples tested show a transverse relaxation time, T_2, of less than 1.0 ms. The value for the montmorillonite is 0.461 ms, while for the kaolinite, it is 0.519 ms and for the Eagle Ford shale, it is 0.720 ms. As these samples have been oven-dried at 100^0C under vacuum for 24

hours, most of the water between clays is presumed to be already evaporated. The signals detected from these samples are then mostly attributed to the clay inter-layer water that could be considered as the clay bound water. The T_2 values measured for montmorillonite agree to some extent with the data represented by Prammer et al. (1996) for the Na-Montmorillonite (SWy-2), shown earlier in Figure 2.17. However, they reached a value of 1.0 ms at a water to dry clay ratio of 0.54 (54.4 %) where in this study, the montmorillonite samples never indicated T_2 value of more than 0.678 ms. The water to dry clay weight ratios used for montmorillonite are 0.87, 0.97, 1.18, and 1.27 respectively. For the kaolinite clay samples, the measured transverse relaxation times are all greater than what has been reported by Prammer et al. (1996).

4.2.2 Relaxation Times for Saturated Samples

The relaxation times T_1 and T_2 for the tested samples are shown in Figure 4.6 for montmorillonite and kaolinite and in Figure 4.7 for the Eagle Ford shale samples. The data for all clay and shale samples is presented in Table 3-3. The salt concentrations used in our study are listed in Molarity units for easy comparison with other studies. The calculated molarity concentrations are 1.12 and 2.68 M for the 8% wt KCl and 17.9% wt KCl solutions, respectively. The red and blue circle symbols in Figure 4.6 represent four montmorillonite samples initially tested for the comparative study while red and blue hollow circle symbols illustrated refer to the samples used for the swelling characteristics of this study.

In general, the transverse relaxation time, T_2, values of montmorillonite are below 1.0 ms. For kaolinite, they vary between 1.640 and 1.863 ms. For the Eagle Ford shale samples, the T_2 relaxation times are between 2.20 and 35.15 ms range. The error bars are shown in the plots include the possible errors introduced in the measurements and data analysis in addition to the experimental procedure followed in this work.

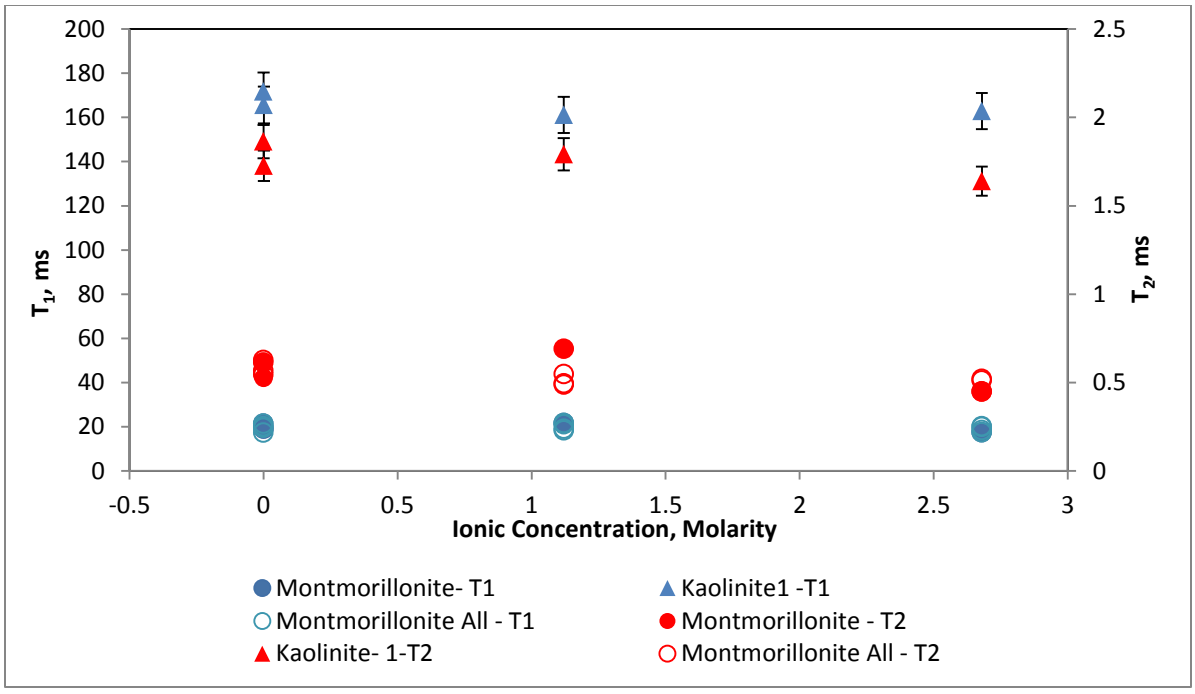

Figure 4.6: T_1 and T_2 relaxation times for montmorillonite and kaolinite samples measured in this study.

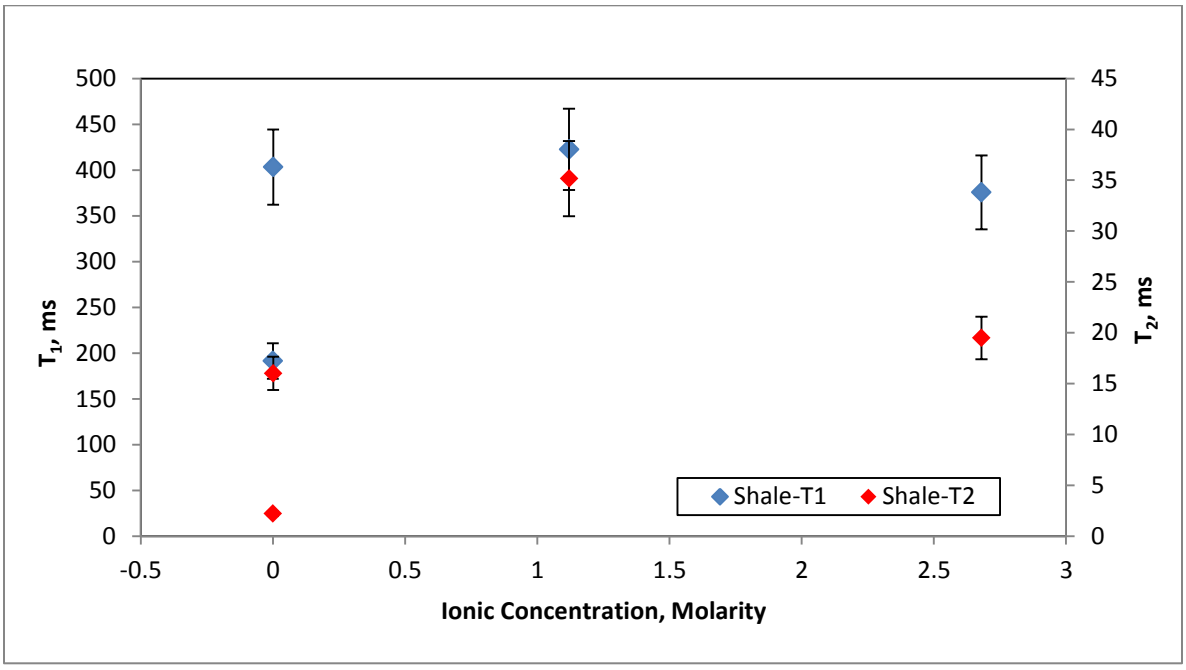

Figure 4.7: T_1 and T_2 relaxation times for the Eagle Ford shale measured in this study.

4.2.3 Relaxation Times Ratio – T_1/T_2

The ratio between the longitudinal and transverse relaxation times is of an importance in calibrating the logging tools. The behavior of this ratio for the three types of pure clay and shales samples studied in this thesis with various ionic concentrations is almost the same and did not indicate any significant change as shown in Figure 4.8.

Due to the inadequacy of waiting time between pulse sequences in the well logging operations, there is a need to apply a formation polarization correction factor which is a function of T_1 values. T_1/T_2 estimates are used to obtain T_1 values from the T_2 measurements. The default value for T_1/T_2 is 1.65 based on over 100 core plug laboratory measurements conducted by Kleinberg et al. (1993) with low field NMR. However, the accuracy of the derived porosity for carbonates and formations containing clay are largely affected by the T_1/T_2 ratio. T_1-T_2 2D NMR measurements showed a linear relationship between this ratio and T_2 measurements as presented in equation 4.1 (Sun et al., 2008).

$$\log\left(\frac{T1}{T2}\right) = a - b\log(T2) \qquad (4.1)$$

The experimental data of our study is obtained from individual 1-D T_1 and T_2 experiments. However, a linear relationship between T_1/T_2 and T_2 exists for all the samples tested as shown in Figure 4.9. , The relationship is linear both in log-log or Cartesian systems in spite of the experimental errors. For montmorillonite, the data shows that the ion concentration of the saturating liquid has no effect on the relationship between T_1/T_2 and T_2.

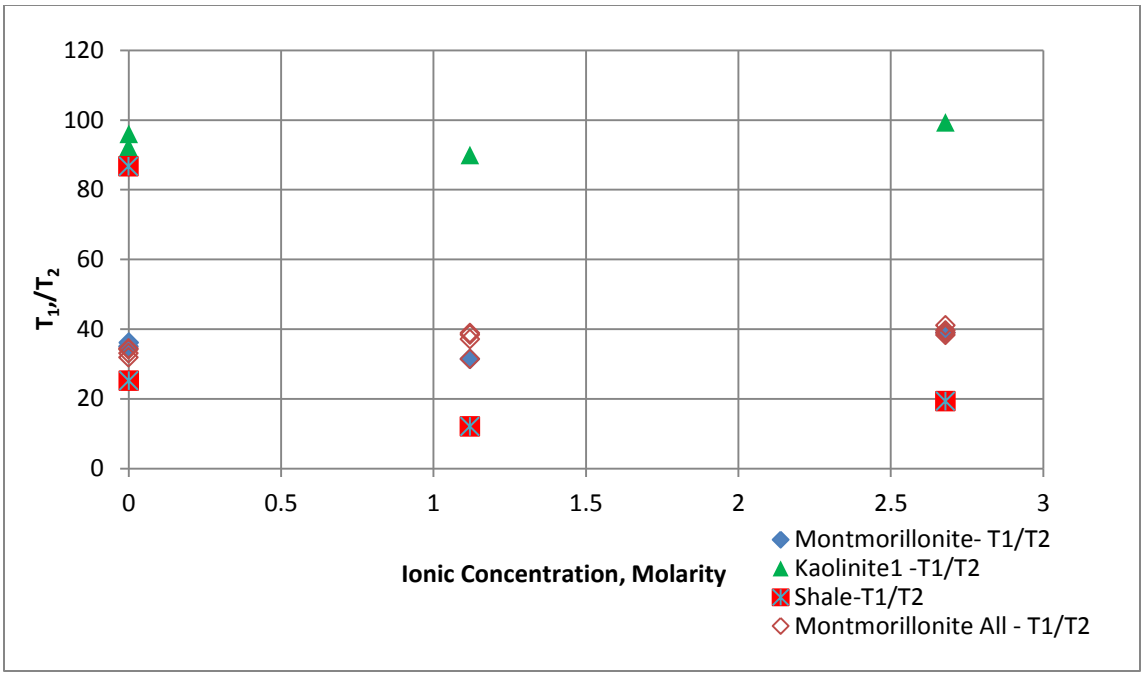

Figure 4.8: T_1/T_2 ratio for all the clay and shale samples tested in this study.

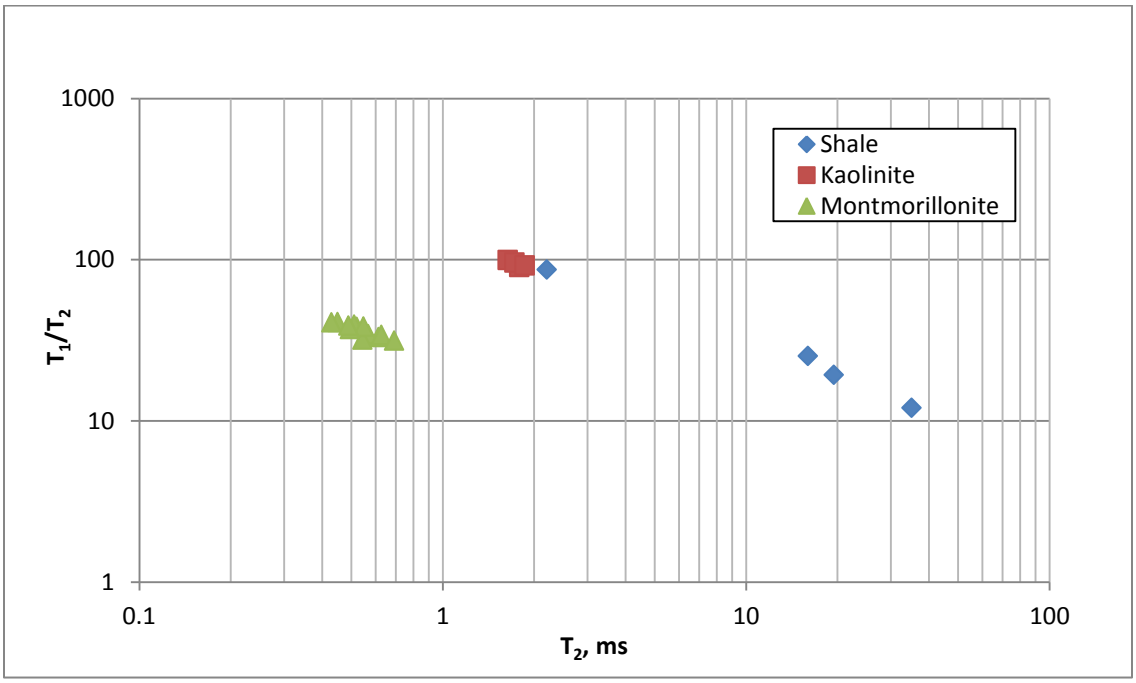

Figure 4.9: T_1 and T_1/T_2 relationship for the samples tested in this study.

4.3 Transverse Relaxation Time (T_2) Distribution Curves

A Matlab code (Marino, 2007) was used for obtaining the distributions of T_2 data in the studied samples. The code is called "rilt" that stands for regularized inverse laplace transform and has been downloaded from the Matlab file exchange site. This code is based on CONTIN regularized inverse Laplace transform method (Provencheher, 1982).

The distributions of the dry samples of smectite, kaolinite, and Eagle Ford shale show two peaks. The high peaks at fast relaxation times are less than one millisecond and small peaks are at longer relaxation times as shown in Figure 4.10. Since the samples have been dried before the experiments, the fast relaxation peaks represent the water filling the smallest pores in the samples that may be utilized as the clay bound water. The other small peaks represent small amount of water still residing within the bulk volume of the samples. It is noticed that the magnetization detected for the dry samples is greater than the magnetizations detected from the saturated samples. At this stage, no explanation has been offered for this phenomenon.

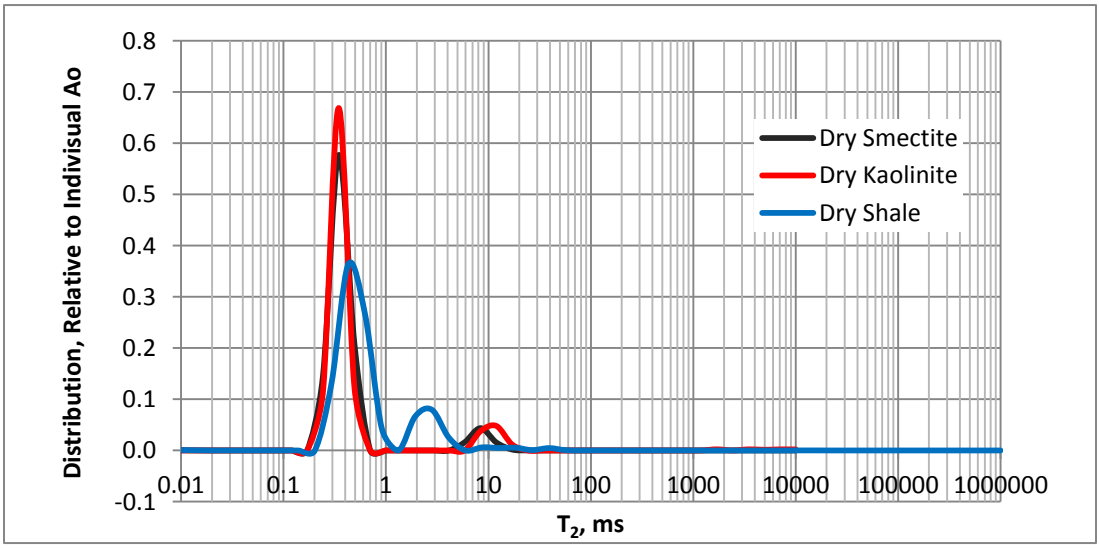

Figure 4.10: Two-peak T_2 distribution of the dry samples tested in this study.

For the saturated clay samples, only one general peak is noticed at a time longer than the first peak of the dry samples, as shown in Figure 4.11, Figure 4.12, and Figure 4.13 for the smectite and Figure 4.14 for kaolinite samples, respectively. Having only one peak might be a result of the effective diffusion between the water in the small pores and the bulk water, added to the sample, leading to having one common relaxation time. Same behavior has also been observed by Matteson et al. (2000) when they analyzed the relaxation of clay/brine mixtures at different stresses.

Because of our measurements are unique and conducted in a very high NMR field, having one peak in the relaxation times in our dataset, shifted a little to the right of the main dry sample peak, might be explained by either the saturation of larger pores in the system or by the effect of the induced internal field gradients that add the diffusion relaxation process term to the T_2 decay. In the latter case, assuming the surface relaxation that is a function of the pore surface to volume ratio is the dominant relaxation process might not be valid any more. However, the wait time (TE) between pulses in the acquisition pulse sequences was set to a very small value (0.20 ms) to minimize the diffusion contribution to the relaxation.

It is very important to understand how the diffusion might affect the relaxation process although its effect might be very small or negligible. In the presence of the diffusion effect, the nuclear spins shift from their initial positions due to the diffusive movement of the atoms. That causes additional magnetization decay, especially in the presence of high magnetic gradients. Having remarkable local gradients would let spins relax so fast, especially near the sharp corners of the grains (common for shale pores), leading to have shorter relaxation times. Moreover, in high magnetic field gradients, it might be difficult to record the short relaxation times, e.g. missing the short time peak in the distribution (Dunn et al., 2002).

The internal field gradients in the porous media are resulted from magnetic susceptibility contrast between the fluids and the sample material. This effect also increases with the strength of the static magnetic field, 400 MHz in our case, which could affect the study of the porous systems. This means that the observed T_2 reflects the free fluids diffused inside the pores rather than the spin interactions of the adsorbed fluids on the pore surfaces (Mitchell et al., 2010).

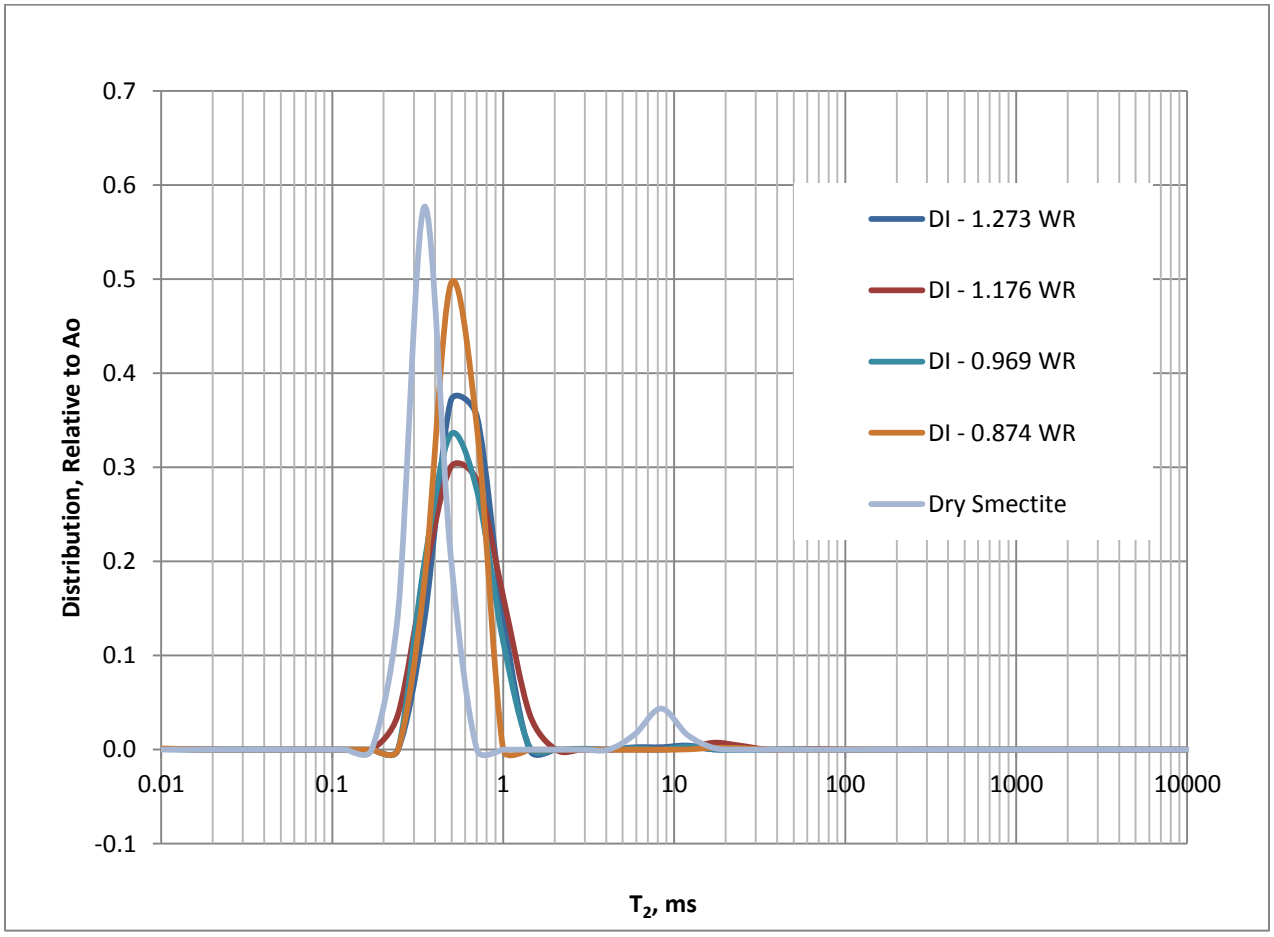

Figure 4.11: DI water saturated smectite samples T_2 Distribution compared to the dry sample (blue curve).

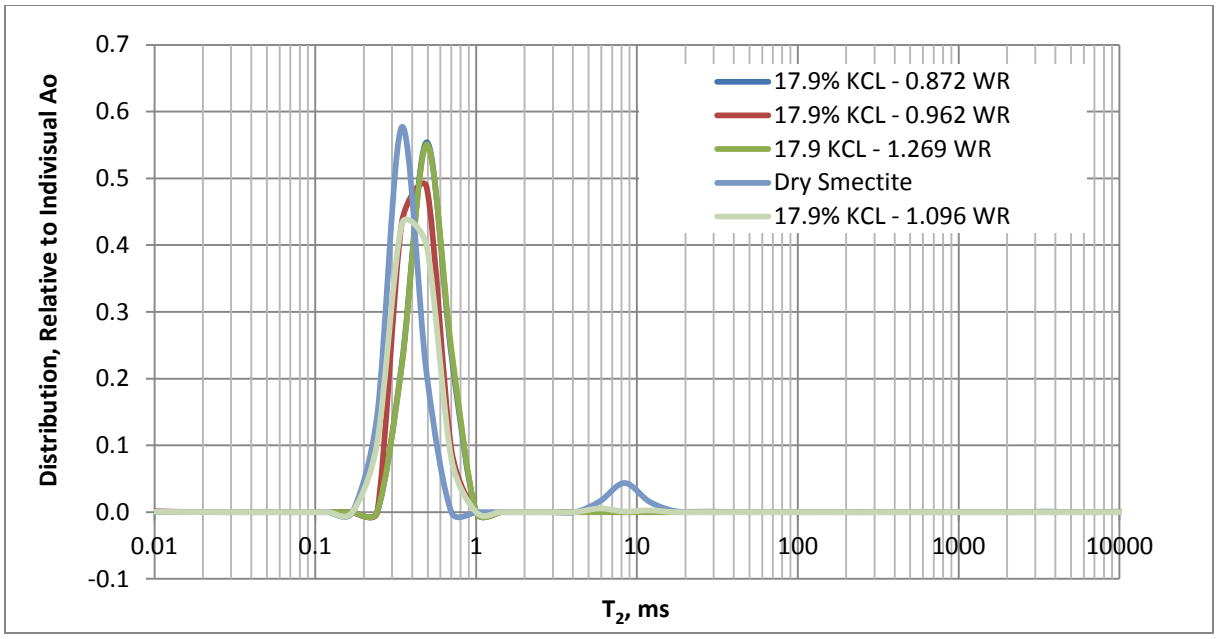

Figure 4.12: 17.9% wt KCl saturated smectite samples T_2 distributions compared to the dry sample (blue curve).

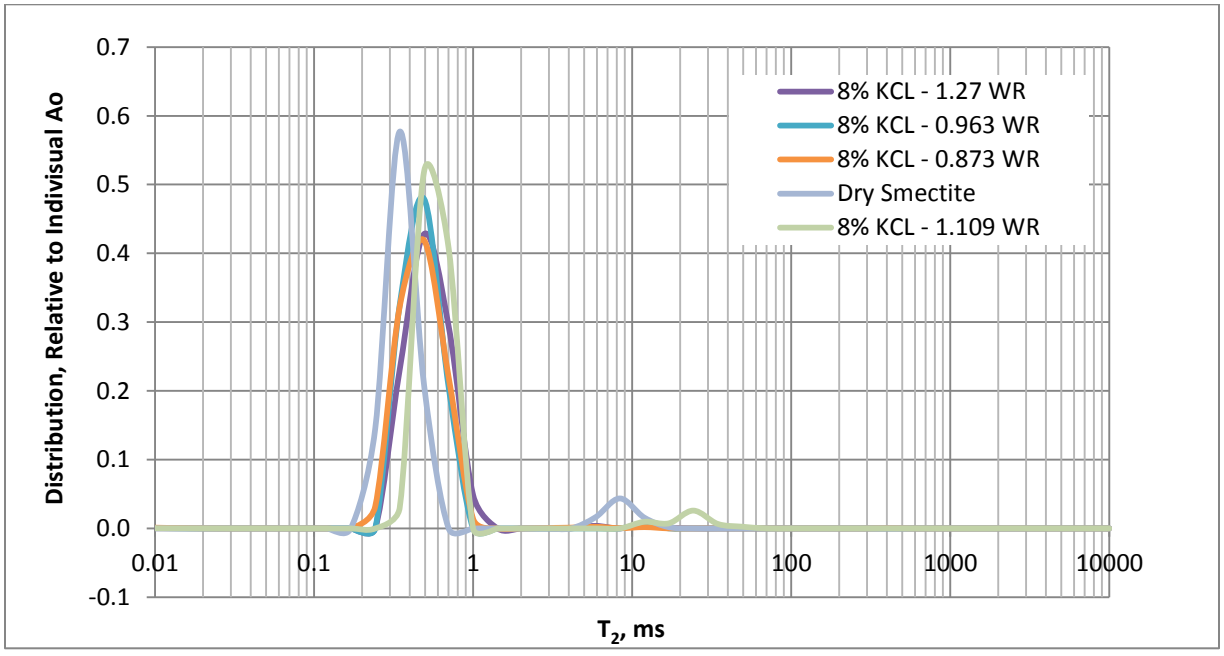

Figure 4.13: 8% wt KCl saturated smectite samples T_2 distribution compared to the dry sample (blue curve).

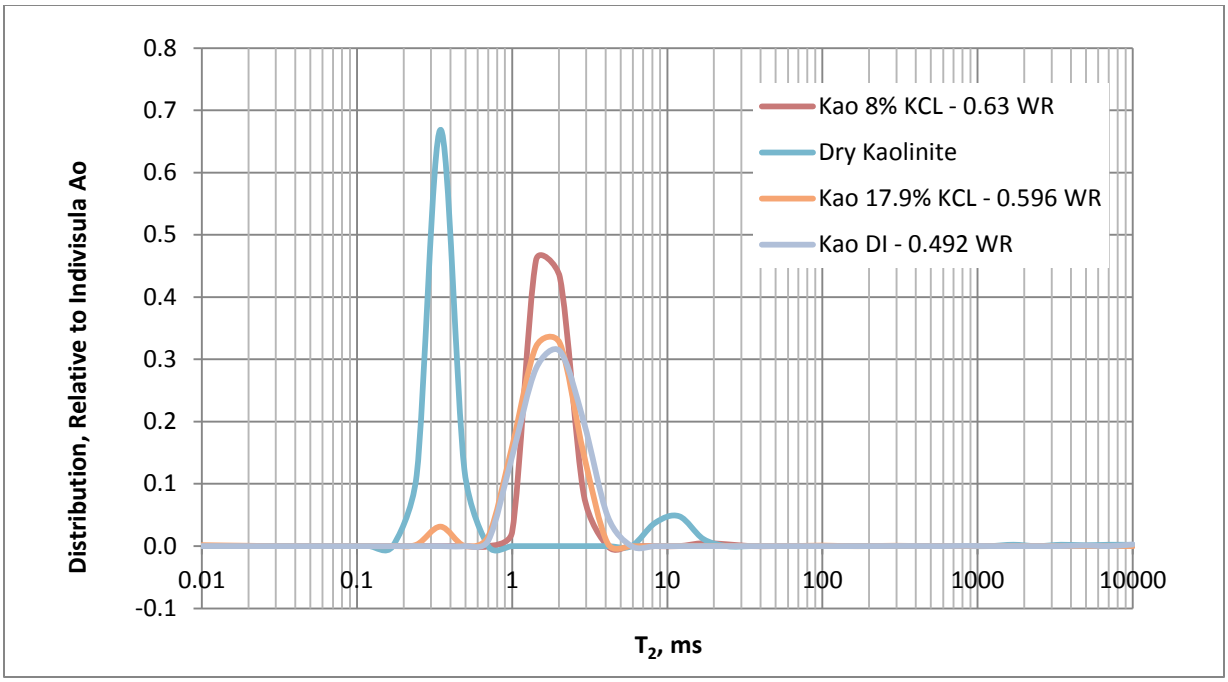

Figure 4.14: Saturated kaolinite samples T_2 distribution compared to the dry sample (blue curve).

For the shale samples, two clear peaks are noticed. One high peak is at faster relaxation times less than 1 ms and the other with lower magnetization at slower relaxation times at about 10 ms as shown in Figure 4.15. The same bi-model distribution has also been observed by Martinez et al. (2000). They studied the distribution of shale samples saturated with DI water and noticed the shift in some samples as a result of the change in the surface to volume pore ratios. In other samples, an increase in the magnetization or broadening in the peak has been noticed. In general, the bi-model has been preserved with noticeable high magnetization for the first peak.

On the other hand, a recent study on shale wettability (Odusina et al., 2011) showed that for the Eagle Ford shales the two peaks almost don't shift when saturating the sample with brine

(25,000 ppm NaCl was used in their study). However, the magnetization of the peak increases remarkably unlike other shale samples from other shale basins.

The distributions obtained in our study show a shift in the peaks toward the right to the higher relaxation times. This shift typically refers to an increase in the porosity, permeability, or saturation of the samples.

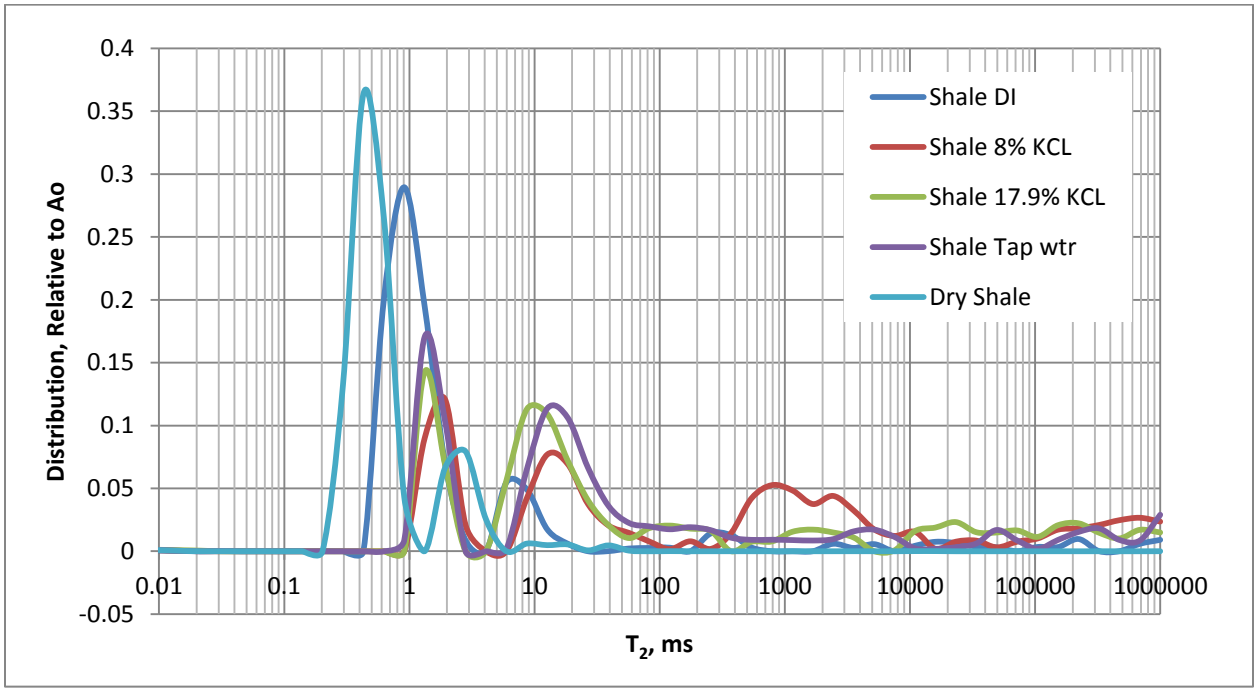

Figure 4.15: Saturated Eagle Ford shale samples T_2 distribution compared to the dry sample.

4.4 Look Into Permeability and Porosity for Eagle Ford Shale Sample

Only a shale sample from given depth of Eagle Ford formation has been tested in this study. The sample has been ground to fit the small test tubes for the NMR measurements. This results in an alteration of the porosity of the rock. The errors associated with the measurements of the shale is slightly higher than those of clays samples as the powder pure clays promotes more homogeneity of the saturated samples than the ground shale does.

Crushed-sample tests for porosity and permeability have been conducted on a shale sample obtained from the same depth in order to evaluate the relationship between these data and the obtained NMR relaxation times. The GRI methods (Luffel et al., 1992 and 1993) have been used for these testes. The obtained porosity and permeability for the sample are 1.6 % and 6.74 x 10^{-6} md, respectively. The GRI method for crushed samples measures the grain volume by the helium injection using the Boyles's Law method. The bulk volume is measured by the mercury immersion. The porosity is then calculated as the difference between these volumes. The permeability is determined using a pressure decay system based on Luffel et al. (1993) GRI method. The crushed sample is subjected to a high pressure (usually helium is used) and the pressure decay is recorded. This decay indicates the penetration into the rock. Models are then used to determine the permeability.

The Kozeny-Carman relationship, equation 4.2, has been used to determine the S/V value for the un-saturated sample using the longitudinal relaxation time (T_1) of 24 ms. This value is estimated from the correlation to the measured transverse relaxation time (T_2) of 0.720 ms as all the values of the two relaxation times show the same trends. The average tortuosity of this sample was assumed to be 10. The S/V ratio was found to be 0.490 nm^{-1} . The T_1 time values have then been used to test the permeability measurements because they are not affected by the diffusion which only affects the transverse relaxation process. The surface relaxivity has been calculated from equation 1.8 and found to be 0.085 micro meter per second assuming the bulk relaxation is neglected. Using this surface relaxivity, the S/V ratios for the saturated shale samples have been calculated from the relaxation times. The bulk relaxation time for water is in the range of seconds, so the associated rate is usually considered negligible. To check the effect of the bulk relaxation, the surface relaxivity was found to be 0.0843 micro meter per second

assuming a bulk relaxation time of 3.0 seconds. Moreover, the S/V ratios calculated assuming this bulk relaxation time are just slightly lower than the S/V ratios assuming only the surface relaxation as shown in Figure 4.16. For our analysis, we assumed that the bulk relaxation is neglected as no significant differences are noticed specially for these small values which will not affect the S/V and porosity curve so much as will discussed afterward.

$$K = \frac{\varphi}{\tau}\left(\frac{V}{S}\right)^2 , \qquad (\tau \text{ is the tortuosity}) \qquad (4.2)$$

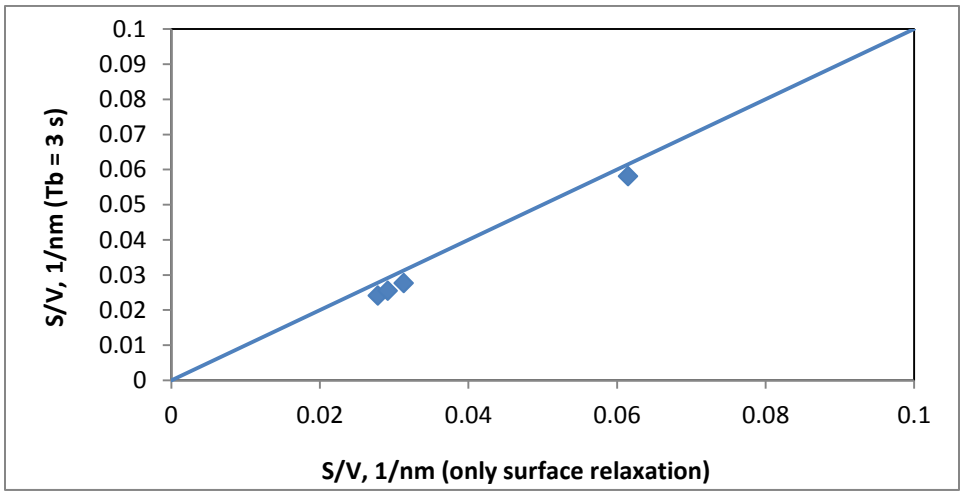

Figure 4.16: Calculated S/V ratios for shale samples.

The S/V measurements then plotted against the sample porosities estimated from the shale and added liquid volumes as shown in Figure 4.17. From this plot, a relationship can be obtained between these two variables. This relationship has been used to determine the permeability values at different porosities. The calculated values are shown in Figure 4.18. Permeability and porosity for another set of samples from the same well at the same formation interval tested in the unconventional natural gas and oil institute (UNGI) geomechanics laboratories are also shown on the same plot. The change between the curves is expected as the sample we used in our study has a lower permeability than the other samples and they couldn't

be tested accurately it in our laboratories due to the limitations of the equipment. In addition, the permeability measurement we obtained is based on the crushed sample analysis which is not the case with the other samples.

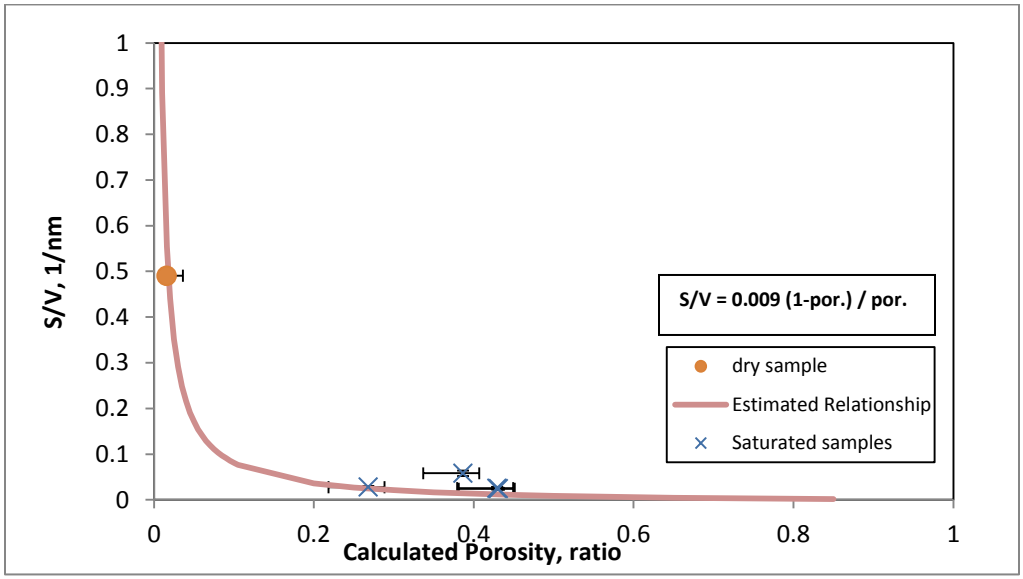

Figure 4.17: Relationship between S/V and porosity for samples tested.

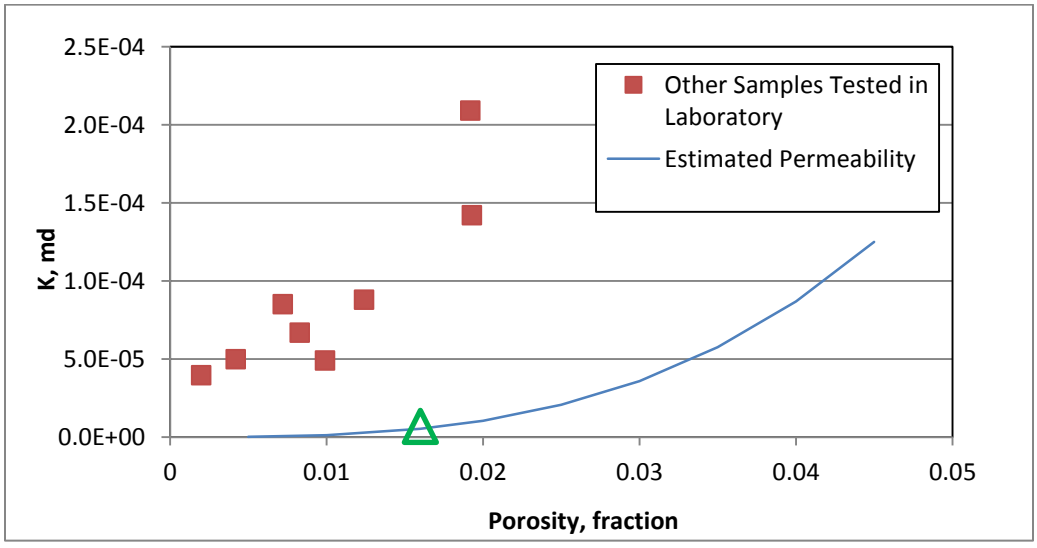

Figure 4.18: Estimated permeability for shale samples. The red points represent other sets of samples of Eagle Ford tested in the CSM laboratories.

The analysis above depends on direct application of the Kozeny-Carman relationship. The results might not provide a perfect solution due to the inadequacy of the used accurate permeability and porosity measurements. However, it gives a picture about the expected ranges of permeability of the rock at different porosities.

There is a plan to design a probe to the high field NMR equipment that is big enough to handle the core plugs eliminating the need to grind them. This will help to get more accurate measurements that can be directly tied to other petrophysical measurements made on the same samples.

CHAPTER 5

NMR STUDY FOR CA-MONTMORILLONITE SWELLING BEHAVIOR

In this chapter, the swelling mechanisms of pure clays will be discussed and tied to the NMR relaxation times and distributions obtained in our research to build a better understanding of the clay swelling behavior. The NMR study has been shown to be helpful in describing the swelling behavior of the montmorillonite samples studied.

5.1 Swelling Mechanisms of Montmorillonites

Smectites in general are organized in quasicrystals. The quasicrystal structure consists of sets of 2:1 silicate layers. The single quasicrystal might contain between two to many thousands stacked layers. A high resolution micrograph of a smectite film (from work by Laird et al. in 1989) is shown in Figure 5.1. The stacked layers are shown clearly in this graph. (Laird, 2006)

Various swelling mechanisms exist in the clays. Among these mechanisms is the crystalline swelling (crystalline hydration) which involves the addition of water sheets between the interlayers of the smectite quasicrystals. The interlayer surfaces in the smectite structure have a negative charge due to the substitution between Si^{+4} and other inter-structure cation like Al+3. For example, when Al^{+3} substitutes Si^{+4} in the silicate tetrahedral later (SiO_4), an oxygen atom becomes free causing a negative charge on the surface. The inter-structure cations and the external cations (e.g. from salt concentrated solution) compete on the water in this interlayer space.

Figure 5.1: Electron micrograph showing the arrangement of smectite layers (Laird, 2006).

Another contributing mechanism to clay swelling is the double-layer swelling which represents the expansion occurring outside the smectite quasicrystals. The diffusion of the negative and positive ions from and to the external surface of the structure and the bulk solution controls this mechanism. In general, some of the negative charge exists outside the smectite layers as the exchangeable cations diffuse to the solution. On the other side, the solution cations dissociate and diffuse toward the negatively charged surfaces. Electrostatic repulsive and attractive forces between the negative and positive ions exist and play role in this kind of swelling.

Laird (2006) described the formation and breakup of quasicrystals as another mechanism of swelling in smectite clays. In this mechanism, two quasicrystals can merge together if they have enough kinetic energy to overcome the repulsion between their double layers. As a result of this merging, the water and charged ions between these quasicrystals will expel out. The result is a big structure with more layers ready for additional crystalline hydration in the interlayer zone.

On the other hand, the quasicrystals may break up under enough external forces like shaking and stirring. An illustration of the structure delineation is shown in Figure 5.2. The formation and breakup of the quasicrystals might be dependent on the layer charge as it decreases the crystalline swelling distance which makes the quiscrystals more stable and larger (Laird, 2006).

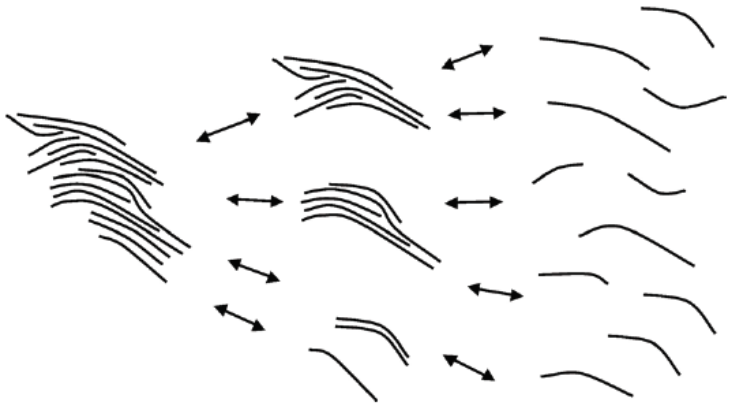

Figure 5.2: An illustration showing the quasicrystals breakage and formation (Laird, 2006).

5.2 Analysis of Clay Swelling Using NMR Data

Twelve samples have been tested to study the NMR response for swelling of Ca-Montmorillonite. Four samples have been saturated with various amounts of De-ionized water, 8% wt KCl and 17.9% wt KCl solutions. Almost identical liquid to dry clay ratios have been kept for those samples. However, to understand the swelling behavior and associated NMR responses, the liquid to dry clay volume ratios were utilized as well although the different samples have different ratios due to the differences in liquid densities. The sample properties used in this section have been discussed earlier in the sample preparation part of this report.

It is worth noting that the longitudinal and transverse relaxation times measured in this study follow the same pattern when the data is plotted against volume or weight ratios as presented in Figure 5.3 thru Figure 5.6. Therefore, the diffusion effect that might be associated with the transverse relaxation does not vigorously affect the behavior of transverse relaxation times in such comparison. Moreover, the bulk relaxation times of liquids usually have values of seconds, so the bulk relaxation decay ($1/T_{bulk}$) is very small and is neglected. Thus, we can assume that the highly affecting relaxation mechanism for the samples tested is the surface relaxation mechanism. The NMR results of this study can be used to describe the swelling behavior of Ca-Montmorillonite clays as the surface relaxation decay is a function of the surface to volume ratio (S/V) of the porous media.

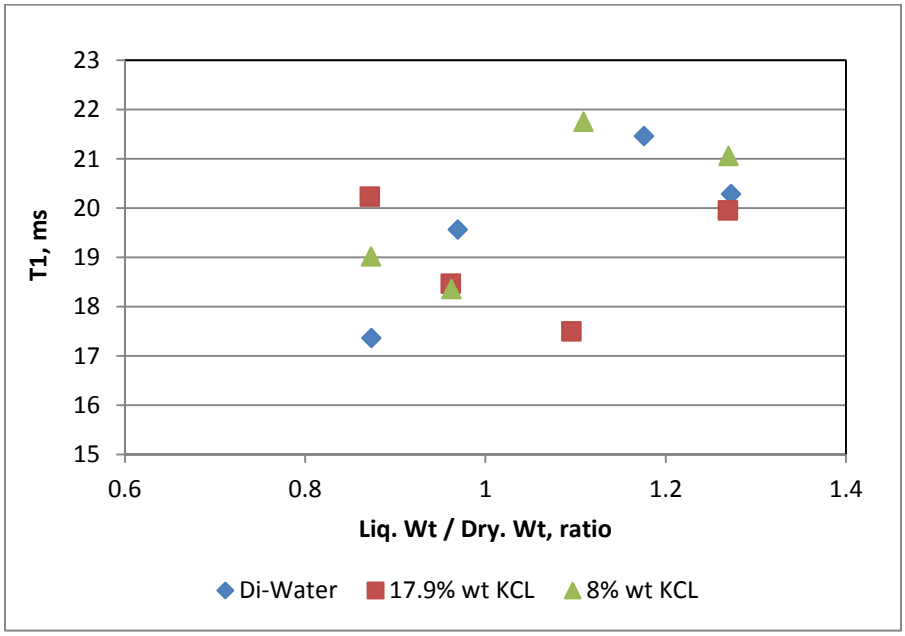

Figure 5.3: T_1 values of montmorillonite at various liquid/clay weight ratios.

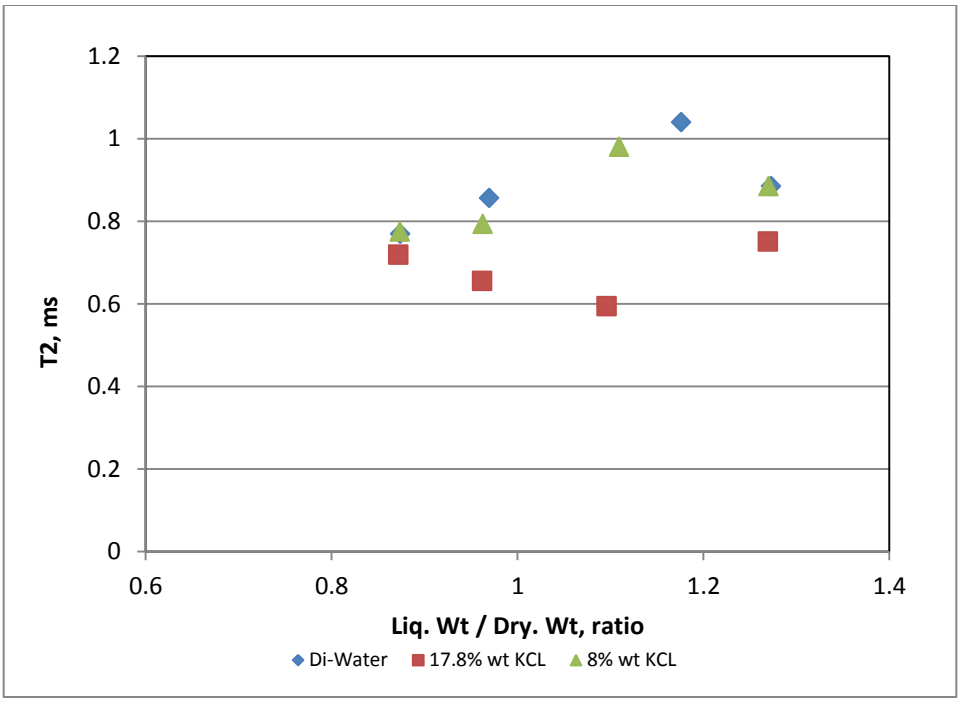

Figure 5.4: T_2 values of montmorillonite at various liquid/clay weight ratios.

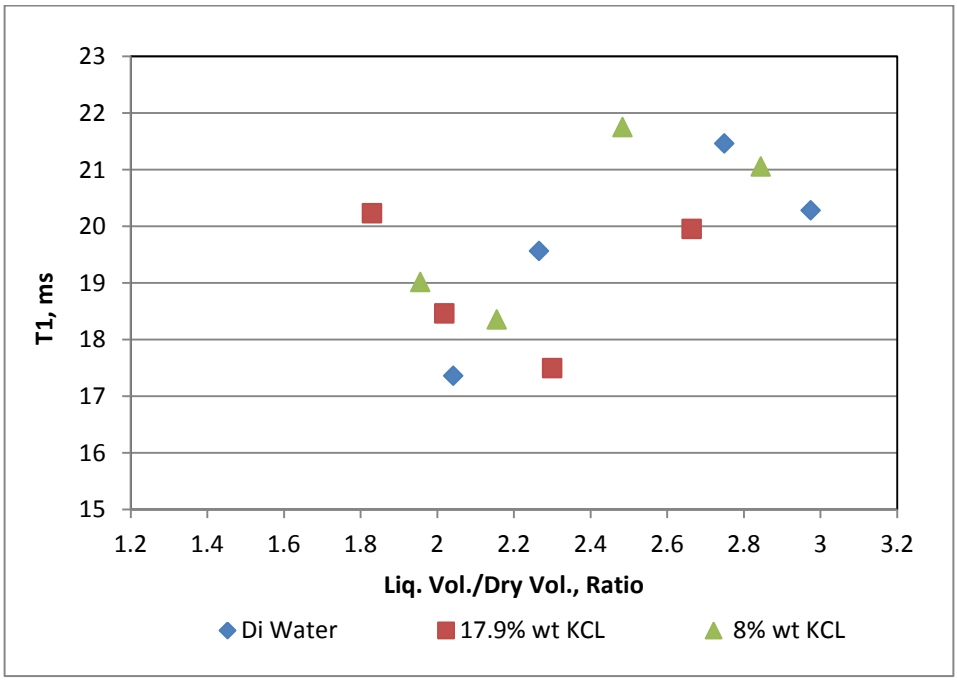

Figure 5.5: T_1 values of montmorillonite at various liquid/clay volume ratios.

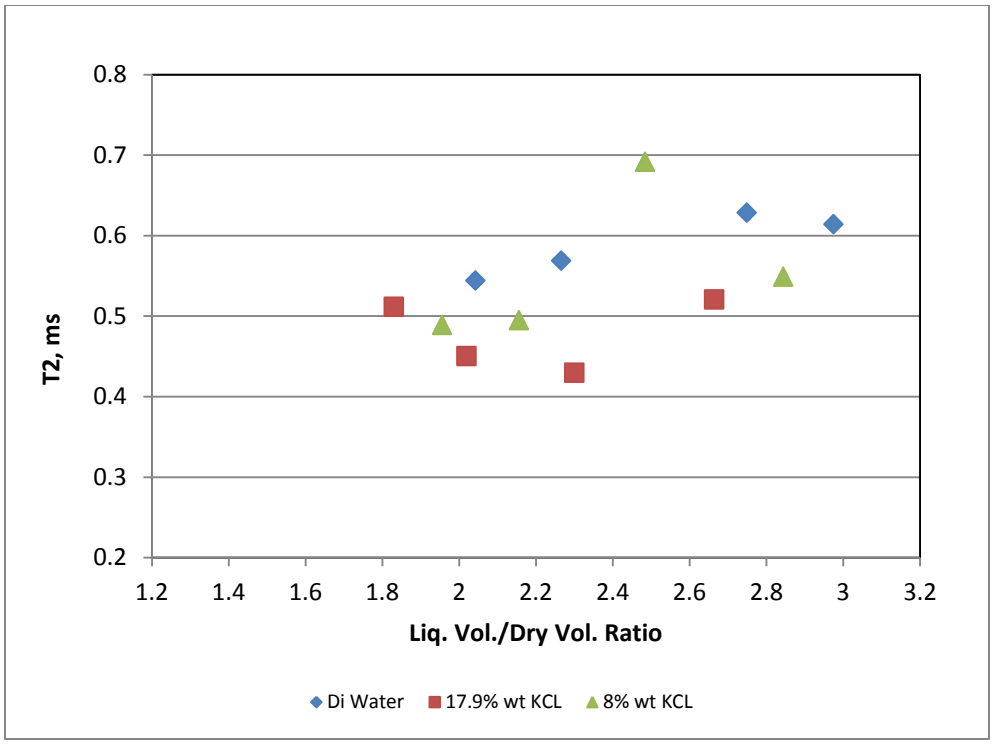

Figure 5.6: T_2 values of montmorillonite at various liquid/clay volume ratios.

All the T_1 data measured falls between 17 and 22 ms as shown in Figure 5.5 while the T_2 values varies between 0.4 and 0.7 ms (Figure 5.6). These ranges might look small for comparisons. However, because clays are very sensitive to swelling and show very fast relaxation times (less than 1 ms) these ranges might be critical and comparing data within them is valid. In general, the samples saturated with 17.9% wt KCl show values concaving up whilst the other samples show the opposite behavior.

The measured T_1 and T_2 values are plotted against the estimated porosities (using 820 m^2/g specific surface area for montmorillonite and the known added volume of water) in Figure 5.7 and Figure 5.8, respectively. The T_2 data doesn't show such clear behavior as T_1. This might be explained by the possible little diffusion that affects the transverse relaxation process

only. The data suggest that the initial portion of water in the dry sample (around 20%) is adsorbed in the external surfaces of the clay which have a specific surface of 70 m^2/g. Moreover, the samples saturated with 17.9% wt. KCl have an average surface relaxivity (ρ_2) value of 3.0 micro-meter per second. The samples saturated with the 17.9% wt. KCl have a surface relaxivity (ρ_1) of 0.083 micro-meter per second whilist the other samples show a value of 0.073 micro-meter per second. This is a result of the alteration in the surface structure changing the relaxation properties on it. This is also related to the impossibility of obtaining any silicon spectra for the samples saturated with the 17.9% wt. KCl suggesting that the small content of iron in the sample has been activated to produce some paramagnetic spots on the surfaces. The surface relaxivity provides information on how the relaxation strength of the pore surfaces is. It increases with the concentration of paramagnetic ions (e.g. iron) content (Bryar, 1999).

The relaxation times are related to the S/V and porosity according to equation 5.1. The average S/V ratios calculated back from the measured longitudinal relaxation times deviate from the total S/V ratios calculated from the clay surfaces and added volumes at some points as shown in Figure 5.9. The results suggest that the interlayer and inter-particle spaces are filled at the same time with the saturating liquid but at different rates changing the average S/V ratios. Starting from lower porosities, the data show a behavior that suggests the movement of fluids from the outer space to the interlayer spaces increasing the average S/V as the volume outside decreases. Moreover, the 17.9% KCl saturated samples show lower S/V values reflecting the slower diffusion of fluids to the interlayer space due to the electrostatic forces on the outer surfaces of the clays that restrict the diffusion of the high salt concentrations. The 8% KCl samples show higher S/V ratios and an earlier entrance to the interlayer space.

$$\frac{1}{T} = \rho \frac{S}{V} = \rho \frac{Specific\ Area*(1-\varphi)*\rho_{dry}}{\varphi} \quad (5.1)$$

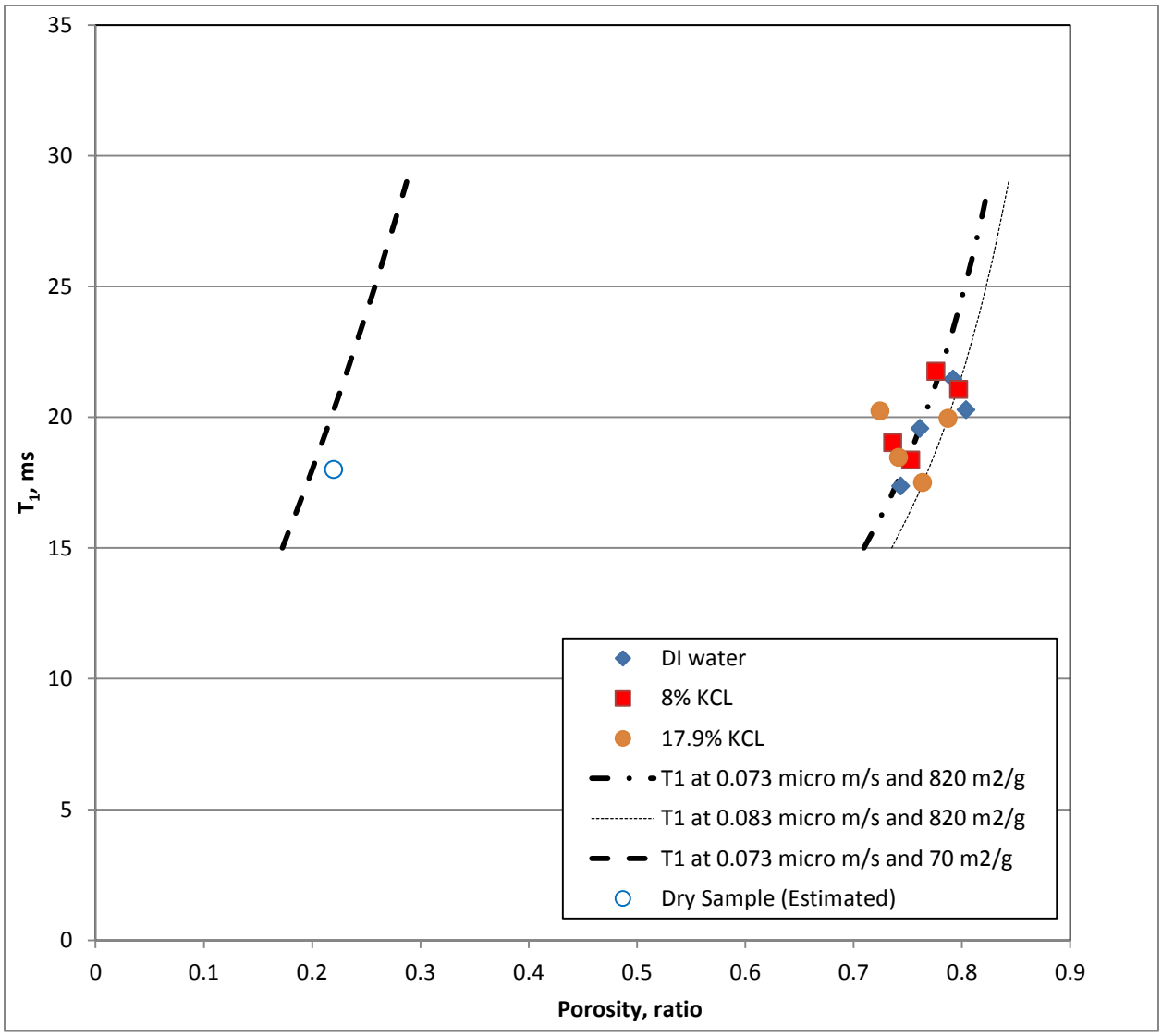

Figure 5.7: T_1 relaxation times versus porosity. The dry sample T_1 value is estimated based on the behavior of the T_2 dry sample.

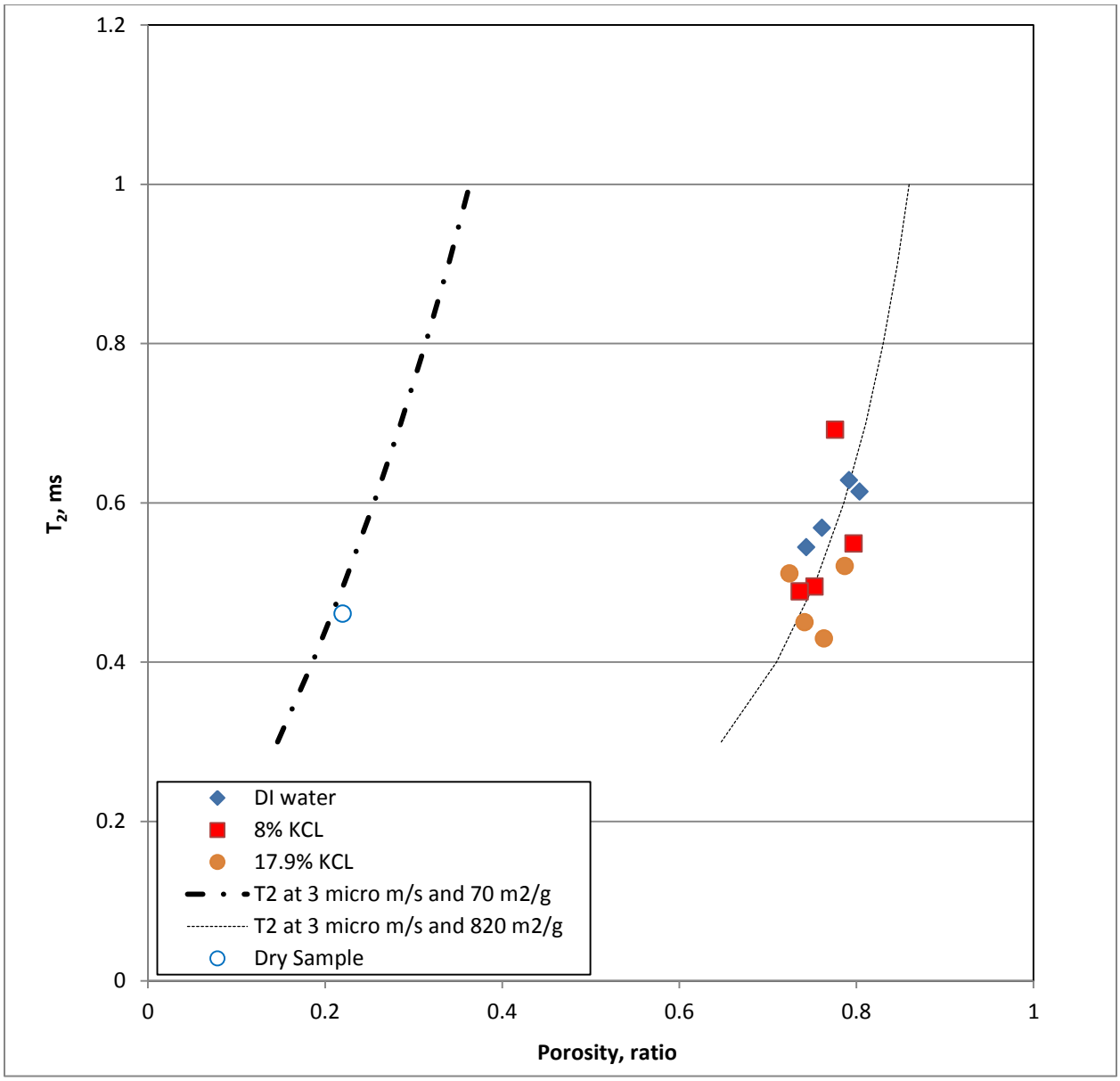

Figure 5.8: T_2 relaxation times versus porosity. The dry sample T_2 value suggests that the original water in the sample is mostly adsorbed on the external surface.

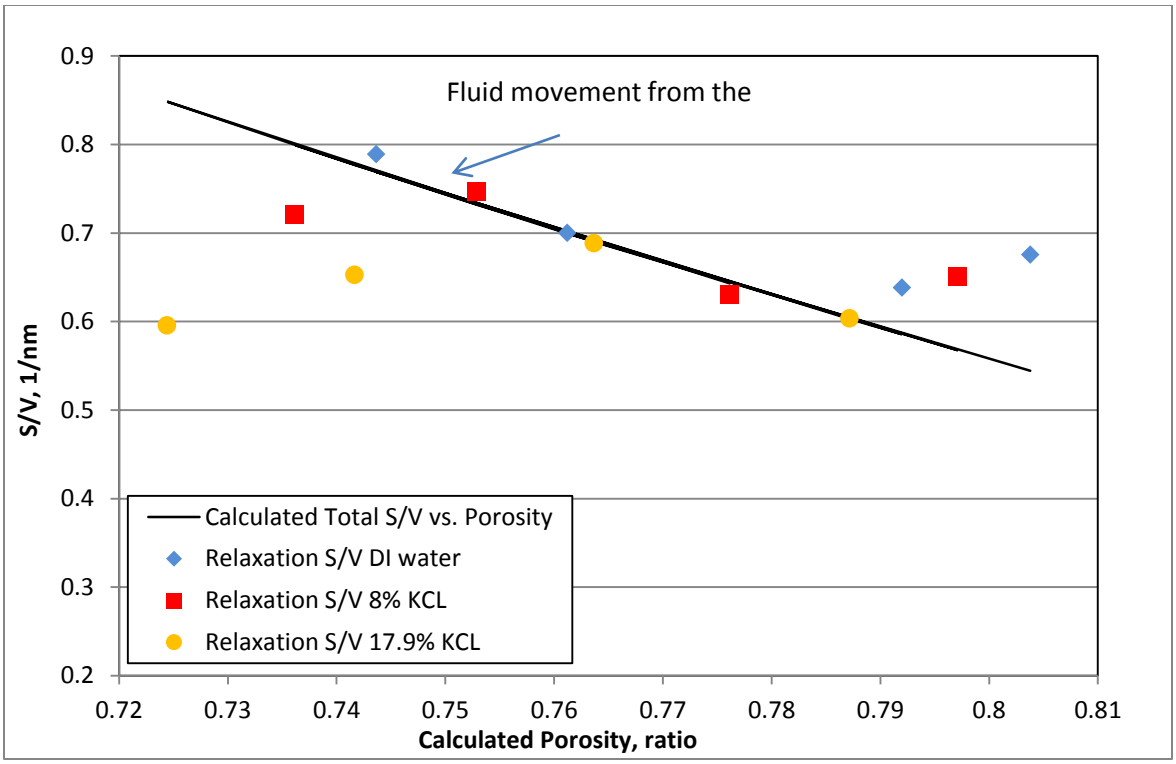

Figure 5.9: NMR average S/V and calculated total S/V for the samples tested in this study.

The middle zone of the plot represents the time when both pore spaces (specially the interlayer) absorb fluids with the surface areas almost constant which matches the ideal theoretical swelling case. For the DI-water saturated, the sample keeps absorbing water inside the clay layers (crystalline swelling) as the water is added to the clay. However, when the volume ratio reaches to approximately 2.6 (0.79 porosity), the interlayer distances reach a maximum and the water start to diffuse back and relax on the outside surfaces of these layers. In this case more surface areas are now available for relaxation, less volume is confined between the layers, and the average surface to area ratio increases. This enhances the surface relaxation, e.g. faster relaxation times. At certain point, this behavior is assumed to disappear or be reversed when more liquid added into these large spaces. Therefore, more relaxation times measurements

are needed to check if the values continuously drop or will get flat at certain point. The same approach applies for the 8% wt KCl saturated samples with a maximum volume ratio of around 2.5. However, the 8% wt KCl saturated samples show sharper T_2 distribution peaks as the salt concentration will help in getting the layers of the structure closely stacked providing regular distribution of the pores, as seen in Figure 5.10.

For the 17.9% wt KCl saturated samples, the solution concentration appears to be very high giving a high charge to the crystalline layers once it enters between them reducing the interlayer distances in the quasicrystals. At the same time, more quasicrystals are formed as more layers merge with each other. We can consider the interlayer space as a small pore in the media. As more clay layers merge together to build larger particles, more of the tighter pores (interlayer spaces) are formed increasing the surface to volume ratio and decreasing the relaxation times at the same time the volume moves inside the layers increasing the S/V for the outside spaces. An illustration of the layers stacking is shown in Figure 5.11.

It has been shown in earlier in section 4.1.2 that the NMR detected a production of (SiO)3 SiOH when the montmorillonite is saturated with the 8% wt KCl. Moreover, the Q4 (0Al) disappeared with just the de-ionized water saturation representing the hydration of the –SiO group to produce the –SiOH group. This might also increase the PH value (related to OH group) in the sample providing more stability in the clay layers through the added negative charge (Tchistiakov, 2000). Moreover, many Si-O-Al could break during this process.

As discussed earlier, the samples saturated with the 17.9% wt KCl did not show any spectra. This can be a result of the effect of the very small amount of paramagnetic ions like iron in the composition that might have been active as the structure of the crystals changed. The iron

content in the clays used in our study is small (the structure as provided by the clay society where clays are obtained is as following: Ca.27 Na.04 K.01)[Al2.41 Fe(III).09 Mntr Mg.71 Ti..03][Si8.00]O20(OH)4). However, the absorption properties of the surfaces in the clays changed, and that is why a different surface relativity has been considered for these samples.

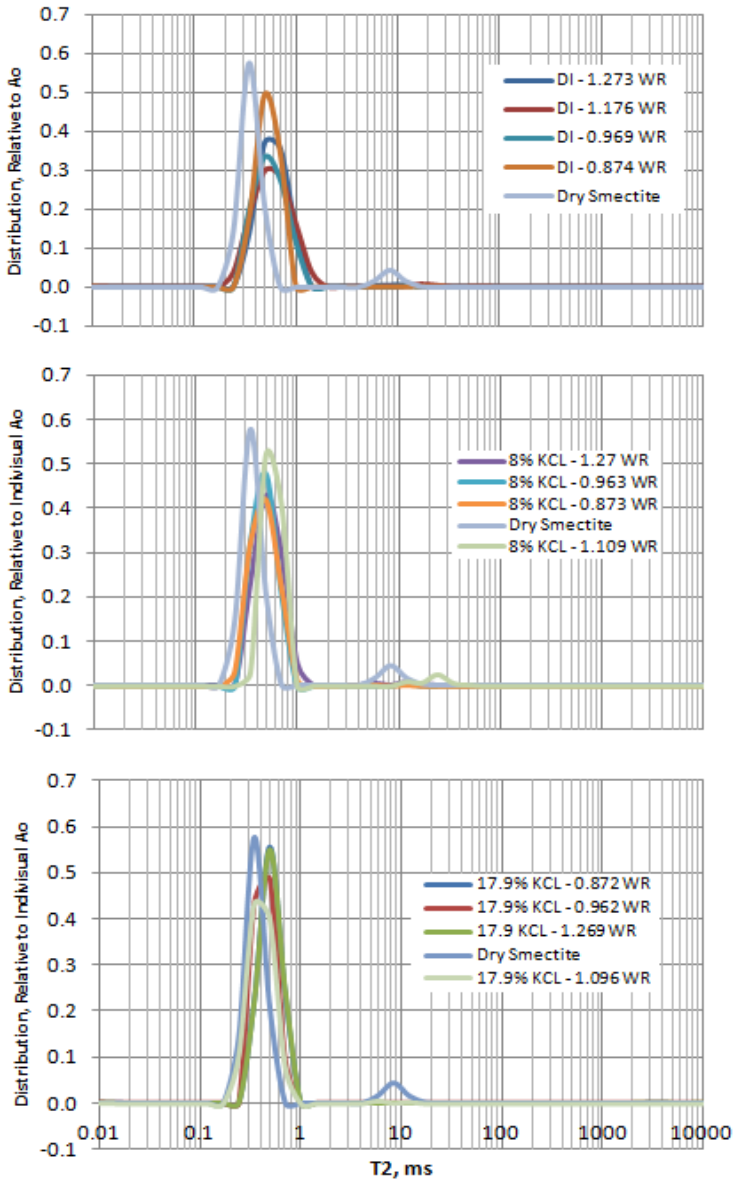

Figure 5.10: Comparison of all the distribution peaks for various fluids used in our experiments.

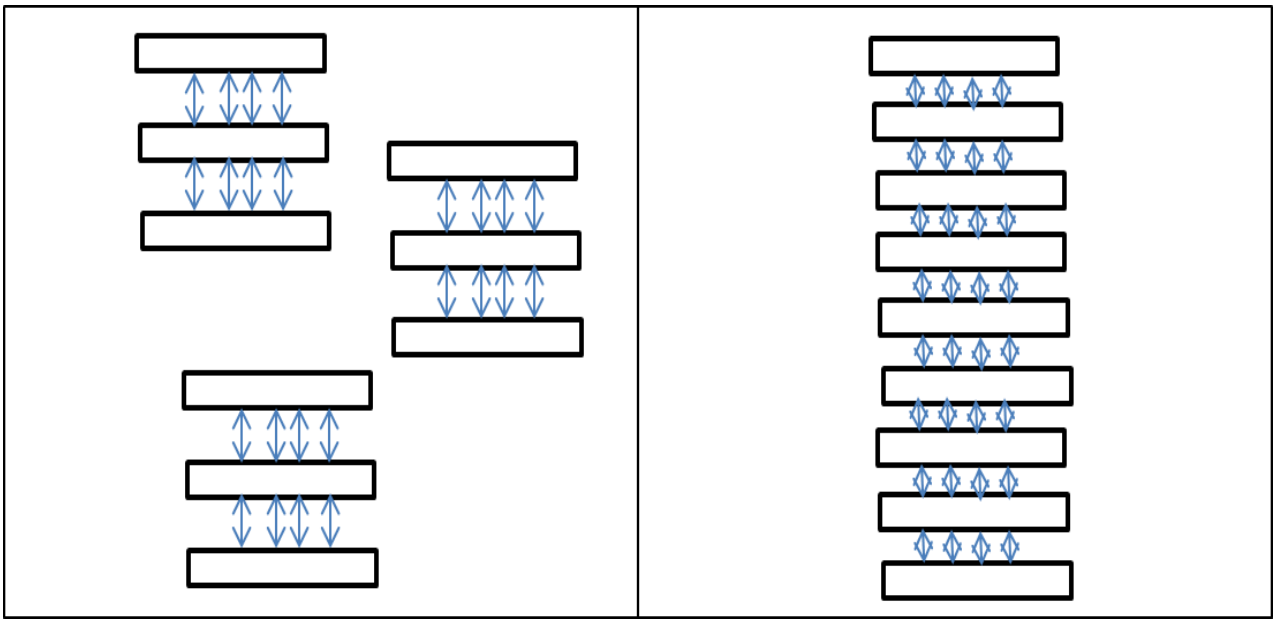

Figure 5.11: An illustration of the smectite layer arrangements when saturated with DI water (left) or KCl solution (right).

CHAPTER 6

CONCLUSIONS AND FUTURE WORK

6.1 Conclusions:

In this study, the swelling mechanisms of pure clays with specific emphasize on montmorillonite have been studied using NMR measurements. The experimental data has been analyzed using relaxation mechanisms determining the role of the salt concentration changes on the swelling characteristics. With the assumptions that the bulk relaxation and relaxation due to diffusion don't really affect the obtained trends of relaxation times (T_1 and T_2), the surface relaxation, a function of the surface to volume ratio, has been used to describe the swelling behavior of the montmorillonite in several liquid/clay systems. It has been concluded that the adsorption process starts from the outside layers of the clays. The interlayer absorption starts afterward at different rates depending on the ionic concentration of the saturating liquid. The interlayer crystalline swelling mechanism appears to play effective role in the swelling when samples exposed to DI water and 8% wt KCl solution. After reaching a maximum capacity of the interlayer expansion, the liquid is expelled outside to start saturating the larger pores opening the interlayer space against the weak attractive forces. A better layer ordering in the presence of the KCl concentration in the latter liquid is observed. This is due to the stacking of the layers that is also observed in the sharper T_2 distribution peaks. However, as we are conducting a free swelling experiment (no external stresses on the clay) the 17.9% wt KCl also shows the interlayer expansion. Moreover, no silicon spectra have been detected for the samples exposed to 17.9% wt

KCl. This can be due to either the activity of the paramagnetic iron (not shown in the samples saturated using 8% wt KCl solution) or the destruction of the silicon bonds in the composition. Both infer a sort of structure alteration takes place at this high KCl concentration. The formation of $(SiO)_3$ SiOH group has been detected in the 8% wt KCl case. The change in the structure of clays surfaces must be taken in consideration when analyzing the NMR data. More of this formation is expected to take place in higher salt concentration systems increasing the PH values in these systems.

The Kozeny-Carman permeability relationship has been used to develop a permabiity model for the shale tested in this study. Permeability and porosity data obtained for the Eagle Ford shale sample by the GRI methods and the data obtained from the NMR experiments have been utilized to develop this model. The relationship seems providing reliable results taking in consideration of the few test points we have to build this relationship.

In brief, the potential of the high field NMR technique for characterizing the swelling behavior of pure clays and shales has been verified in this study. Moreover, the available information on permeability and porosity suggested a good potential of using the NMR data to estimate the properties of this shale. The capability of investigating the structures of the clay and shale samples and testing of the dry or clay (shale)/water systems in un-compacted conditions could be used in further studies of the unconventional systems.

6.2 Future Work

Upon to completion of this thesis, the following are recommended as a continuation of the research study initiated here.

1- Tests on other pure clays and shale formations are recommended to be conducted in order to build a set of family curves for future references.

2- Other salt concentrations are recommended to be tested in order to have a general conclusion on swelling.

3- Petrophysical and acoustic properties of these pure clay and shale samples are suggested to be measured in order to correlate to the NMR relaxation response. To test this concept, we have tested one sample. The results of this sample are plotted and compared to data obtained by Mese (2001) as shown in Figure 6.1. The sample showed ultrasonic velocities slightly higher than these of the smectite used in Mese's study.

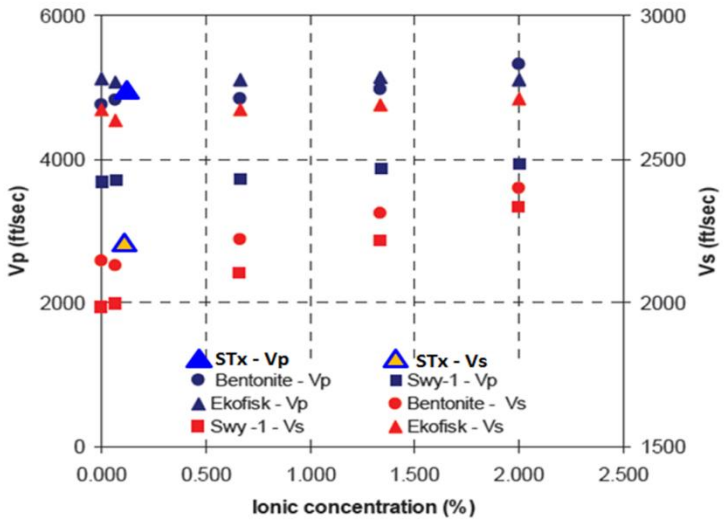

Figure 6.1: Acoustic velocities of a montmorillonite sample tested in this study plotted with other data reported by Mese (2001).

4- A probe that can handle a core plug is required to test shale samples to correlate the NMR properties to other measured properties (e.g. porosity, permeability, and acoustic properties). It will also be beneficial to consider the stress related changes in

the new probe design in order to conduct the tests in elevated pressure conditions helping to have a more accurate predictive model.

5- Continuation of the detailed investigation on the shale NMR porosity and permeability from several basins is recommended to find the best correlations for the unconventional systems.

REFERENCES

Abu-Shanab, M. M., Hamada, G. M., Oraby, M. El., Abdel Wally, A. A., 2005, Improved Porosity Estimation in Tight Gas Reservoirs from NMR and Density Logs, Emirates Journal for Engineering Research, Vol. 10, No. 2, p 9-13.

Bryar, T. R., Daughney, C. J., Knight, R. J., 2000, Paramagnetic Effects of Iron (III) Species on Nuclear Magnetic Relaxation of Fluid Protons in Porous Media, Journal of Magnetic Resonance, Vol. 142, p 74-85.

Chitale, D. V. Gardner, J., Sigal, R., 2000, Significance of NMR T2 Distributions from Hydrated Montmorillonites, SPWLA 41th Annual Logging Symposium, June 4-7.

CNS Clinic, 2011, MRI Physics, http://www.iomonitoring.pro/mrphysics.htm

Coates, G. R., Xiao, L., Prammer, G. 1999, *NMR Logging Principles and Applications*. Houston: Haliburton Energy Services, 234 pages.

Dlubac, K., Knight, R., 2010, An Assessment of the Use of the Kozeny-Carman Relationship to Estimate Permeability in Anisotropic Materials from NMR Data, SEG Denver 2010 Annual Meeting, p 2644-2648.

Dunn K., LaTorraca, G. A., Bergman, D. J., 1999, Permeability Relation With Other Petrophysical Parameters for Periodic Porous Media, Geophysics, Vol. 64, No. 2, March-April, p 470-478.

Dunn, K. –J., Bergman, D. J., Latorraca, G. A., 2002. *Nuclear Magnetic Resonance Petrophysical and Logging Applications*. Seismic Exploration Vol. 30, Oxford: Elsevier Science Ltd, 311 pages.

Freedman, R., Heaton, N., 2004, Fluid Characterization using Nuclear Magnetic Resonance Logging, Petrophysics, May-June, Vol. 45, No. 3, p 241-250.

Ghosh, Pallab, 2012, DLVO Theory and Non-DLVO Forces, Interfacial Engineering Lecture Notes, National Programme on Technology Enhanced Learning, India, http://www.nptel.iitm.ac.in/courses/103103033/16

Glorioso, J. C., 2012, Unconventional Reservoirs: Basic Petrophysical Concepts for Shale Gas, Proceedings for the SPE/EAGE European Unconventional Resources Conference and Exhibition, Vienna, Austria, March 20-22.

Hamada, G. M., 2012, Petrophysical Properties Evaluation of Tight Gas Sands Using NMR and Conventional Logs, Proceedings for the SPE Middle East Unconventional Gas Conference and Exhibition, Abu Dhabi, UAE, Jan. 23-25.

Laird, D. A., 2006, Influence of Layer Charge on Swelling of Smectites, Applied Clay Science, Vol. 34, p74-87.

Luffel, D. L., Guidry, F. K., 1992, New Core Analysis Methods for Measuring Reservoir Rock Properties of Devonian Shale, JPT, November, p 1184-1190.

Luffel, K. L., Hopkins, C. W., Schettler Ju., P. D., 1993, Matrix Permeability Measurement of Gas Productive Shales, Paper SPE 26633, Proceedings for the 68th Annual Technical Conference and Exhibition of the Society of Petroleum Engineers, Houston, Texas, Oct. 3-6.

Marino, I. G., 2007, Regularized Inverse Laplace Transform Matlab Code, http://www.mathworks.com/matlabcentral/fileexchange/6523-rilt

Martinez, G. A., Davis, L. A., 2000, Petrophysical Measurements on Shales Using NMR, Paper SPE 62851, Proceedings for the 2000 SPE/AAPG Western Regional Meeting, Long Beach, California, June 19-23.

Matteson, A., Tomanic, J. P., Herron, M. M., Allen, D. F., and Kenyon, W. E., 2000, NMR Relaxation of Clay/Brine Mixtures, SPE Reservoir Eval. & Eng., Vol. 3, No. 5, October, p 408-413.

Mese, A. I., 2008, Clay-Water Interaction, Intermolecular Forces and Acoustic Velocity, SEG, Las Vegas Annual Meeting, p 1615-1619.

Mese, A.I., 1995, Effect of Fluid Saturation and Stress State on The Mechanical and Chemical Properties of Shales, PhD Dissertation, The University of Texas at Austin.

Mitchell, J., Chandrasekera, T. C., Gladden, L. F., 2010, Obtaining True Transverse Relaxation Time Distributions In High-Field NMR Measurements of Saturated Porous Media: Removing The Influence of Internal Gradients, The Journal of Chemical Physics, Vol. 132, Issue 24, Article 244705.

Nelson, P. H., 2009, Pore-Throat Sizes in Sandstones, Tight Sandstones, and Shales, AAPG Bulletin, Vol. 93, No. 3, March, p 329-340.

Odusina, E., Sondergeld, C., Rai, C., 2011, An NMR Study on Shale Wettability, Paper CSUG/SPE 147371, Proceedings for the Canadian Unconventional Resources Conference, Calgary, Alberta, Canada, November 15-17.

Prammer, M. G., Drack, J. C., Bouton, J. C., Gardner, J. S., Coates, G. R., Chandler, R. N., and Miller, M. N., 1996, Measurements of Clay-Bound Water and Total Porosity by Magnetic Resonance Logging, Paper SPE 36522, Proceedings for the SPE Annual Technical Conference and Exhibition, Denver, Co, The United States, October 6-9.

Process NMR Associates, 2012, ^{29}Si NMR Chemical Shifts - Silicone Materials, Process NMR Associates, LLC, http://www.process-nmr.com/Table%205%2029Si%20Shifts.htm

Provencher, S. W., 1982, A Constrained Regularization Method for Inverting Data Represented By Linear Algebraic or Integral Equations, Computer Physics Communications 27, pages 213-227.

Reich, I. L., 2012, NMR Spectroscopy, Chemistry 345 Lecture Notes, University of Wisconsin, Madison, WI.

Schurko R., 2009, Introductory Solid State NMR Notes, http://mutuslab.cs.uwindsor.ca/schurko/ssnmr/index.html

Slade, P. G., Quirk, J. P., Norrish, K., 1991, Crystalline Swelling of Smectite Samples in Concentrated NaCl Solutions in Relation to Layer Charge, Clays and Clay Minerals, Vol. 39, No. 3, p 234-238.

Sun, B., Skalinski, M., Brantjes, J., Liu, C., LaTorraca, G. A., Menard, G., Dunn, K., 2008, Accurate NMR Fluid Typing Using Functional T_1/T_2 Ratio and Fluid Component Decomposition, Paper IPTC 12837, Proceedings for the International Petroleum Technology Conference, Kuala Lumpur, Malaysia, December 3-5.

Tchistiakov, A. A., 2000, Colloid Chemistry of In-Situ Clay-Induced Formation Damage, Paper SPE 58747, Proceedings the 2000 SPE International Symposium on Formation Damage Control, Lafayette, Louisiana, February 23-24.

TKAC, I., Komadel, P., Muller, D., 1994, Acid-treated Montmorillonites – A Study By ^{29}Si and ^{27}Al MAS NMR, Clay Minerals, Vol. 29, p 11-19.

Traficante, D. D., 1996, Relaxation: An introduction, Encyclopedia of Nuclear Magnetic Resonance, edited by M. D. Grant and R. K. Harris, Wiley, New York, Vol. 6, p. 3988 - 4003.

Tutuncu, A.N, 2012, Shale Reservoir Engineering Lecture Notes, Colorado School of Mines, Golden, PEGN 615.

Tutuncu, A.N., 1992, Velocity Dispersion and Attenuation in Granular Sedimentary Media, PhD Dissertation, The University of Texas at Austin.

US Geological Survey, 2013, A Laboratory Manual for X-Ray Powder Diffraction, U. S. Geological Survey Open-File Report 01-041, http://pubs.usgs.gov/of/2001/of01-041/htmldocs/clays/smc.htm

Wang H., 2010, Rethinking of Shale Swelling Based on Interesting Test Results, Paper ARMA 10-127, Proceedings for the 44th US Rock Mechanics Symposium and 5th U.S. –Canada Rock Mechanics Symposium, Salt Lake City, June 27-30.

Wang, Z., Wang, H., Cates, M. E., 1998, Elastic Properties of Solid Clays, SEG Expanded Abstracts.

XIAO, L., MAO, Z., LI, G., JIN, Y, 2012, Calculation of Porosity from Nuclear Magnetic Resonance and Conventional Logs in Gas-Bearing Reservoirs, Acta Geophysica, Vol. 60, No. 4, pages 1030-1042.

Yang Y., 2012, Personal Communication, NMR Laboratory, Chemistry Department, Colorado School of Mines

Yew, C. H., Wang C. L., 1992, A Theory on Water Activity Between Drill-Fluid and Shale, Rock Mechanics, Tillerson & Wawerisk (eds), Rotterdam: Balkema, pages 717-725.

Young, R., Taylor, L. O., Warkentin, B. P., 1962, Swelling Pressures of Sodium Montmorillonite at Depressed Temperatures, Clay and Clay Minerals, Proceedings to the 11th National Conference on Clays and Clay Minerals, pages 268-281.

Zhang, J., Chen, J., Edwards, C., 2012, Lab NMR Study on Adsorption/condensation of Hydrocarbon in Smectite Clay, Paper SPE 151136, Proceedings for the SPE/EAGE European Unconventional Resources Conference and Exhibition, Vienna, Austria, March 20-22.